Faculty of Engineering
Department of Applied Physics
Head of the department: Prof. Dr. Ir. C. Leys

Electrical Probe Measurements on the COMPASS Tokamak

By

Gregory Cieters

Promotor: Prof. Dr. Ir. G. Van Oost
Co–promotor: Dr. J. Stöckel
Supervisors: Dr. J. Adámek, Dr. R. Dejarnac, Dr. J. Horáček

The research reported in this thesis was performed at the
Institute of Plasma Physics AS CR, Za Slovankou 1782/3,
182 00 Praha 8, Czech Republic

Thesis submitted to obtain the academic degree in Science of
Master in Physics and Astronomy, option Research

Academic Year 2010–2011

English abstract

The goal of this thesis is to examine some basic plasma properties at the edge of the COMPASS tokamak with the aid of electrical probes. The probe systems available on COMPASS are an array of divertor probes consisting of 39 Langmuir probes and a reciprocating manipulator oriented in the midplane equipped with four Ball-Pen probes and four Langmuir probes.

The data acquired with the divertor probes will be used to obtain the $I - V$–characteristics and hence to derive the plasma density, electron temperature and floating potential along the array of the probes. Furthermore the divertor probes are used to determine possible correlations between these basic plasma parameters. Finally it will be demonstrated that the divertor probe array can be used as a crude plasma position sensor.

The reciprocating manipulator will be used especially for measuring directly the plasma potential and determining the electron temperature.

old version

The goal of this thesis is to examine some basic plasma properties at the edge of the COMPASS tokamak with the aid of electrical probes. The probes available on COMPASS are an array of divertor probes consisting of 39 Langmuir probes and a reciprocating probe oriented in the midplane with four Ball-Pen probes and four Langmuir probes. The data acquired with the divertor probes will be used to obtain the $I - V$–characteristics and hence to derive the plasma density, electron temperature and floating potential along the array of the probes. The same will be done with the data from the reciprocating probe and the radial profiles of these plasma parameters will be determined. Finally, a comparison between both probe systems will be performed at different discharge regimes.

Contents

Part I

Preliminaries

Chapter 1

Introduction

1.1 The world energy problem

1.1.1 The need for energy

Energy. It is the most fundamental building block of all modern civilizations. From burning firewood, coal and oil to nuclear, solar and wind energy, energy resources have evolved throughout history and are still doing.

Look around you and think about all the energy we consume and how dependent we are from it. Even this thesis could not have been written without energy. Plenty of hours of computer work were needed to produce the result as now can be read. Every hour my computer was turned on roughly 0.1 kWh energy was needed. And I am not the only one with a computer... Most of the families in the Western Society has at least one computer which all added up consumes a lot of energy. Above we do not only use computers in our daily live but also different kinds of other electronical devices or services which requires large amounts of (electrical) energy. Mankind is addicted to energy.

In table 1.1 a brief selection is given about the per capita energy consumption. On average a human consumes roughly 73.10^6 Btu or about 21400 kWh per year (in 2007) and for the moment we are with almost 7 billion on this planet. Depending on some factors like fertility and mortality there are different predictions for the future population on Earth. Anyhow every model predicts an increase of humans (see figure 1.1a). The most plausible model estimates that earth's population will increase untill 8.9 billion in 2050 [1]. Along the growing population the demand for energy will increase. Above the less developed countries will notice a better standard of living for their citizens (which is a right for everybody!). Conclusion is that the world's hunger for energy will never be satisfied and even will keep rising. Most of our energy nowadays originates from fossil fuels. Hence the possible solution to our energy problem is digging for more oil, coal and gasses, or not ...?

1.1.2 The problem with current energy resources

If we even forget about the future energy demand we are still running into big problems. In 2007 it was estimated that 86.8% of our energy was produced by means of fossil fuels like oil, coal and gass (see figure 1.1b). Unfortunately nothing lasts for ever and so do the fossil fuels reserves. In for instance [4] it is estimated that the oil reserves will run out within 35 years, while coal reserves are put on 107 years and natural gas reserves on 37 years. Although different depletions times are given depending on the model used, all the models agree that one can speak about time periods of the order of decades till a few centuries. Hence it is clear that the natural resources for fossil fuels are running out and that this will happen not so far in the future! And is it justified to simply burn these resources while they are of great importance for different kind of derived products (e.g. plastic, textiles, ...)? Above fossil fuels resources are located on

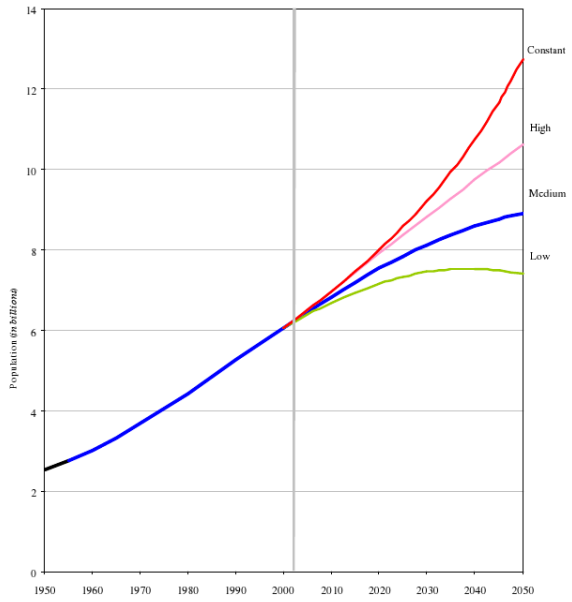

(a) Predicted world population. "Constant" means that fertility remains the same as in 2002. "High" means a slightly lower fertility than in 2002 while "Medium" and "Low" are still lower [1].

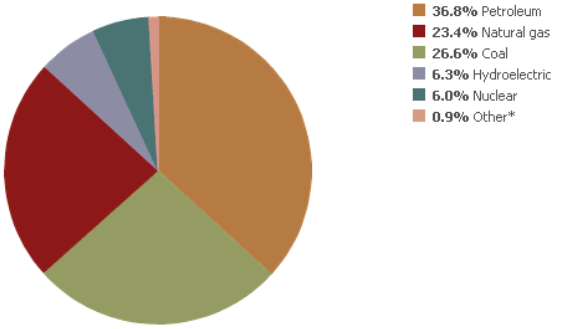

(b) Distribution of the different kind of energy resources in 2005 [2].

Figure 1.1: World population and energy resources.

a limited amount of places across the Earth which provide economical and political power to only a selected number of "owners". In the past this was the cause of several conflicts and with current prospects this will not change, in contrary ...

Another aspect is the term "global warming". The Earth is a highly complex system which we still do not understand completely. Science has revealed that during the last century the mean temperature of the Earth is increasing. The cause of this phenomenon is still a topic of heated discussions. Almost certainly the CO_2–emission resulting from the combustion of fossil fuels is playing a role in this entire "global warming"–effect. As mentioned already we do not yet know the full effect of fossil fuels. There exists a typical Dutch proverb *"Beter voorkomen dan genezen* [1] " that even advises us to reduce the combustion of fossil fuels. Don't forget that above CO_2–emission the entire fossil–fuel–machinery is a polluting industry. Think at the devasting effects of oil leaks on the environment or the destruction of valuable natural habitats for mining[2].

1.1.3 Solutions for energy supply

Nuclear fission and renewables

There already exist alternatives for fossil fuel combustion. An important one is nuclear fission which represents about 6.0% of the world's energy production. A priori this way of producing energy is relative efficient and safe. Although there were some disasters[3] in the past, the safety procedures are improving in order to reduce the risk of such catastrophic events. Nevertheless incidents always happen. Every year there are more victims due to traffic than due to nuclear incidents...

[1] Literally translated this means "better to prevent than to cure".

[2] e.g. 20 April 2010, Gulf of Mexico, BP Deepwater Horizon; 24 March 1989, Alaska, Exxon Valdez; 'hidden' oil spill in Niger Delta; ...

[3] e.g. 26 April 1986, Chernobyl, Ukrain; 28 March 1979, Three Mile Island, Pennsylvania, USA; and more recently the Fukushima incidents of March 2011, Japan.

Table 1.1: Annual energy consumption per capita. Values are expressed in units 10^6 Btu (1 Btu = 1055.05585 J) [3].

Country	2000	2001	2002	2003	2004	2005	2006
Canada	416.4	406.5	414.9	425.1	430.7	439.5	427.2
United States	350.6	338.0	340.2	338.3	342.5	339.9	334.6
Argentina	71.2	68.9	64.7	68.8	71.0	74.6	79.0
Brazil	48.7	47.7	47.7	47.7	49.0	50.4	51.2
El Salvador	17.7	18.4	17.9	19.0	18.3	18.9	19.2
Haiti	3.2	3.4	3.4	3.3	3.3	3.3	3.3
Venezuela	117.9	127.1	121.3	111.0	117.7	123.3	124.4
Belgium	266.3	262.5	259.7	269.2	271.2	268.0	265.1
Czech Republic	156.7	163.7	162.1	170.4	169.3	173.7	176.6
Denmark	163.8	165.5	158.9	165.9	159.5	153.0	161.3
Finland	234.1	236.3	239.6	252.7	256.7	240.3	252.7
France	177.4	180.2	177.7	178.7	182.1	180.4	180.7
Germany	173.5	177.7	174.0	177.0	178.9	175.9	177.5
Luxembourg	350.6	360.7	377.7	392.5	426.7	429.3	424.1
Netherlands	238.5	245.3	244.3	246.6	252.0	257.8	250.9
Norway	436.2	413.3	425.3	398.5	413.5	429.1	410.8
Sweden	254.2	268.7	253.4	241.6	256.3	258.8	245.8
United Kingdom	163.2	165.0	162.3	164.1	163.9	164.1	161.7
Russia	187.2	189.9	192.4	199.4	206.2	210.5	213.9
Kuwait	460.9	432.2	420.4	439.9	446.1	496.0	469.8
Oman	134.5	132.2	132.7	127.0	131.2	162.9	177.2
Qatar	866.0	653.3	664.4	715.2	839.3	978.1	1.023.3
Burundi	1.0	1.0	1.0	1.0	0.9	0.8	0.8
Congo (Kinshasa)	1.8	1.5	1.4	1.5	1.6	1.6	1.6
Ethiopia	1.0	1.0	1.1	1.2	1.2	1.2	1.4
South Africa	104.2	105.3	102.2	109.7	117.3	115.4	117.2
Sudan	3.0	3.7	3.8	4.1	4.3	4.5	4.8
Australia	253.2	259.5	262.7	260.4	264.2	277.2	276.9
Bangladesh	3.9	4.2	4.3	4.5	4.7	4.8	5.0
China	29.3	30.9	33.7	39.2	46.2	51.1	56.2
India	13.4	13.6	13.3	13.5	14.4	14.9	15.9
Japan	177.0	175.2	174.2	173.9	178.4	178.3	178.7
Korea. North	39.7	40.2	38.3	39.1	39.6	40.7	41.1
Korea. South	166.6	169.8	174.9	179.2	184.0	189.7	193.4
Mongolia	28.1	29.6	31.0	28.9	30.9	33.2	33.0
World Total	**65.6**	**65.5**	**66.0**	**67.7**	**70.2**	**71.7**	**72.4**

The most important disadvantage of fission is the nuclear waste. In a fission reaction a heavy nucleus is split by an incident neutron into two or more daughter nuclei of which at least one of them is radioactive. As a consequence nuclear fission not only produce energy but also leaves us with tons of radioactive waste. This nuclear waste is a danger for humans and its environment. Moreover this waste is long lived and needs to be stored safetly for many generations. Although there are some important drawbacks with nuclear fission, it can not be excluded as energy source for the moment. Even in future nuclear fission will play probably a crucial role. The new

generation of fission power plants will produce less radioactive waste than the old ones and this will keep improving for future generations. Furthermore new methods[4] for waste treatment will also help to reduce the radioactive waste left by nuclear fission.

Another alternative for fossil fuels are renewables of which hydroelectricity is the most important for the moment. This method turns gravitational potential energy of large amounts of water into kinetic energy which can drive turbines and hence producing electricity. Hyrdoelectricity roughly takes another 6.3% of the world's energy supply. This method of obtaining energy does not pollute the environment. But the main disadvantge is the fact that one needs plenty of dams which need to be big enough to produce considerable amounts of energy. Although no pollution is created, the environment drastically changes: entire areas are being flooded[5], influencing fauna and flora and the lives of local inhabitants. Furthermore the creation of gigantic dams is not everywhere possible. So hydroelectricity is not a full option for future energy production, it can only be an addition. Other renewable energy source are geothermal, solar, tide, wind, wood and waste. These ways of energy production only account for a tiny fraction of the total, less than 1%. The big problem with most kind of renewables (solar, tide, wind, geothermal and even wood) is scaling and the fact that there is a strong dependency on location. Waste combustion does not depend on location and can be a promising energy production method. However, like most renewables, this techique is quite new and still needs a lot of development. Anyway renewables will play an important role in the future.

Nuclear fusion

A very promising alternative which is still in an experimental phase is nuclear fusion. It will be a clean and almost inexhaustible way of energy production. Inherently nuclear fusion does not produce any polluting byproducts. There is no emission of green house gasses and essentialy no radioactive waste is produced. Only indirect radioactivity is induced due to neutron emission which can activate materials in the reactor. Nevertheless by the right choose of reactor materials and later on fusion reactions without neutron induction (see section 1.2.3) the radioactive waste is negligible compared to nuclear fission. Most of the waste could be recycled after a few decades and the amounts produced are only a fraction of nuclear fission. Concerning the resources nuclear fusion is quasi inexhaustible. In section 1.2.3 some possible nuclear reactions are given that can be used in future fusion devices and there something will be said about the resources.

Like with every energy production method there are some risks, although in fusion power plants only local incidents can happen. Probably the most dangerous risk is the leakage of radioactive tritium (see section 1.2.3) but this will be only on a local scale. Moreover this will be only a risk for the first generation of power plants. In future generations one hopes to use fusion reactions without tritium. Catastrophic incidents like Chernobyl are almost impossible because any failure of a reactor component during the fusion process will result in the breakdown of this fusion process, thereby cancelling the risk of dramatic chain reactions. This because very specific conditions are needed to sustain fusion reactions. The complexity of the machine and functioning will also prevent the use of nuclear fusion technology in nuclear weapon industry .

1.1.4 A note on the way of living

Before going deeper into the fascinating world of fusion a few thoughts can be made. From the dawn of mankind till the present day humans were and still are strongly dependent on fossil fuels for their energy supply. Nevertheless it has become clear that this form of energy resources does not have a bright future ahead. Instead we will need new ways of energy production which are

[4] a lot of research goes to the "transmutation of radioactive waste" whereby highly radioactive elements are transformed into radioactive safe elements.

[5] an area of 632 km^2 and 5250 km^2 have been flooded for the construction of the Three Gorges Dam in China and respectively the Aswan Dam in Egypt.

meanwhile also sustainable, efficient, clean and save. Nuclear fusion can be such a candidate for this goal. But whatever the outcome will be, the most important thing we as, responsible beings, need to do is to change our way of living. It is good to have the ideal energy supply but it would be better if we used our energy wisely. We cannot affort us to spill energy. If everybody in the world would have the same ecological footprint as the mean Westerner, planet Earth won't be enough, with or without fusion ...

1.2 Nuclear fusion

1.2.1 Basic principles of nuclear fusion

As can be seen in figure 1.2 Fe has the highest binding energy per nucleon, which makes it a very stable element. Now it is possible to form new elements on two different ways. The first way is by taking the nucleus of an element to the right of iron in the graph and trigger a so–called fission process (e.g. by bombarding the nucleus with neutrons). This will result in the splitting (i.e. fission) of the original nucleus into two daughter nuclei which are more stable and thereby release energy. Generaly one speaks about nuclear fission. This physical process takes place in nuclear fission power plants (see also section 1.1.3).

The second way is kind of the opposite of nuclear fission: instead of splitting nuclei, nuclei are fused together. If one takes two elements to the left of iron in the graph and succeeds in bringing them close enough to each other both elements will fuse into one new element. This new element will have a higher binding energy per nucleon and hence will be more stable. As a result of this increase of stability energy will be released. One calls this merging process of two nuclei into one single nucleus simply **nuclear fusion**. The release of energy can be explained by the mass defect. The definition states that[6]:

"The mass defect is the amount by which the mass of an atomic nucleus is less than the sum of the masses of its constituent particles."

In practice this means that the mass defect Δm is the difference between the sum of masses of the constituting protons m_p and neutrons m_n of the nucleus and the experimental measured mass of the nucleus m_{exp}. Or in formula form:

$$\Delta m = (Zm_p - Nm_n) - m_{exp}$$

with Z the number of protons and N the number of neutrons. If we use Einstein's relation between mass and energy we can calculate the amount of energy released ΔE is:

$$\Delta E = \Delta m c^2$$

with c the speed of light in vacuum.

This looks all fine, we have an idea of the amount of energy released during fusion. The only thing that needs to be done is to fuse two appropriate light nuclei into one nucleus (more information on the possible nuclear reactions that can be used is given in section 1.2.3). Unfortunatly, as often in live, things doesn't go that easy. This thing is called the Coulomb Barrier.

1.2.2 The Coulomb barrier

The major challenge of fusion is that one needs to bring two positively charged nuclei close enough to each other in order that fusion can take place. As we al learned in kindergarten two equally charged objects tend to repell each other. Figure 1.3a shows the typical potential, consisting of the Coulomb potential and the strong force potential, for a proton–proton reaction. The peak in this potential is caused by the Coulomb force which acts as a barrier for fusing

[6] see for example `http://www.wolframalpha.com/input/?i=mass+defect`

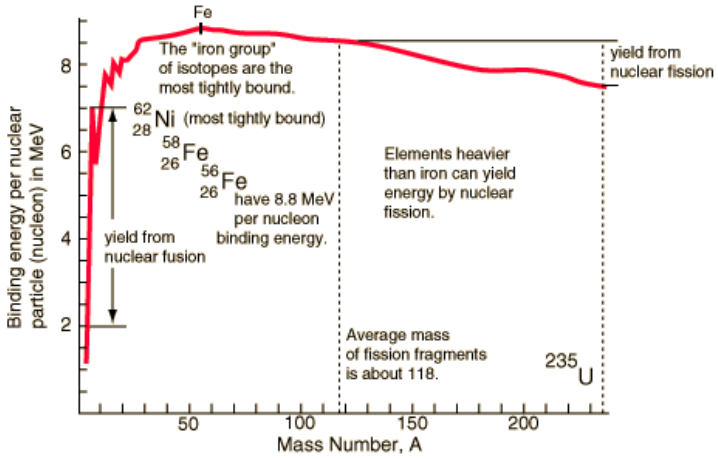

Figure 1.2: Binding energy per nucleon [5].

particles. Therefore one also speaks about the **Coulomb barrier**. But as one can see it is possible to overcome this energy barrier such that the nuclear force takes over and accomplishes the fusion reaction. To this end the fusing nuclei will need to have sufficient energy. A simple classical calculation shows roughly how much energy is required.

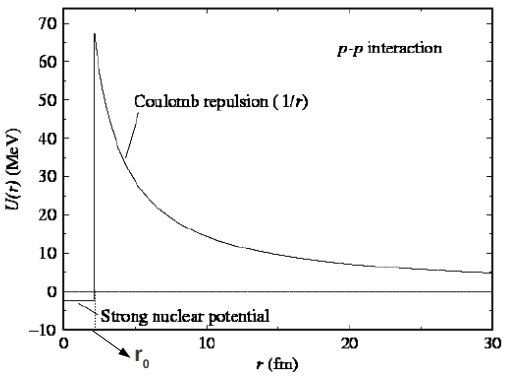

(a) The potential barrier for a proton–proton reaction. The Coulomb force works repulsive. The nuclear strong force works attractive [6].

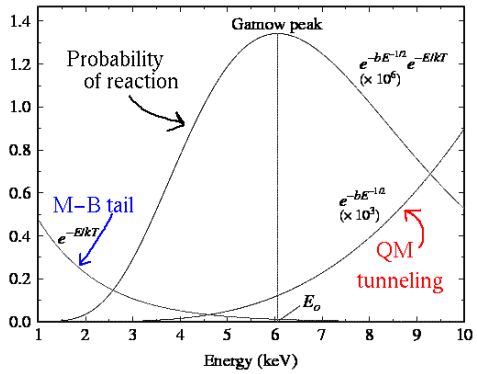

(b) The combined effect of the high–energy tail of the Maxwell–Boltzmann distribution with the tunneling probability results in the so–called Gamow–peak [6].

Figure 1.3: The Coulomb barrier and the probability to tunnel through it.

The potential has a maximum which the fusing nuclei need to overcome before actual fusion can take place. We call the distance corresponding with this peak r_0 and hence the potential energy here amounts to:

$$U_{max} = \frac{1}{4\pi\epsilon_0}\frac{q_1 q_2}{r_0} \tag{1.1}$$

where q_i is the nuclear charge of nucleus i and ϵ_0 the permittivity of free space.

As an example one takes the proton–proton reaction with typical values $q_1 = q_2 = e$ and $r_0 = 2\,.\,10^{-15}m$. Using equation (1.1) one can find that the maximum of the Coulomb barrier U_{max} for the proton–proton reaction is roughly 350 keV. Hence the particles will need to have at least a kinetic energy equal to U_{max} in order to overcome the Coulomb barrier. In classical thermodynamics this (thermal) kinetic energy corresponds to $\frac{3T}{2}$ (we omit the Boltzmann factor). The temperature corresponding with this kinetic energy is about 10^{10} K. Compare this with our sun's core temperature of about $15\,.\,10^6$ K and it is clear that one is dealing with an incredible

high temperature! Fortunately this is not the whole story. In reality the velocities of particles at a certain temperature are following a Maxwell–Boltzmann distribution. As a consequence the high energy tail of such a distribution will have higher kinetic energies than the mean particle velocity. Hence fusion reactions will start at lower temperatures due to these higher energy particles. Another important aspect that comes into play is the quantum mechanical nature of fusion reactions in the disguise of quantum tunneling. This tunneling effect allows atoms to penetrate through the Coulomb barrier. More information about the exact treatment of quantum tunneling can be found in more specialised literature. In figure 1.3b one can see the combined effect of the high energy tail of the Maxwell–Boltzmann distribution and the tunneling effect. The result is the so–called Gamow–peak which gives the energy for which nuclear fusion is most probable. The result is that fusion sets in "already" for energies of $3 - 10\,\mathrm{keV}$ for the proton–proton reaction. Mention that this corresponds with temperatures of a few tens of million Kelvin ($E = k_B T$). At these high temperatures materials are in the so–called fourth state of matter: **plasma**.

Nuclear fusion becomes more realistic. But still these high temperatures explains immediately the major problem of nuclear fusion. No material can ever withstand these high temperatures which make it hard to confine the actual fusion plasma. Mankind has thought about this confinement problem and has proposed some solutions, which will be overviewed in section 1.2.4.

1.2.3 Nuclear reactions

Astrophysical fusion reactions

The proton–proton chain In every star this process takes place. It is the dominant process in stars with masses comparable and smaller than our Sun's mass. The proton–proton chain goes in a few steps and there our some different reaction processes possible. Here we only discuss the main process in our Sun (at a rate of 86%):

1. $p + p \rightarrow D + e^+ + \nu + 0.42\,\mathrm{MeV}$
2. $e^- + e^+ \rightarrow 2\gamma + 1.02\,\mathrm{MeV}$
3. $D + p \rightarrow {}^3\mathrm{He} + \gamma + 5.49\,\mathrm{MeV}$
4. ${}^3\mathrm{He} + {}^3\mathrm{He} \rightarrow \alpha + 2p + 12.86\,\mathrm{MeV}$

Net result: $4p \rightarrow \alpha + 2e^+ + 2\nu + 26.7\,\mathrm{MeV}$

CNO–cycle This process becomes dominant in stars which are heavier than the Sun. There are several variants possible. Here we only discuss the most important one:

1. ${}^{12}\mathrm{C} + p \rightarrow {}^{13}\mathrm{N} + \gamma + 1.95\,\mathrm{MeV}$
2. ${}^{13}\mathrm{N} \rightarrow {}^{12}\mathrm{C} + e^+ + \nu + 2.22\,\mathrm{MeV}$
3. ${}^{13}\mathrm{C} + p \rightarrow {}^{14}\mathrm{N} + \gamma + 7.54\,\mathrm{MeV}$
4. ${}^{14}\mathrm{N} + p \rightarrow {}^{15}\mathrm{O} + \gamma + 7.35\,\mathrm{MeV}$
5. ${}^{15}\mathrm{O} \rightarrow {}^{15}\mathrm{N} + e^+ + \nu + 2.75\,\mathrm{MeV}$
6. ${}^{15}\mathrm{N} + p \rightarrow {}^{12}\mathrm{C} + \alpha + 4.96\,\mathrm{MeV}$

Net result: $4p \rightarrow \alpha + 2e^+ + 2\nu + 26.7\,\mathrm{MeV}$
Notice that the net result of the proton–proton chain and the CNO–cycle is the same. The elements C, N and O just act as catalysts in the fusion process.

Terrestial fusion reactions

D–D–reaction The D–D–reaction goes as follows:

$$D + D \rightarrow {}^3\mathrm{He} + n + 3.27\,\mathrm{MeV} \tag{1.2}$$
$$\rightarrow T + p + 4.00\,\mathrm{MeV} \tag{1.3}$$

followed by

$${}^3\mathrm{He} + D \rightarrow \alpha + p + 18.4\,\mathrm{MeV} \tag{1.4}$$
$$T + D \rightarrow \alpha + n + 17.6\,\mathrm{MeV} \tag{1.5}$$

Reaction (1.2) is called the neutron–branch, reaction (1.3) is called the proton–branch and they both have a probability of 50%. In figure 1.4 one can find the reaction rates for $D - D$, ^{3}He–D and $T - D$. In the energy range that is practical feasible for the moment $T - D$ comes out as the best candidate for fusion. It has also the highest energy production of the three reactions. Untill now only two tokamaks were capable of fusing $T - D$, this was JET and TFTR (which is now dismanteled). In COMPASS protons are fused together to form deuterium. One can also see reactions (1.2) and (1.3) together with reactions (1.4) and (1.5) as one global reactions:

$$6D \rightarrow 2\alpha + 2n + 43.2\,\mathrm{MeV} \tag{1.6}$$

Hereby T and ^{3}He actually act as catalysts in the global reaction. Hence they should be added from the start in suitable quantities. The main advantage of this reaction is that one needs to supply T only once. The disadvantage is the rather low fusion energy density for the same plasma pressure compared to the case of $D - T$ fusion.

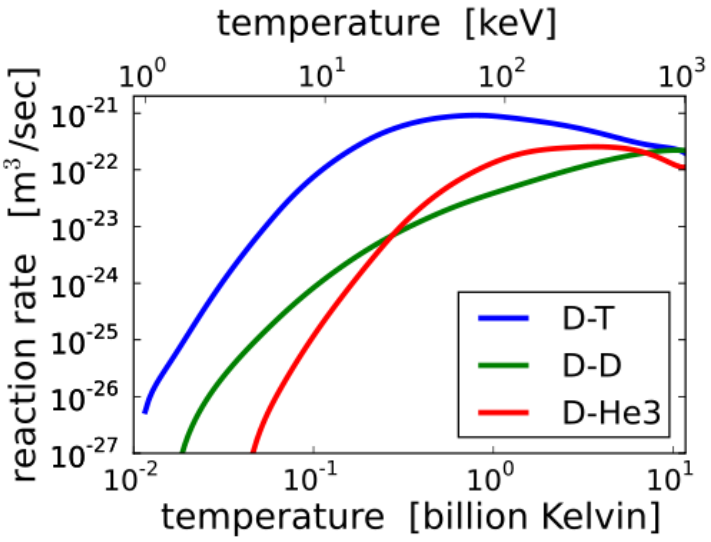

Figure 1.4: Reaction rate for some possible fusion reactions [7].

We now return to the discussion of resources for nuclear fusion (see section 1.1.3). For the $D - D$–reaction one needs deuterium which is an isotope of hydrogen. In natural water 0.015% of all the water molecules has at least one of the two hydrogen atoms replaced by a deuterium atom. It is estimated that there is a natural reserve of deuterium for about 150 billion years which is quasi inexhaustible. Tritium on the other hand is radioactive and short–lived (12.32 years). Due to this short life time it is only present in negligible amounts (mostly in the upper atmosphere where it is created by cosmic rays). Hence tritium cannot be extracted from nature

and must be obtained by an alternative way. Such a way can be the breeding of tritium from lithium. To this end a lithium blanket needs to be placed around the reactor and with the aid of the neutrons released during fusion reactions one gets tritium by:

$$^6\mathrm{Li} + n \rightarrow T + \alpha + 4.9\,\mathrm{MeV} \tag{1.7}$$

$$\text{or} \tag{1.8}$$

$$^7\mathrm{Li} + n \rightarrow T + n + \alpha + 2.5\,\mathrm{MeV} \tag{1.9}$$

Lithium resources in the crust of the earth are estimated at some few 100 years. Above lithium is used in many electronical applications such as batteries, computers, ... and the demand for lithium keeps rising. So lithium resources will run out soon. But luckily there is also lithium present in sea water. If technologies for extracting lithium from sea water becomes more efficient and cheaper one will have lithium for about some 60 million year.

Concerning the resources one can conclude that the resources for the $D-T$ reaction are quasi inexhaustible. Planet Earth provides us the necessary fuels for tens of millions of years.

Future reactions The little radioactive waste produced indirectly during fusion reactions is due to induced neutron–reactions. The neutrons released during for example (1.5) are neutrally charged and can leave the confined plasma (see section 2.1.1) unhindered. These neutrons will be stopped through collisions with the atoms of the surrounding material of the reactor. These neutron–collisions[7] can activate the reactor material and hence are inducing indirectly radioactivity. This issue can be reduced by selecting the right reactor materials (i.e. materials which are relatively insensitive to neutron–activation). But the best way to solve this problem is to make use of fusion reactions without the production of neutrons. Such reactions are:

$$D + {}^3\mathrm{He} \rightarrow \alpha + p + 18.4\,\mathrm{MeV} \tag{1.10}$$

$$\text{or}$$

$$^{11}\mathrm{B} + p \rightarrow 3\alpha + 8.7\,\mathrm{MeV} \tag{1.11}$$

Currently these reactions are technically not feasible.

1.2.4 Fusion in practice

The main problem that one needs to fix is the confinement of the high temperature plasma in order to sustain sufficient fusion reactions and to prevent contact between the plasma and the reactor wall. One can distinguish between three kinds of confinement: gravitational, inertial and magnetic confinement.

Gravitational confinement fusion

Actually erverybody knows or better said experiences this form of fusion because it is the way our Sun and all the other stars produce their energy. Stars are simply said gaint balls of plasma which are held together by gravity. In a star's core gravity is so strong that atoms obtain sufficient high energies and velocities in such a way that the inner part is actually ionised. In fact, conditions are just wright to enable fusion reactions to ignite. The produced fusion energy gives the particles the tendency to expand from the core. Eventually this pressure induced expansion is counterbalanced with the collapsing effect of gravity. This makes stars, especially main sequence stars, steady fusion reactors. Gravitational fusion only takes places if objects have masses of about 75 times the mass of Jupiter [8]. Jupiters mass is estimated at $1.899\,10^{27}\,\mathrm{kg}$, about 300 times the mass of Planet Earth, so gravitational fusion is out of reach.

[7] Neutron–activation becomes more important when high neutron fluxes are present which will be the case in future fusion power plants.

Inertial confinement fusion

Fusion reactions are triggered by heating and compressing a small fuel pellet with the aid of high power lasers. In figure 1.5 the principle is sketched briefly. The following steps take place [9]:

1. Laser beams or laser–produced X–rays rapidly heat the surface of the fusion target, forming a surrounding plasma envelope.
2. The fuel is compressed by the rocket–like blowoff of the hot surface material.
3. During the final part of the capsule implosion, the fuel core reaches 20 times the density of lead and ignites at $100 \cdot 10^6$ K.
4. Thermonuclear burn spreads rapidly through the compressed fuel, yielding many times the input energy.

For more details on inertial confinement fusion we refer to more advanced literature in this topic.

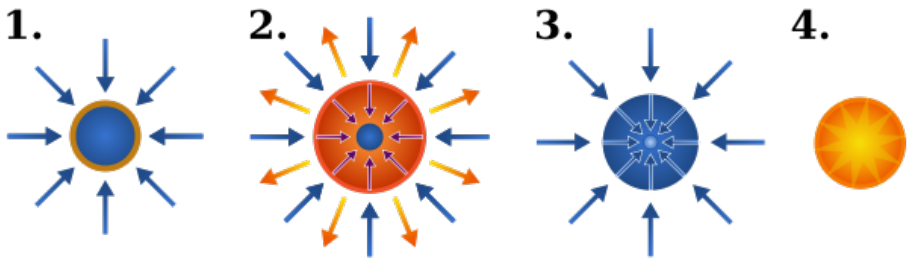

Figure 1.5: Schematic of the stages of inertial confinement fusion using lasers. The blue arrows represent radiation; orange is blowoff; purple is inwardly transported thermal energy [9].

Magnetic confinement fusion

Magnetic confinement is the way one hopes to realise future fusion reactors. Because there exist no materials that can withstand the high temperatures needed for nuclear fusion, one can make use of magnetic fields. Electrically charged particles have the tendency to follow magnetic field lines (see section 2.1.1). If one can create an appropriate magnetic field configuration it is possible to keep the hot plasma away from the reactor walls and hence to confine the plasma. Over the years different kinds of magnetic fusion devices have been developed:

- **Tokamaks**
  Most research has gone to this type of possible fusion reactors. The word tokamak is a Russian acronym of тороидальная камера с магнитными катушками (**to**roidalnaya **ka**mera **ma**gnitnaya **k**atuschka), which means toroidal chamber with magnetic coils. The tokamak concept was invented in the 1950's by the Russians Andrei Sakharov and Igor Tamm. The measurements performed in this thesis were obtained on COMPASS which is an experimental fusion machine of the tokamak type. The next chapter will go deeper into the tokamak concept and COMPASS.

- **Stellerators**
  The main difference with the tokamak concept is that the confining magnetic field is only produced by external field coils in the case of stellerators. As a consequence one need special shaped coils which are technically difficult to fabricate. This is the main disadvantage of stellerators with respect to tokamaks. On the other hand it is not necessary to drive a toroidal current for the confinement in stellerators (which is necessary with the tokamak concept, see section 2.1). This induced current can be a possible source for instabilities

which can disrupt the fusion plasma prematurely. The research about stellerators is not as far developed as tokamak research. The Large Helical Device (in Toki, Gifu, Japan) and the Wendelstein 7-X (in Greifswald, Germany), which is now being build, are the most promising devices in their kind for deeper understanding the concept of stellerators. We refer to more advanced literature for more information about stellerators.

- **Spherical tokamaks**
  Spherical tokamaks are actually a kind of varation of normal torus–shaped tokamaks. As the name suggests they are more spherically shaped whereby they have a small aspect ratio approaching to one (see 2.1.1). The main advantage would be an more efficient energy production due to the more compact form. The research of spherical tokamaks is rather new and started in 1991 with the Small Tight Aspect Ratio Tokamak (START) in Culham, UK. In 1999 START was followed by the Mega Amp Spherical Tokamak (MAST) also in Culham, UK.

Irrespective of the kind of tokamak that will be used the first operating fusion power plants will probably work with $D-T$ fuel. In figure 1.6 one can find a schematic view of a future power plant.

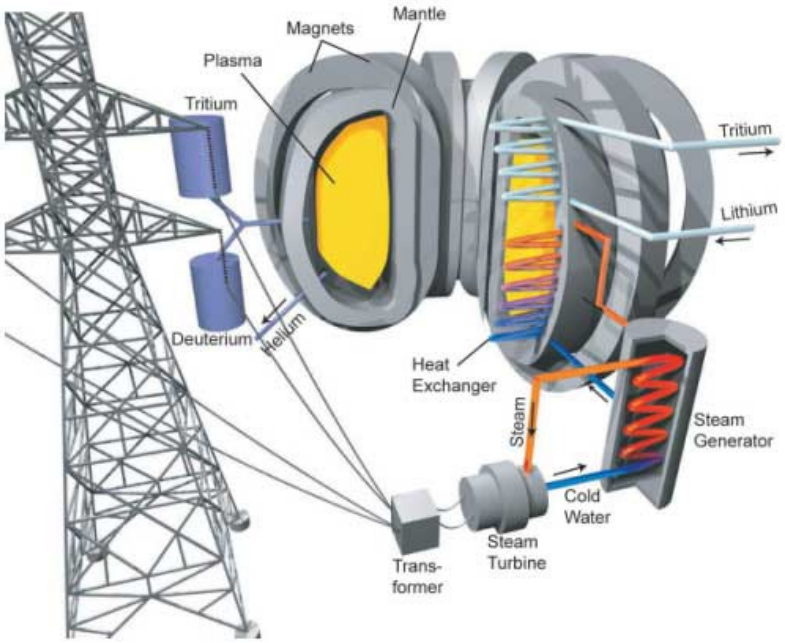

Figure 1.6: Example of a future fusion power plant [10].

Chapter 2

Tokamaks

2.1 Tokamak concept

2.1.1 Confinement by magnetic fields

The equation of motion of a charged particle in a magnetic field is given by:

$$m\frac{d\vec{v}}{dt} = q\vec{v} \times \vec{B} + \vec{F} \tag{2.1}$$

where $\vec{F}$ can represent the electrical force $q\vec{E}$.

In general the motion of a charged particle will consist of a gyration motion around a instantaneous gyration centre with cyclotron frequency $\vec{\omega_c}$ [11]:

$$\vec{\omega_c} = -\frac{q\vec{B}}{m} \tag{2.2}$$

and a corresponding Larmor radius:

$$\rho = \frac{m|\vec{v}|}{q|\vec{B}|} \tag{2.3}$$

The instantaneous gyration centre moves on a parabolic orbit with velocity $\vec{v_g}$:

$$\vec{v_g} = \vec{v_{g,||}} + \vec{v_D} \tag{2.4}$$

with

$$\vec{v_{g,||}} = \vec{v_{||,0}} + \frac{\vec{F_{||}}}{m}t \tag{2.5}$$

which is the velocity component parallel to the magnetic field lines, and

$$\vec{v_D} = \frac{\vec{F} \times \vec{B}}{q|\vec{B}|^2} \tag{2.6}$$

which is the velocity component perpendicular to the magnetic field lines, also called the drift velocity.

It can be easliy shown that in the presence of only a magnetic field ($\vec{F} = \vec{0}$) the charged particles move at a constant velocity along the magnetic field lines whereby they make a gyration around these magnetic field lines. Hence charged particles are confined to move in parallel with the field lines. If one could make a pipe with the magnetic field lines parallel to the axis of axial symmetry of the pipe the particles would be confined in the pipe (see figure 2.1). Of course the particles are still able to escape the pipe at the ends. The next logical step to prevent this particle loss is to close both ends of the pipe to each other. This configuration is called a torus.

For a torus one defines special coordinates (poloidal and toroidal coordinates) as seen in figure 2.2. In practice coils along the poloidal direction of the torus carry currents which induces a magnetic field in the toroidal direction. Therefore these coils are called toroidal field coils (TFC). Furthermore one defines the ratio of the major radius to the minor radius of the tokamak (see figure 2.2) as the aspect ratio.

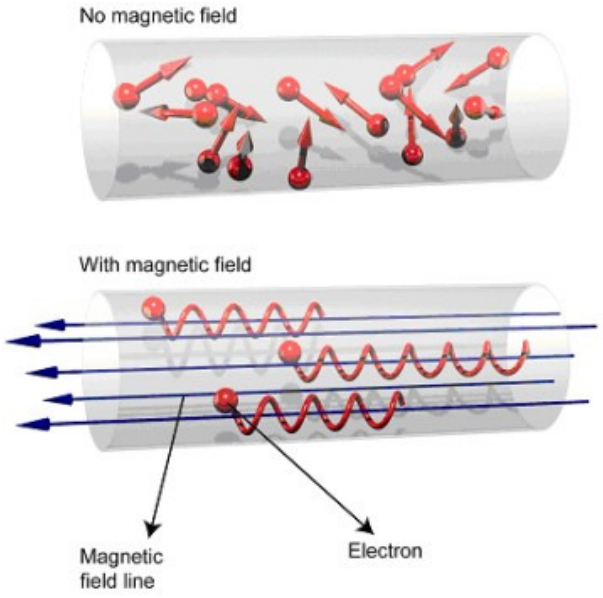

Figure 2.1: Charged particles move along the magnetic field lines. Here the case is shown for electrons [12].

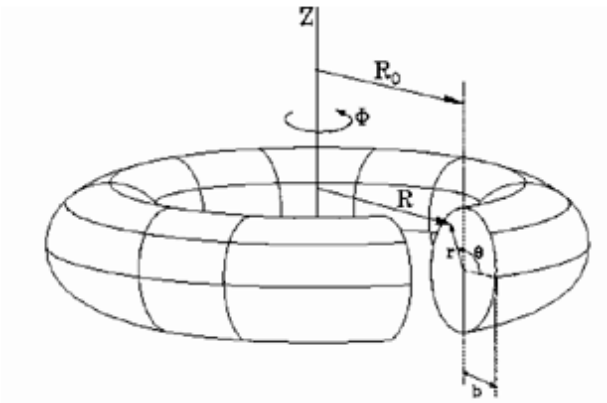

Figure 2.2: Coordinates in a tokamak. ϕ is the toroidal coordinate, θ the poloidal coordinate. R_0 is called the major radius of the tokamak and b the minor radius. The z–axis is the axis of axial symmetry [13].

This toroidal magnetic field induced by these TFC is not homogeneous throughout the torus. The magnetic field decrease as one moves away from the axis of axial symmetry of the torus[1]. This magnetic field gradient induces a drift velocity given by [11]:

$$\vec{v_D} = \frac{k_B T}{q|B|^4}(\vec{B} \times \nabla |B|^2) \tag{2.7}$$

$$= \frac{4\pi k_B T}{q\mu_0 I_p} \tag{2.8}$$

[1] This can be verified through Ampère's law: $\oint_C \vec{H} \cdot \mathrm{d}\vec{l} = \int\int_S \vec{J} \cdot \mathrm{d}\vec{S}$

with μ_0 the permeability in vacuum and I_p the poloidal current.

Equation (2.8) shows that this dirft velocity induces a charge separation because of the $1/q$ dependence. As a consequence the separation of the electrons and the positive ions causes the formation of an electrical field $\vec{E}$ within the plasma. This electrical field in turn induces a so–called Hall–drift of the paticles with a drift velocity of (see equation (2.6)):

$$\vec{v_D} = \frac{\vec{E} \times \vec{B}}{|B|^2}$$

One can see that this final drift is charge independent. And as can be seen in figure 2.3 this drift is oriented outwards the plasma. Hence the whole plasma drifts away from the main axis of the torus and the plasma becomes unstable.

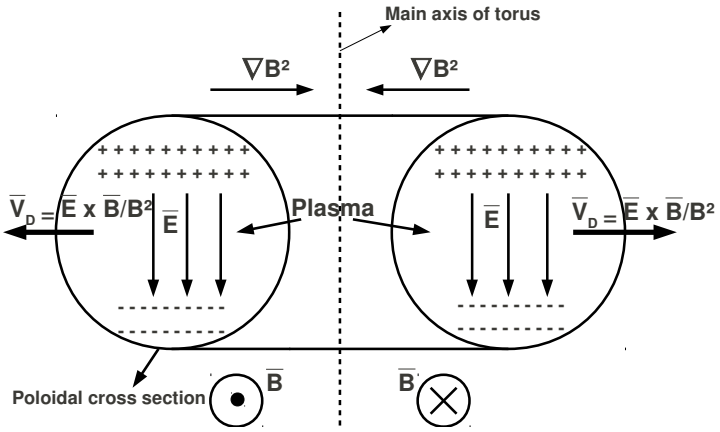

Figure 2.3: Poloidal cross section of a torus. The magnetic field increase towards the main axis of the torus. The resulting Hall–drift induces a total outward drift of the plasma. Hence the plasma is unstable in the pure torus configuration.

As possible cure for this problem is to increase the poloidal current I_p of the TFCs and hence to decrease the particle drift (see (2.8)). But normally this is not the method used because higher currents in the poloidal coils requires better conducting materials and cooling systems. It is better to modify the magnetic field itself such that the outward drift is counterbalanced. This is done by inducing also a poloidal component $\vec{B_p}$ to the magnetic field. A way to create this poloidal field components is to drive a current along the toroidal direction of the torus and hence inducing a poloidal magnetic field. In practice this poloidal magnetic field is created by toroidal coils wrapped around the torus axis which constitute the primary winding of a transformer. The plasma itself then serves as the secondary winding and hence a toroidal current is induced into the plasma.

The combined effect of the toroidal and poloidal magnetic field lines results in field lines spiralling helically around the torus (see figure 2.4a) forming closed magnetic flux surfaces. It can be proven that charged particles are following these magnetic field lines around the torus. Particles can only move radially across the magnetic flux surfaces (i.e. the particles are drifting away) through e.g. collisions, MHD–instabilities, residual $\vec{E} \times \vec{B}$–drift, ... This method of confining plasma particles with current–induced magnetic fields in a torus–shaped configuration is what we call the tokamak–concept.

In figure 2.4b one can find a typical magnetic field system of a tokamak. Above the toroidal field coils and the inner poloidal field coils of the transformer there could also be some additional field coils present in order to improve the flexibility of the experiments. It is important to notice that tokamaks can only operate in a pulsating mode. The reason is that the transformer cannot induce continuously dc–current in the secondary winding (here the plasma).

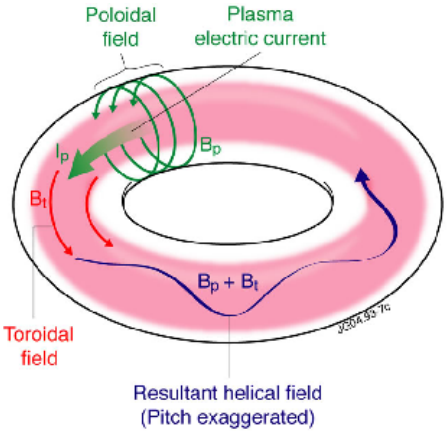

(a) Total resulting magnetic field of a tokamak. The toroidal magnetic field is generated by poloidal oriented coils. The poloidal magnetic field is generated by a current along the toroidal direction inside the plasma [14].

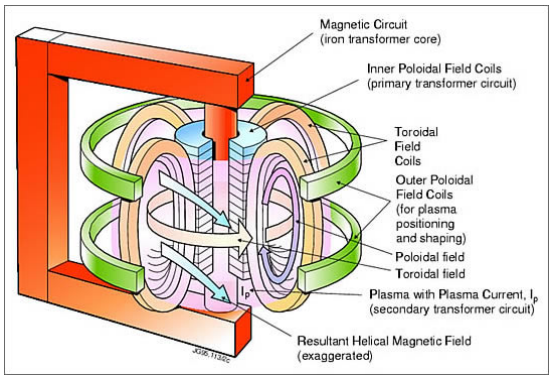

(b) Magnetic field system of a typical tokamak [15].

Figure 2.4: Magnetic field in tokamaks.

2.1.2 Edge plasma

The subject of this thesis is concerned with physical phenomena in the so–called **edge plasma**. It can be thought as the region in the neighbourhood of the Last Closed Flux Surface (LCFS) or separatrix. As the name already indicates the LCFS or separatrix is a border between two different plasma regions. Inside the LCFS plasma particles move on closed magnetic flux surfaces which define the confined plasma. Outside the separatrix the magnetic flux surfaces are actually also closed but they cross a solid surface from for instance a limiter or divertor (see below). Hence the plasma particles moving outside the LCFS will interact with these neutral solid surfaces or the colder neutral gas in front of it. This outer region is called the Scrape–Off Layer (SOL). As mentioned in the previous section plasma particles are allowed to cross the magnetic surface inside the confined plasma through indirect transport mechanism like e.g. diffusion. It are these escaped particles, called plasma exhaust, that make up the SOL and interact with the reactor walls, divertors, limiters, etc.

One of the main conditions for fusion to take place is the confinement of the plasma particles. Therefore the plasma needs to be shielded from the First Wall (FW) of the tokamak vessel in order to enhance fusion yield. Strong interaction of the plasma with the FW would introduce large amounts of impurities into the plasma and terminate the discharge. A first solution (and historically the oldest) is to use a so–called **limiter**. Simply said it can be considered as a first wall in front of the actual FW. A limiter is namely a barrier that is inserted into the SOL right up to the confined plasma and actually defines the LCFS (see figure 2.5). This limiter–configuration acts as a sink for plasma exhaust. The collection principle of limiters is based on the formation of a plasma sheath [16] (see section 3.2.5 for a brief introduction to the plasma sheath). The limiter will collect most of the escaped particles before they reach the FW. The main purpose of the limiter, seperating the confined plasma from the FW, is thus accomplished. But meanwhile the greatest disadvantage of limiters is revealed: the risk to introduce impurities. Bombardement of the limiter surface by plasma particles could directly introduce impurities into the core plasma and hence disrupt the discharge. A better approach is to modify the magnetic field lines such that the field lines of the SOL are directed to a preferred region of the FW. The particles are "diverted" to special designed target plates of the FW in a so-called divertor–region. The whole concept of modifying the field lines and designing a special divertor–region is simply called a **divertor** (see figure 2.5). It can be shown that the temperature and the density of the

plasma drops along the magnetic field lines of the SOL in the direction of the divertor–region [16]. Hence the divertor is capable to sustain the incident power load[2] and to act as a plasma exhaust sink. In contrast to limiters, released impurities cannot directly enter the plasma core because divertors are not in direct contact with the confined plasma. There are more advantages compared to limiters which will not be listed in this thesis work. A good introduction to the principle of divertors and limiters can be found in e.g. [16, 18, 19]. Nowadays most important tokamaks work with the divertor–principle.

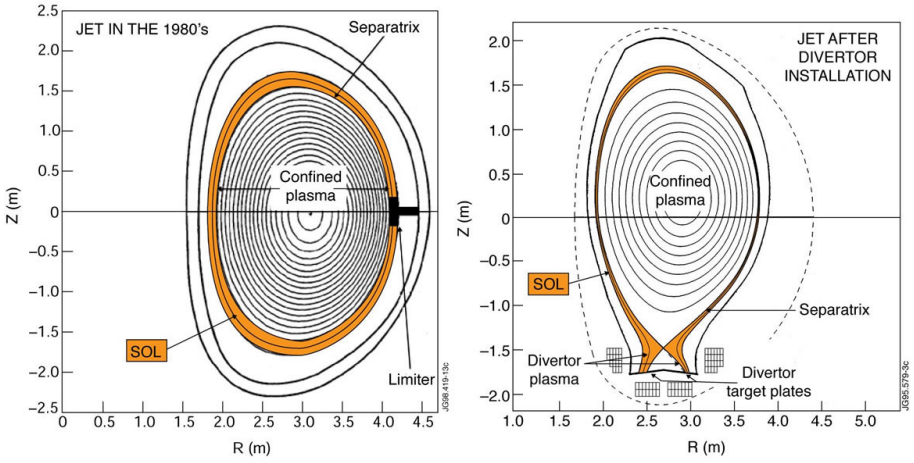

Figure 2.5: Poloidal cross section of a tokamak with a limiter configuration (left figure) or a divertor configuration (right figure) [18].

2.2 The COMPASS tokamak

2.2.1 A short historical overview

In this section we give a more detailed description of the COMPASS tokamak. COMPASS stands for **COMP**act **ASS**embly and is located at the Institute of Plasma Physics (IPP) in Prague. Originaly it was designed and installed in Culham Science Centre, UK in 1989. Based on his size COMPASS is in the category of the smaller fusion devices. Nevertheless it is of great importance in the development of the ITER project towards commercial fusion[3]. The reason is that COMPASS has a size and shape such that is corresponds to one tenth of the ITER future device (see figure 2.6a). This makes it rather unique because there are only two other tokamaks with comparable configurations to ITER which are bigger: JET in Culham, UK and ASDEX-U in Garching, Germany. The results from these two tokamaks can be compared with the results of COMPASS. Hence one can examine scaling relations which are very important for the construction of ITER and future fusion devices. Due to the start of a new tokamak project in Culham, called MAST, and insufficient resources COMPASS was offered for free to the IPP. Hence COMPASS moved in the autumn of 2007 from Culham to Prague where the first plasma was generated on 12 December 2008. Meanwhile the former tokamak CASTOR present at IPP moved to the Technical Institute of Prague and was renamed GOLEM. Chapter 8 is devoted to the latter tokamak.

[2]Not all materials are suited to be used as divertor target–plates. The choice of appropriate materials which can withstand high power loads is a research branche on its own in fusion technology. For a good introduction to fusion materials see e.g. [17].

[3]More information on ITER and future fusion can be found on [20].

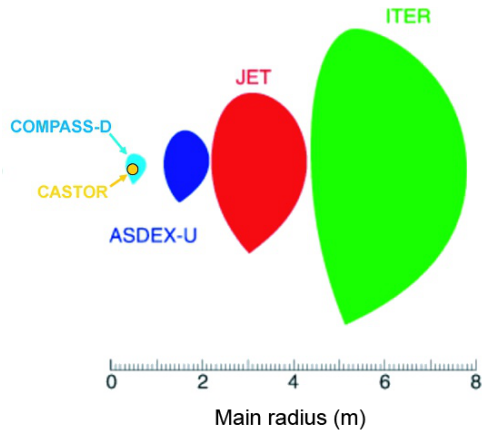

(a) Comparison of the plasma cross–section of tokamak with ITER–relevant plasma shapes [21].

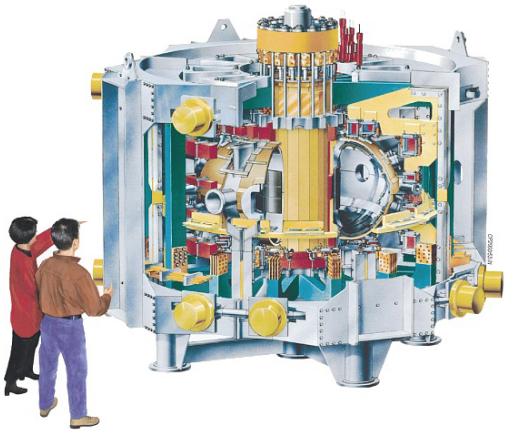

(b) Section of COMPASS [21].

Figure 2.6: The COMPASS tokamak.

2.2.2 A short technical overview

In table 2.1 one can find an overview of the most important parameters of COMPASS. Important to note is that the current plasma shape is not the ITER–like D–shape. During the campaign at IPP Prague all the data were obtained from a circular–shaped plasma.

Table 2.1: Most important parameters of COMPASS [21].

Parameters	Current values	Expected max values
Major radius R_0	0.56 m	0.56 m
Minor radius a	0.18 m	0.23 m
Plasma current I_p (max)	100 kA	350 kA
Magnetic field B_t (max)	1.8 T	2.1 T
Vacuum pressure	$5 \,.\, 10^{-8}$ Pa	$1 \,.\, 10^{-8}$ Pa
Elongation	1	1.8
Plasma shape	circular	D, SND, elliptical, circular
Pulse length	0.1 s	1 s
Lower–hybrid current drive P_{LH} 1.3 GHz	0 MW	0.4 MW
Neutral beam heating P_{NBI} 40 keV	0 MW	2×0.3 MW

2.2.3 Available diagnostics

Only a brief discussion of the avaible diagnostics at COMPASS is given here. More information can be found at [22].

Magnetic diagnostics

A wide variety of magnetic diagnostics are available on COMPASS. In figure 2.7 one can find an overview. For more details about the different kind of magnetic diagnostics we refer to more advanced literature (e.g. [23], chapter 2) or the webpages of COMPASS ([22]). The main goal of magnetics is to determine plasma current, plasma density, total plasma current, plasma position, plasma shape, plasma conductivity, total energy content and MHD instabilities.

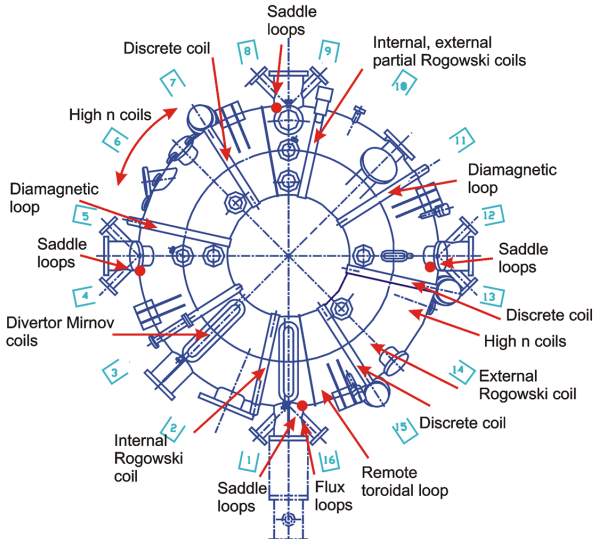

Figure 2.7: Magnetic diagnostic system on COMPASS [22].

We go a little bit deeper into the basic operation of some magnetic diagnostics because these kind of diagnostics are frequently used aside the electrical probes, especially for the determination of the plasma position (see section 5.3). Basically most magnetic diagnostics consist of a coil of conducting wire[4]. In figure 2.8 on can find two of the many variantions of magnetic coil configurations. Essentially, magnetic coils produce, through Faraday's law, a voltage signal which is proportional to (the time derivative of) the magnetic field (e.g. as in figure 2.8a) or to (the time derivative of) the encircled current (e.g. as in figure 2.8b).

Assuming that the plasma is in magnetohydrodynamic equilibrium implies that there is a balance between the kinetic pressure force density and the electromagnetic force density which is expressed as:

$$\nabla \cdot \boldsymbol{T} = 0 \tag{2.9}$$

with

$$\boldsymbol{T} = \left(p + \frac{B^2}{2\mu_0}\right)\mathbf{1} - \frac{\boldsymbol{BB}}{\mu_0} \tag{2.10}$$

Equation (2.9) can be solved in cylindrical coordinates with Fourier analysis (which is satisfied for most tokamaks). It can be shown (see for example [23]) that solving equation (2.9) up to the first order term of the fourier expansion of the magnetic field, gives a relation between the magnetic field and the plasma position. Hence measurements of the magnetic field by appropriate magnetic field coils make it possible to extract information about the position of the plasma column.

Spectroscopic diagnostics

- **Fast VIS camera**
  A camera that measures the visible light in a tangential direction of the plasma column. It is used to observe the plasma–wall interaction. The camera pictures are very usefull to make a movie from the discharge.

- **Multichannel optical system for visible plasma radiation measurement**
  This is an experimental set–up with spectrometers and photomultipliers. One can deter-

[4] An other category of magnetic diagnostics consists of semiconductor plates which are inserted inside the plasma. The physical process determining the output of these diagnostics are based on the *Hall–effect*. Therefore these measuring devices are called Hall–probes. For more information see also [23].

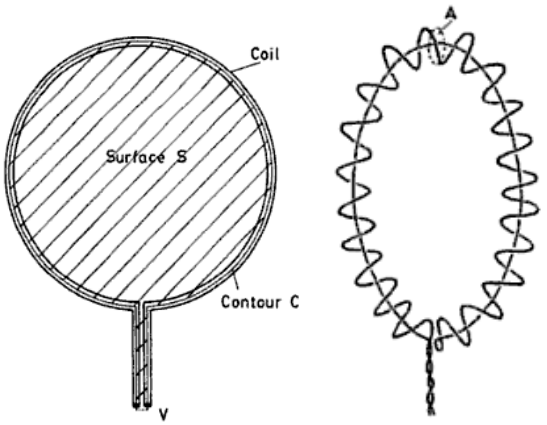

(a) The most basic form of magnetic coil.

(b) A Rogowski coil, a more advanced form of a magnetic coil.

Figure 2.8: Two examples of coil configurations frequently used on tokamaks [23].

mine hydrogen and impurity emission and their evolution during the discharges. Furthermore integral plasma radiation in the visible range both from the plasma core and from the plasma edge can be measured. Above it is possible to observe specific spectral lines, like that from hydrogen or from the most intensive impurities (e.g. carbon).

- **Bolometry**
  With this diagnostic one measures the energy of the incident electromagnetic radiation. Bolometers are used in tokamaks to record the total radiated power covering a wide spectral range. It enables scientists to determine the total radiated power and to learn something about energy losses in the plasma.

- **Soft X–rays diagnostics**
  The soft X-ray diagnostic is used to monitor the distribution of radiated power in a soft X–ray spectral region. It is suitable to observe fast radiation events related to plasma instabilities.

- **Plasma rotation measurements**
  Based on the Doppler broading of spectral lines one can determine the toroidal and/or poloidal velocity of the plasma column. Herefor high–resolution spectrometers are necessary.

- **Thompson scattering**
  The combined effect of Thompson scattering and the Doppler effect makes it possible to determine the electron temperature and density of the plasma. The experimental set–up for Thompson scattering consist of a laser beam directed towards the plasma column. This diagnostic system was being installed during the experimental campaign.

Microwave diagnostics

- 2 mm **microwave interferometer**
  The phase shift is measured by comparing the phase of a microwave beam that passed through the plasma with the phase of a reference signal. It can be shown that this phase shift is proportional to electron density averaged along the tokamak diameter.

- **Electron cyclotron emision radiometer (ECE)**
  The electrons gyrate around the magnetic field lines and produce specific radiation at radiofrequencies. One can prove that the emission power of this radiation is proportional to the electron temperature. The system installed on COMPASS makes it possible to determine the radial profile of the electron temperature.

- **Microwave reflectometer**
  For this diagnostic one uses a microwave beam with a frequency for which the plasma is reflective. Now the frequency of this beam is related to the electron density. Hence the microwave reflectometer is very usefull to determine the profile of the electron density at the plasma edge.

Beam and particle diagnostics

These diagnostics were not available during the campaign. After the installation of the neutral beam injector one will start with installing these diagnostics. There will be three different kinds of beam and particle diagnostics: a **beam emission spectroscopy** sytem, an **atomic beam probe** and a **neutral particle analyzer**. The main goal of these diagnostics is to determine plasma density profiles, electron density fluctuations at the plasma edge, poloidal magnetic field perturbations and edge plasma current profiles.

Electrical probe diagnostics

For completeness we give here the two probe diagnostics available on COMPASS. Both systems were used to obtain the data for this thesis. Hence a more profound discussion will be given in the following chapters.

- **Divertor probe array**
  See section 5.1.

- **Reciprocating manipulator**
  See section 5.2.

2.2.4 Power supply

The amount of electrical power ($50 - 60\,\mathrm{MW}$) necessary to operate the tokamak is to big to acquire directly from the public grid. Therefore one needs to accumulate the required energy in advance. This is done with the aid of two fly–wheel generators. One is used for the operation of the toroidal field coils and the second for the poloidal field coils and (in future) additional heating systems.

For the moment the only heating method for the plasma on COMPASS is the ohmic heating induced by the plasma current. In November 2010 one will start with the installation of a neutral beam injector. This will increase significantly the heating capacity of the tokamak as can be seen in table 2.1. Further in the future one also hopes to install a lower–hybrid wave heating and current–drive system. This extra heating system will make it possible to operate the tokamak more continuously.

Cooling system

The large currents driven in the magnetic field coils are heating up these coils which reduce their efficiency. Hence one needs to cool the field coils sufficiently. At COMPASS a water–cooling system is in operation. The coils are cooled by demineralised and deionised water.

2.2.5 Vacuum system

There are three main steps in the process to ensure a sufficiently low vacuum for optimal plasma operation. In a first stage vacuum pumps are pumping out the air from the vessel till some pressure of 10^{-4} Pa. Before going to the next stage one first checks if there are no leaks. This is done by blowing from the outside systematically helium onto every part of the tokamak or diagnostic in contact with it. If there is a leakage the helium will penetrate the tokamak and will be pumped away by the vacuum pumps. Now one connects a mass detector to the vacuum pumps which is sensitive to helium. Hence the detection of helium means that there is some leak. If no leakages are found one can go to the next step of the entire vacuum process.

Sometimes it necessary to enter the vessel or to (re)install some diagnostics and hence one needs to break the vacuum. Every time the vacuum is broken the inner side of the tokamak becomes polluted by impurities (e.g. carbon, oxygen, ...). This can be caused by not using gloves to handle the materials or just by contact with the air. Hence one needs to remove these impurities that can undermine the vacuum and cause premature disruption of the plasma. The method for removing wall–absorped impurities is called "baking". So in a second stage one starts literally to "bake" the tokamak and the diagnostics. This is done by inducing a current through some parts of the tokamak or by putting heating elements around tokamak components and around the diagnostics. As a result the temperature of the vessel and surrounding diagnostics is brought to about $150 - 200\,^{\circ}$C and hence most of the impurities will be desorped from the surface of the inner side of the tokamak. Meanwhile the vacuum pumps keeps pumping and hence removes these desorped impurities. This method reduces pressure again with one to two orders of magnitude.

Finally in the last stage one fills the tokamak with helium (at a pressure of $1 - 10$ Pa) and one inserts an electrode into the vessel. This electrode is biased with respect to the vessel at a voltage of about $+500$ V (see figure 2.9). This will trigger a glow discharge inside the tokamak whereby the vessel will act as a cathode and the electrode as an anode. The discharge will ionize the helium atoms. As a consequence the electrons will be attracted to the electrode while the ionized helium atoms will be attracted to the vessel. The energy of the helium atoms is high enough to actually sputter the surface of the vessel and hence removing remaining impurities. The whole vacuum process must ensure a pressure of a few 10^{-6} Pa.

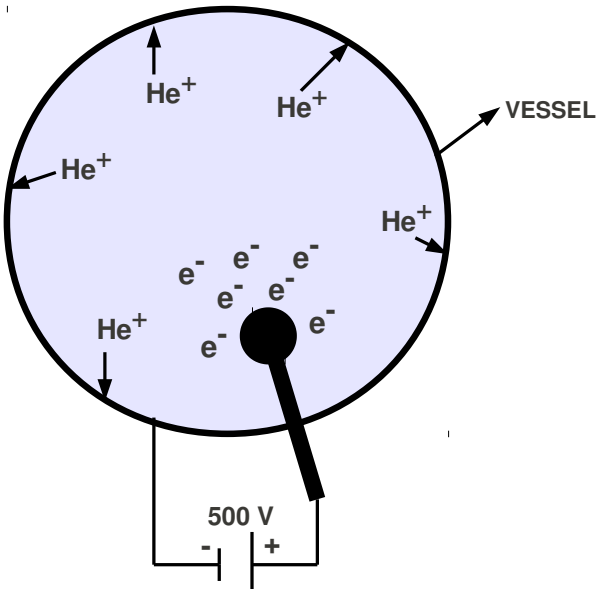

Figure 2.9: Basic scheme of the last stage of the vacuum process.

Part II

Electrical Probes in Theory

Chapter 3

The Langmuir probe

3.1 History

In general electrical probes are a very natural approach to determine some properties of the plasma under study. The basic principle is that one puts an electrode into the plasma and baises it to a certain voltage in order to collect plasma particles. From the measured currents and voltages one can determine different kind of plasma properties (e.g. the electron temperature). The fact that probes penetrate into the plasma is also their main disadvantage. The severe conditions inside the plasma can destroy the probe. Hence probes are limited to diagnose only the plasma edge in thermonuclear fusion devices where thermal loads are tolerable. Of course, in low temperature plasma physics one could probe deeper into the plasma without destroying it. Furthermore different kind of varieties of probe systems were developped in order to get information from deeper inside the plasma as for example the reciprocating manipulator (see section 5.2). Another difficulty about probes is the way how to interpret the obtained data. Often it is not justified to use the theories for the ideal non–magnetised case when strong magnetic fields are to be included (as in the case of tokamaks). Above, by introducing an electrode into the plasma, one will eventually alter the (local) plasma properties. Hence it is very important to know the influence of the probe on the raw data. Although at the end, how complicated the probe design and interpretation can be, most simple theoretical models are often a good first approximation. The most basic and oldest probe design is the Langmuir probe. It was invented by Irving Langmuir[1] in 1924. Langmuir probes are suitable to determine electron density, electron temperature and floating potential at the plasma edge.

3.2 Physics

3.2.1 Ideal $I - V$ characteristic

Since a plasma consists of charged particles there will be electrical fields and corresponding potentials present inside the plasma. The total potential arising from the ensemble of charged particles is called the plasma potential or space potential V_p. Now a Langmuir probe consist of an electrode which is put into the (edge of the) plasma. By biasing this electrode and measuring the corresponding current one can determine the $I - V$ characteristic. In figure 3.1 one can find a typical $I - V$–curve produced by a Langmuir probe measurement in an ideal homogeneous plasma without collisions and magnetic fields and where particles are collected at only one side of the probe. Basically the curve is made up of two currents: the ion current I_i and the electron current I_e. If no probe is inserted into the plasma these currents are determined by V_p.

[1] Irving Langmuir was a American physicist and chemist. He lived from 31 January 1881 till 16 August 1957. In 1932 he received the Nobel Prize in Chemistry. He originated the word plasma to ionized gasses. His name is also connected to electron density waves in plasmas, i.e. Langmuir waves.

I_i and I_e will then be equal to their unperturbed value which is called the saturation current I_s, given by:

$$\begin{aligned} I_s &= Aj_s \\ &= Aq \int v_x f(v)\, \mathrm{d}\vec{v} \\ &= Aqn \left(\frac{m}{2\pi T}\right)^{3/2} \int_0^{+\infty} v_x \exp\left(\frac{-mv_x^2}{2T}\right) \mathrm{d}v_x \int_{-\infty}^{+\infty} \exp\left(\frac{-mv_y^2}{2T}\right) \mathrm{d}v_y \int_{-\infty}^{+\infty} \exp\left(\frac{-mv_z^2}{2T}\right) \mathrm{d}v_z \\ &= \frac{1}{4} Aqn \sqrt{\frac{8T}{\pi m}} \\ &= \frac{1}{4} Aqn\bar{v} \end{aligned} \tag{3.1}$$

where we used a Maxwell–Boltzmann distribution $f(v)$ for the velocity. Furthermore we assumed that particles are only collected at one side of the probe, here particles arriving from the positive x–axis.

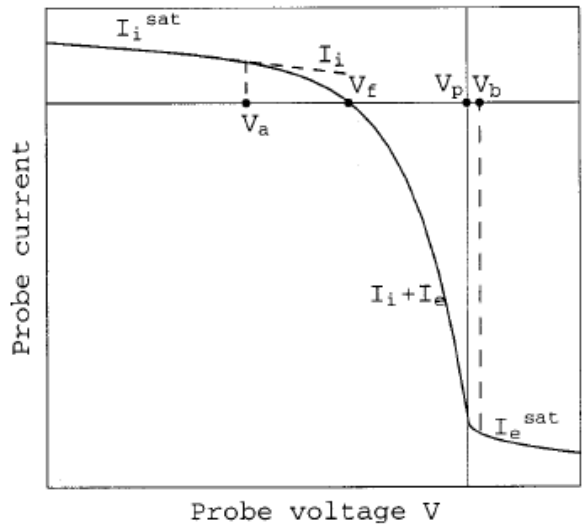

Figure 3.1: Ideal $I-V$–curve measured by a Langmuir probe. I_i^{sat} and I_e^{sat} corresponds to I_{is} and I_{es} respectively in the text. For $V < V_a$ the probe collects in the ion–saturation regime and for $V > V_b$ in the electron–saturation regime. The transition region is for $V_a < V < V_b$ [24].

Hence at the plasma potential the total current will be the sum of I_{es} and I_{is}:

$$I = \frac{1}{4} Ae(n_i\bar{v}_i - n_e\bar{v}_e) \tag{3.2}$$

In practice at V_p the total current will be almost equal to the electron saturation current:

$$I \approx -\frac{1}{4} Ae(n_e\bar{v}_e) = I_{es} \tag{3.3}$$

This because of the smallness of the ion saturation current. We can prove this by using the expressions for the saturation current (3.1):

$$\frac{|I_{is}|}{|I_{es}|} = \sqrt{\frac{T_i}{T_e}\frac{m_e}{m_i}} \tag{3.4}$$

Even for thermal equilibrium between ions and electrons ($T_i = T_e$) this ratio is about $1/43$ for

hydrogen. Hence the ion current can be neglected. Here one assumed that the collecting area for ions A_i and electrons A_e is the same. However, this will not be true when (strong) magnetic fields are taken into account (see section 3.2.4).

If one now increases V above V_p the ions will be repelled from the probe and more and more electrons will be collected. So one would expect an ever increasing electron current. Nevertheless from certain voltage V_b the electron current approaches I_{es} because no more electrons can be collected by the probe than the plasma can provide (see figure 3.1). We call this region the **electron–saturation** regime.

On the other side if one decreases V below V_p more and more electrons will be repelled from the probe. This decrease of the electron current is characterised by a Boltzmann factor:

$$I_e = I_{es} \exp\left(\frac{e(V - V_p)}{T_e}\right) \tag{3.5}$$

This exponential decay marks the **transition** region as shown on the figure. Actually the ion current has a similar behaviour when V is above V_p but due to the smallness of I_{is} the ion current I_i almost drops directly to zero for voltages just above V_p.

At a certain voltage the magnitude of the ion current and the electron current will have the same size. Hence the total current will be zero. The corresponding voltage with this zero–current case is called the floating potential V_f. This voltage is negative with respect to the plasma potential. This can be explained by noticing that the floating potential is the same potential we would obtain when the probe is electrically insulated from the vessel. This will cause the probe to rapidely charge up negatively due to the dominant electron current untill the charge becomes so negatively that electrons are repelled again. Eventualy the total collected current will be zero:

$$I = I_e + I_i = 0 \qquad \text{for } V = V_f \tag{3.6}$$

This condition can be translated into the following equality by taking $I_i = I_{is}$ and a Boltzmann factor for I_e ($V = V_f < V_p$):

$$I_i = I_{is} = -I_e = -I_{es} \exp\left(\frac{e(V_f - V_p)}{T_e}\right) \tag{3.7}$$

This equation can be rewritten by taken the natural logarithm and rearranging the result:

$$V_p = V_f + T_e \ln(\delta) \tag{3.8}$$

with

$$\delta = \frac{I_{es}}{I_{is}} \tag{3.9}$$

and T_e expressed in units of eV.

Equation (3.8) gives us a relation between V_p, V_f and T_e.

A further decrease of the voltage below the floating potential will result in the collection of mostly ions. As in the case of electron saturation the ion current will also saturate from a certain voltage V_a because no more ions can be collected than there are present in the plasma (see figure 3.1). We call this region the **ion–saturation** regime.

To summarise (see also figure 3.1):

- $V < V_a \Rightarrow$ ion–saturation
- $V_a < V < V_b \Rightarrow$ transition
- $V_b < V \Rightarrow$ electron–saturation

An important remark has to be made. In practice probes will only operate at voltages below or just slightly above the floating potential. Measuring at higher voltages would destroy

the probe due to the high electron currents. In the forgoing we discussed the $I-V$ curve in the ideal situation for a Maxwellian plasma which is in thermal equilibrium, collisionless and non–magnetised. Clearly the relaxation of these conditions will change the $I-V$ curve. The consequence will be discussed in the following sections.

3.2.2 Debeye shielding

Important to know is what the influence is of a test particle (in our case this will be the probe) into the plasma. The plasma will act as a shielding around this perturbation. The range of how far the perturbation effects the plasma and hence alters the plasma potential is determined by the Debeye shielding length λ_D. A short derivation is given here [25]. We assume that we have a positive point charge with charge e which serves as a test charge. This test charge introduces an electrostatic Coulomb potential in free space:

$$V_C = \frac{e}{4\pi\epsilon_0 r} \tag{3.10}$$

In a plasma this perturbation will effect the surrounding charged particles. In this case electrons will be attracted and positive ions will be repelled. Eventually this will shield the test charge from the rest of the plasma. An electron cloud will surround the test charge. The edge of this cloud determines λ_D. At this edge the electrons are no longer bound to the test charge. Their thermal energy (i.e. the thermal velocity w) is sufficient to overcome the Coulomb potential. A particle (electron/ion) will have a total energy E_{tot} of:

$$E_{tot} = \frac{m_{e,i}w^2}{2} \pm eV$$

where the upper sign holds for ion and the lower sign for electrons. The distribution function $f(\vec{r},\vec{w})$ will be:

$$f(\vec{r},\vec{w}) = n_0 \left(\frac{m_{e,i}}{2\pi T}\exp\left(-\frac{E_{tot}}{T}\right)\right)^{3/2}$$

where n_0 is the density when $V=0$, i.e. no perturbation. If we integrated this last equation over the entire momentum space we get the density:

$$n_{e,i} = \int f(\vec{r},\vec{w})\ \mathrm{d}^3w = n_0 \exp\frac{\mp eV}{T} \tag{3.11}$$

again the upper sign holds for ions and the lower sign for electrons. In this calculation we assumed for simplicity that $T_e = T_i = T$ and that there are no temperature gradients. We now use Poisson's equation to calculate V (whereby the test charge is included):

$$\epsilon_0\nabla^2 V = -e(n_i - n_e) + e\delta(\vec{r}) \tag{3.12}$$

Inserting equation (3.11) into (3.12) gives:

$$\nabla^2 V = \frac{2n_0 e}{\epsilon_0}\sinh\frac{eV}{T} - \frac{e}{\epsilon_0}\delta(\vec{r}) \tag{3.13}$$

This last equation is difficult to solve. Therefore we assume that the pertubation is small compared to the thermal energy, i.e. $eV << T$. Hence equation (3.13) becomes ($\vec{r}\neq\vec{0}$):

$$\nabla^2 V = \frac{2}{\lambda_D^2}V \tag{3.14}$$

where we introduced:

$$\lambda_D = \sqrt{\frac{\epsilon_0 T}{n_0 e^2}} \tag{3.15}$$

Remark: for $T_e \neq T_i$ one needs to replace in equation (3.15) T by $\frac{T_e T_i}{T_e + T_i}$ [24].
We assume spherical symmetry (only dependence on distance r) and hence equation (3.14) becomes:

$$\frac{1}{r^2}\frac{d}{dr}\left(r^2 \frac{dV}{dr}\right) = \frac{2}{\lambda^2} V \tag{3.16}$$

To solve this equation we make the following substitution:

$$V(r) = V_C(r) y(r)$$

where $y(0) = 1$ because we know that close to the test charge V should be the same as the electrostatic Coulomb potential V_C (equation (3.10)). Making this substitution into equation (3.10) gives:

$$\frac{d^2 y}{dr^2} = \frac{2}{\lambda^2} y \tag{3.17}$$

Solving this equation with the physical boundary condition that the solution is finite for $r \to \infty$ finally gives for V:

$$V(r) = \frac{e}{4\pi\epsilon_0 r} \exp\left(-\sqrt{2}\frac{r}{\lambda_D}\right) \tag{3.18}$$

This clearly demonstrates the physical meaning of the Debeye shielding lenght. It represents the range of the effect of the test charge into the plasma. For distances a couple of times λ_D the pertubation is negligible. Although some assumption has to be made, the general treatment of the Debeye shielding length gives a similar result. So to conclude, typical dimensions a of plasma probes need to be several times greater than the Debeye shielding length in order to reduce the influence of the probe on the plasma.

3.2.3 Incorporating collisions

Collisions will generally reduce the current collected by the probe because particles will not fly freely to the probe but rather diffuse to it. A way to calculate the effect of collisions is to really treat the plasma as a diffusive medium. The result is that the particle fluxes are adjusted as [23]:

$$\phi_{e,i} = \frac{1}{4} n_0 v_{e,i} \frac{1}{1 + \frac{v_{e,i} a}{4D}} \tag{3.19}$$

where the diffusive coefficient D is assumed to be constant, the probe to be a perfectly spherical absorber with dimension a and there are no magnetic fields. This equation can be written with the definition of the mean free path $l = 3D/v_{e,i}$ as:

$$\phi_{e,i} = \frac{1}{4} n_0 v_{e,i} \frac{1}{1 + \frac{3a}{4l}} \tag{3.20}$$

Mind the difference between equation (3.20) and the definition of the flux in equation (3.1). This simple approach for collisions shows that the collected current in the collisional case is reduced compared to the collisionless case. Equation (3.20) also gives a criterium to decide when collisions are negligible for a spherical probe. If $l >> a$, collisions can be ignored and currents are given by the equations listed in ideal case 3.2.1. Otherwise collisions needs to be taken into account and a reduction of the current is observed as given by (3.20). However for this thesis work, measurements were done in the SOL (see section 2.1.2). In this region the plasma density is relatively low, such that collisions can be neglected.

3.2.4 Influence of magnetic fields

In the ideal case of Langmuir probes the interpretation of the characteristics is relatively simple. The ion current is neglected except in the ion–saturation regime. But in the case of plasmas in strong magnetic fields like in tokamaks the interpretation becomes more complicated. When a magnetic field is present inside the plasma the charged particles will move in helical orbits around the magnetic field lines. The helical orbit is characterised by the Larmor radius which is bigger for ions than for electrons in the same magnetic field (see equation (2.3)). The consequence is that the real collecting surface of the probe for the ions will be larger compared to that of the electrons. So more ions will be collected compared to the zero–field case which means that equation (3.4) won't be valid anymore. The ion saturation current will be a factor $\sqrt{\frac{A_i}{A_e}}$ bigger than in the non–magnetic case. Hence the ion current will become more important with respect to the electron current. Furthermore the interpretation of Langmuir probe measurements in strong magnetic plasma is still not fully understood. Especially, there are no satisfying theories for the the $I-V$–characteristics far above the floating potential, i.e. the part were electron contribution to the current starts to dominate. Studies shows that for probe voltages above the floating potential the measured electron distribution (i.e. current) is no longer Maxwellian. To extract T_e, V_f and I_{is} one fits to the data a curve based on a Maxwellian electron distribution. Hence fitting the data far above the floating potential would introduce the incorrect non–Mawxellian electron distribution with a spuriously high T_e as a consequence [26]. Therefore one use the following formula to describe the observed $I-V$–characteristic below the floating potential:

$$\begin{aligned} I &= I_e + I_s && (3.21)\\ &= I_{es}\exp\left(\frac{e(V_f - V_p)}{T_e}\right) + I_{is} && (3.22)\\ &= I_{is}\left[1 - \exp\left(\frac{e(V - V_f)}{T_e}\right)\right] && (3.23) \end{aligned}$$

where we used in the third line equation (3.7) to eliminate I_{es}.

Equation (3.23) is a very important relation and will be used as a fitting function during the analysis of the data. Remember that this function can only be used up to the floating potential.

3.2.5 Ion saturation current and plasma density

Experimentally one can determine the ion–saturation current from the measured $I-V$–characteristics. Now one can use the fact that current is proportional to density and velocity:

$$\begin{aligned} I_{is} &= Aj_{is}\\ &= AZen_ic_s\\ &= Aen_ec_s \end{aligned} \qquad (3.24)$$

In the last line we used the fact that the entire plasma is charge–neutral, i.e. $Zen_i = en_e$. Where Z is the ion charge. Furhermore we introduced c_s which has the dimension of velocity. It is nothing else than the ion sound speed. This sound speed is given by the Bohm sheath criterion:

$$c_s = \sqrt{\frac{T_e + Z\gamma T_i}{m_i}} \qquad (3.25)$$

where γ the adiabatic coefficient of the ions. A note can be made on the values for γ and T_i. First of all γ depends on the model one assumes. For isothermal plasma flows one uses $\gamma = 1$, for adiabatic flows with isotropic pressure $\gamma = 5/3$ and for one–dimensional adiabatic flows $\gamma = 3$ [27]. The value of the ion temperature depends on the plasma. For plasma where

$T_i << T_e$ one often neglects the ion temperature. But in fusion plasmas the ions are often in thermal equilibrium. Even if the ion temperature is still smaller than the electron temperature one mostly take $T_i = T_e$.

The origin for this Bohm sheath criterion comes from the mechanism of plasma–sheath formation (e.g. [27, 28, 29]). In general a plasma is in connection with the outside world with means of boundaries (i.e. walls, probes, ...). Due to the high electron mobility the original neutral boundaries will charge up negatively and start to repell electrons and attract ions. Hence a positive space charge will build up in front of the boundary and act as a shielding of the pertubation of the negative boundary. A characteristic distance scale for shielding effects is the Debeye length λ_D (see section 3.2.2). This space charge region will typically extend over some Debeye lengths and is called the plasma sheath region. The complete mechanism of plasma–sheath formation is still not fully understood but a necessary condition for the sheath formation is the Bohm–criterion. This condition states that the ion speed needs to be at least the ion sound speed [27].

In the case of the probe measurements the ion–saturation is measured when the probes are biased to negative voltages. In this aspect the negatively biased probes acts as the boundary which is preceeded by a plasma sheath for which ions need to fulfill the Bohm criterion. Hence it is justified to use equation (3.24) as a relation between ion–saturation current and plasma density.

Chapter 4

The Ball–Pen probe

4.1 History

In 1967 I. Katsumata et al. developed a new kind of probe to measure the perpendicular ion energy distribution in plasmas. Therefore the electrons needed to be shielded completely [30]. This concept was improved by making the electron screening adjustable. As will be explained in section 4.2 the right choice of electron shielding made it possible to directly measure the plasma potential. This improved Katsumata probe was called the Ball–Pen Probe (BPP). One of the inventors of the BPP and pioneer in the measurements with this new probe is J. Adámek (also a supervisor of this thesis work) [31].

4.2 Physics

In figure 4.1 one can find the typical scheme of a BPP. A BPP exist of a pin that can move in and outside a tube. If the pin is completely outside the tube the BPP collects directly electrons and ions. Actually, in this case, the BPP acts as a convential Langmuir probe and hence the results derived in section 3.2 can be used. Things become different when the pin enters the tube. Because the BPP is oriented perpendicular to the magnetic field lines the pin will not intersect these field lines anymore if it is inside the tube. The pin becomes shielded from the plasma and charged particles can only be collected indirectly. As explained in section 2.1, charged particles orbit the magnetic field lines with a certain radius, the Larmor radius. This spiralling effect around the magnetic field lines will enable particles to enter the tube and hit the pin. Now we know from equation (2.3) that ions have a larger Larmor radius than electrons due to their larger mass. Intuitively one can expect that ions will penetrate more easy the tube than electrons due to this larger ion Larmor radius. As a consequence one also expect differences in the measured ion and electron current.

We now come back to equation (3.8). This equation gives a relation between the plasma potential V_p, V_f and T_e. One can simply measure V_f by keeping the probe floating. But mostly one is more interested in the plasma potential V_p because it is related to the electrical fields inside the plasma. These electrical fields and fluctuations on these fields are very important in the study of plasma turbulences and plasma confinement. By using equation (3.8) one can in principle determine V_p from V_f if one also know the values T_e and δ either from theory or from experiment. In practice T_e can be measured but it is not convenient to examine plasma potential fluctuations based on the combined effect of floating potential and electron temperature fluctuations. Above one still has the factor δ which is the ratio of electron–saturation current and ion–saturation current. Again ion–saturation current can be measured rather simply (see 6.2). The problem is the measurement of the electron–saturation current. As already mentioned the high power load of electron–saturation current can destroy the probe and hence this measurement is avoided. Mostly δ is estimated from classical Langmuir probe theory for non–magnetised

plasmas because of the lack of satisfying theories for electron–saturation regime in magnetised plasmas. For non–magnetised hydrogen plasmas (as in the case of this thesis) this value is about 2.8. A work around to this problem of determining V_p from V_f, T_e and δ is to adjust δ such that the problematic term $T_e \ln(\delta)$ becomes negligible.

The main goal of the BPP is to change δ, i.e. the ratio of the electron–saturation current to the ion–saturation current. As already mentioned the particle collection of the BPP will depend on the depth of the pin inside the tube and the Larmor radius of the considered particles. If the pin enters the tube one expects that electrons will enter the tube more difficult than the ions due to the their smaller Larmor radius. At a certain point the electron current should be counterbalanced by the ion current such that $\delta = 1$ and hence by equation (3.8): $V_p = V_f$. This behaviour has been experimentally observed [31]. It was seen that δ decreased almost close to one when the pin entered more and more the tube. However one observed that from a certain depth δ became independent from the depth and stayed around 1. This behaviour is very convenient for experimental set–ups because it seems not very important how deep the pin is inside once the minimum depth is crossed. Finally it should be noted that from this experiment it was also seen that δ stayed above 1 ($\delta \approx 1.1$). This means that the electron–saturation current was always higher than the ion–saturation current eventhough the pin was far inside the tube. A possible explanation for this feature is the transport of electrons across the magnetic field lines. Still a lot of work needs to be done around these topics. Nevertheless comparable studies of BPPs with other probe systems that can directly measure plasma potential showed that the results of the BPPs are credible [32].

To conclude one can use a BPP as a tool for the direct measurement of the plasma potential. To this end the probe's pin needs to be sufficient deep inside the shielding tube such that the measurement of floating potential directly corresponds to the plasma potential. Note that BPPs can only be used in magnetic plasmas because the working principle is strongly based on the magnetic–related Larmor radius.

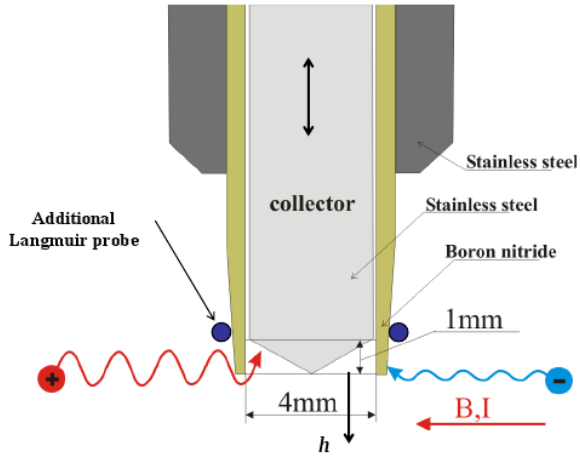

Figure 4.1: Example of a schematical view of a Ball–Pen probe. The probe is oriented perpendicular to the magnetic field lines. This BBP was used for the first time on the CASTOR tokamak [31].

Part III

Experiments with Electrical Probes

Chapter 5

Experimental set up

5.1 Divertor probe array

The divertor of COMPASS is equiped with an array of 39 Langmuir probes as is shown in figure 5.1. The Langmuir probes are seperated by a distance of 5 mm as can be seen in figure 5.2

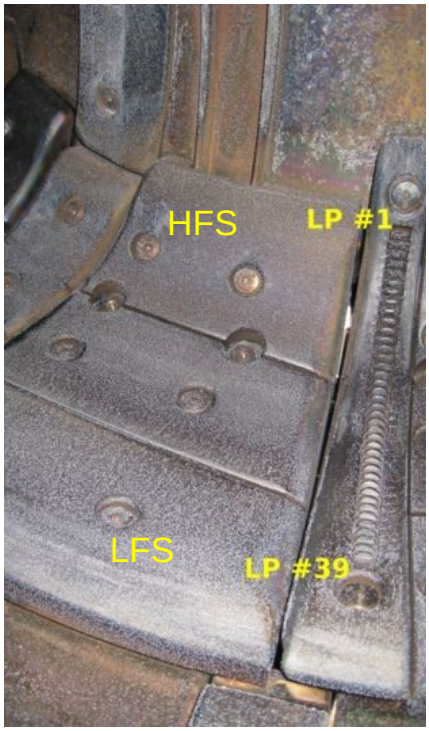

Figure 5.1: Image of the array of 39 Langmuir probes in the divertor of COMPASS. Langmuir probe #1 is located in the high field side (HFS) and #39 in the low field side (LFS) of the magnetic field.

Maximum five Langmuir probes can be connected to a power supply. It can either apply a sweeping voltage or a constant voltage. In the latter case one usually takes a voltage of about $-100\,\mathrm{V}$ to measure ion–saturation current I_{is}. If a sweeping voltage is applied it is possible to determine the $I-V$–characteristics as explained in section 3.2.1. Typically the sweeping voltage is between $-100\,\mathrm{V}$ and $+100\,\mathrm{V}$. The maximum voltage may certainly not be larger than $+100\,\mathrm{V}$. A higher voltage would collect to many high energy electrons which could destroy the probe. Finally one can also disconnect the power supply from the probe. The probe is thus in floating mode and one can measure the floating potential. To summarise, the divertor probe provides a

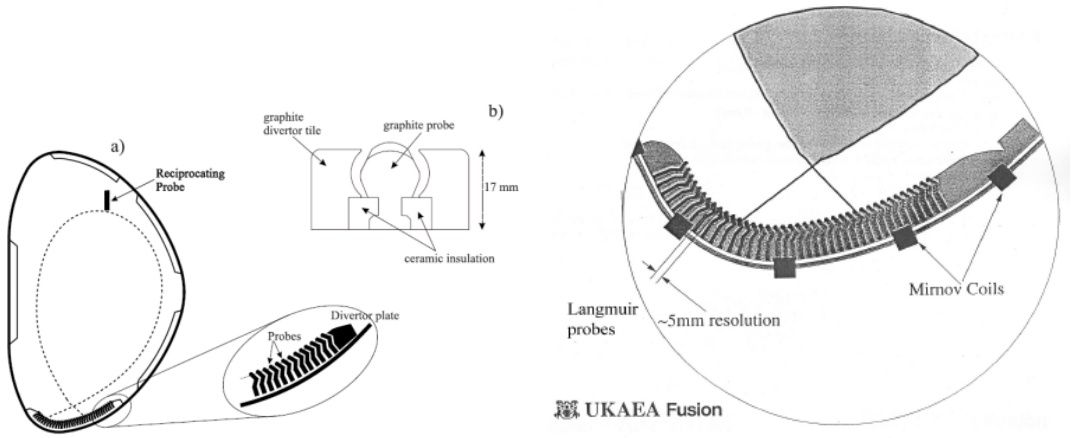

(a) a) Poloidal cross–section of COMPASS with the positions of divertor probes. b) Detail of a Langmuir probe of the divertor array.

(b) 5 mm distance between two probes.

Figure 5.2: The divertor probe on COMPASS.

way to record floating potential, ion–saturation current and $I - V$–characteristics. In figure 5.3 a basic electronical scheme is given for the measurement of voltage and/or current in the case of two probes connected. Currents are measured over the 4.7 Ω–resistor. To measure voltages a simple potential divider is used with a resistor ratio of 100.

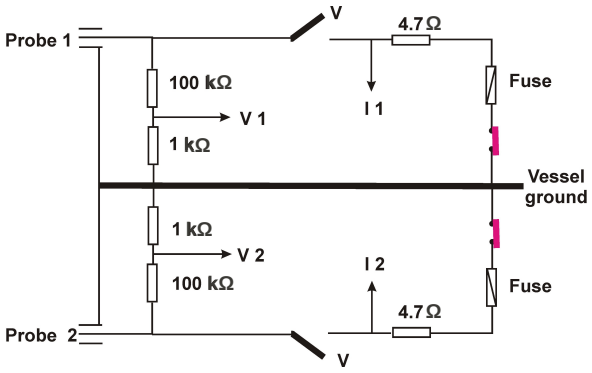

Figure 5.3: Basic electronical scheme for measuring voltage and/or current from the divertor probes.

5.2 Reciprocating manipulator

The reciprocating manipulator with probe head is one of the different kinds of probe systems, frequently used in fusion plasmas. This reciprocating manipulator penetrates and leaves again the plasma at very high frequencies. Hence the probe head is capable to withstand the higher heat loads present deeper inside the plasma without being destroyed. Reciprocating manipulators are thus suitable to examine plasma properties further inside the plasma. The probe head, used before on ASDEX Upgrade (see e.g. [33]), of the reciprocating manipulator on COMPASS consists of four Langmuir probes and four Ball–Pen probes (see figure 5.4a).

In figure 5.5 one can find the basic electronical scheme for measurements with the probe head of the reciprocating manipulator. The power supply can either provide a sweeping voltage or a constant voltage to the probes of the probe head. The sweeping voltage is used to measure

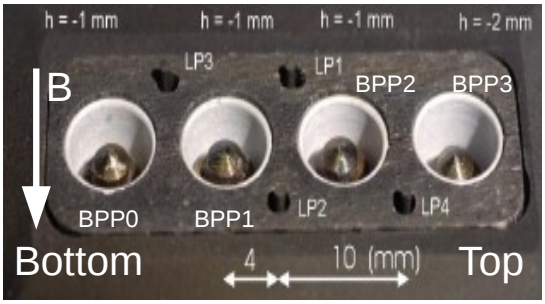

(a) Detail of the probe head. Four Langmuir probes (LP) and four Ball-Pen probes (BPP) are present. Three BPPs are 1 mm inside their tube and one BPP is 2 mm inside. The probe head shielding is made of graphite. The probe head is oriented perpendicular to the magnetic field as shown in the figure.

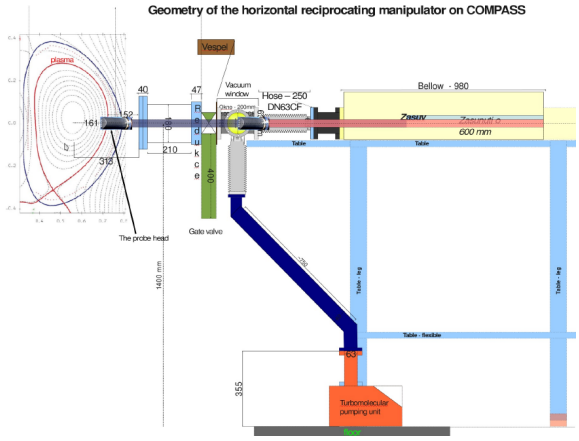

(b) Set up of the reciprocating manipulator. The probe head is located in the midplane.

Figure 5.4: The reciprocating manipulator on COMPASS tokamak.

$I - V$–characteristics. This operation mode is called sweeping mode and can be obtained by closing the switch an applying a triangular voltage to the probe. The voltage drop across the resistors R_1 and R_2 gives us the value of the voltage and the voltage drop across resistor R_3 gives us the current collected by the probe. Instead of applying a sweeping voltage one can also apply a constant voltage. This voltage is chosen negatively such that only ions are collected (positive voltage would collect the much higher energy electrons which could destroy the probe). Hence one now measures with the same circuit the so–called ion saturation current or short I_{sat}. A last possibility is to not close the switch. Hence the probe is not biased and will become floating. The voltage drop measured across R_1 and R_2 will now give directly the floating potential. This last operation mode will be used during the experiments with the reciprocating manipulator (see chapter 7).

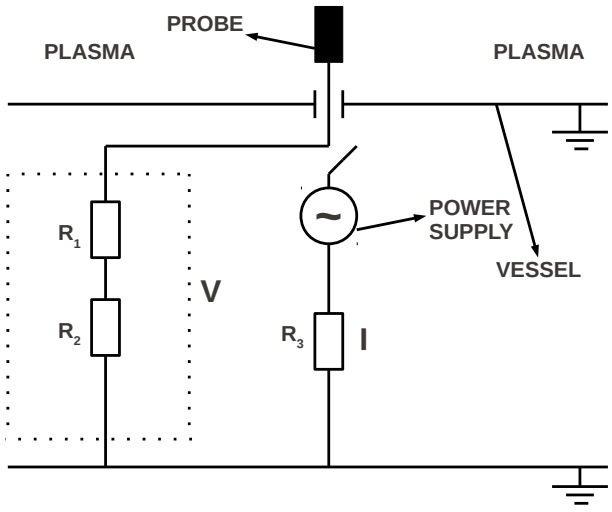

Figure 5.5: Basic electronical scheme for BPP measurements with R_1=660 kΩ, R_2=6.7 kΩ and R_3=47 Ω.

A remark can be made concerning the reciprocating manipulator. During my campaign in Prague the reciprocating manipulator was installed and used on COMPASS for the first time ever. Hence the data analysed in this thesis work are the first results on COMPASS with the reciprocating manipulator! Unfortunately the probe system was not fully operationally in this starting–up period. It was not possible to put the probe head reciprocating automatically. Instead a predefined penetration depth was determined before each plasma discharge. Therefore the reciprocating manipulator stayed in a static position with respect to the vessel. However there was still some way of reciprocation by means of the movement of the plasma column. As explained in the following section there was no plasma position feedback system. Hence the plasma column was allowed to move with respect to the vessel and thus possibly reciprocate with respect to the probe head.

5.3 Plasma positioning system

In this section we want to make an important remark concerning the plasma positioning system on COMPASS. Normally there should be a feed back system which adjusts the position of the plasma column (measured with techniques as explained in 2.2.3). The main of goal of this system is to keep the plasma as long as possible in an equilibrium position inside the torus vessel. Unfortunately the feed back system was not operationally during the campaign. As a consequence the plasma column was not stable. Hence most of the shots made during the campaign were of short duration ($< 50\,\text{ms}$). Nevertheless the COMPASS–team succeeded in having a few shots longer than 100 ms till even a temporary record shot of about 200 ms, which is a great accomplishment without properly working positioning feed back system.

Due to the position of the divertor probe (down in the tokamak at the divertor) and the static position of the reciprocating probe (at the edge of the plasma close to the wall) a signal was obtained only when the plasma moved to these probes. In chapters 6 and 7 one will see that most of the time useful data are obtained at the beginning of the shot when the plasma is not yet stabilised or at the end of the shot when the plasma disrupts at the probes's location.

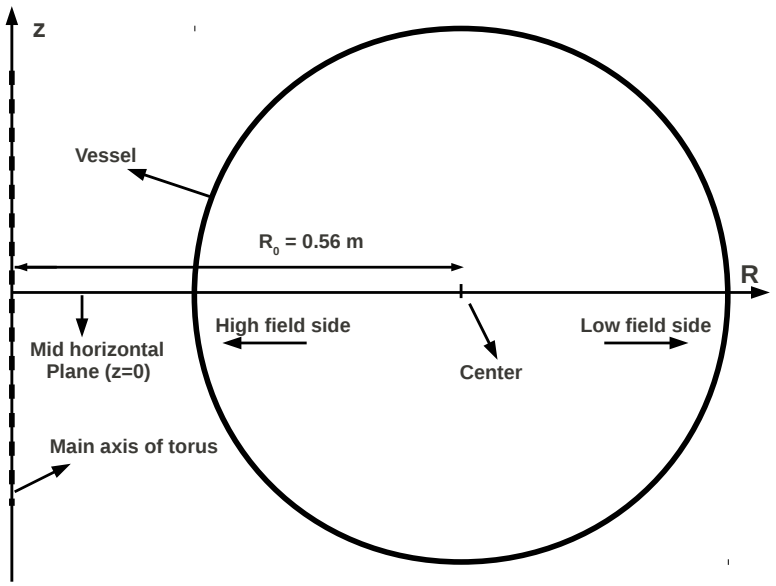

Figure 5.6: Definition of the coordinates z and R. The zero of the z coordinate is the mid horizontal plane whereas the zero for R corresponds with the main axis of the torus. R_0 is the major and a the minor radius of the tokamak (see also table 2.1).

Plasma position

Sometimes it necessary to know the position of the plasma column. This information is extracted from magnetic reconstruction (see also section 2.2.3). A routine exists that immediately gives the z and R coordinates as output. In figure 5.6 we define what these coordinates are. For further purpose it is worthwhile to mention that a positive z means that the plasma column is above the mid horizontal plane and vice versa. If R is greater than $R_0 = 0.56\,\mathrm{m}$ the plasma column is more located to the low field side and vice versa.

5.4 Data acquisition system

The probes measure eventually only voltage signals. These signals can represent either a current or a real voltage depending on the measuring circuit (see the electronical circuits in sections 5.1 and 5.2). The voltage signals are digitalised and sent to a central **Data Acquisition System (DAS)**. From there on the data can be accessed with data–analysing–software. Special routines in either IDL® or MATLAB® are available to read the data easily. For this thesis the high-level technical computing language MATLAB® was used.

For completeness we give an overview of the timing of DAS.

- 0 ms: start–up of the main power supplies
- 10 ms: start–up of the toroidal field power supplies
- 800 ms: start–up of the magnetising power supply
- $\sim$ 960 ms: plasma breakdown

All the data with the probes were acquired at a sampling frequency of 2 MHz.

Chapter 6

Measurements with the divertor probe array

6.1 Sweeping mode

A first experiment with the divertor probe array is dedicated to the measurement of $I - V$–characteristics. To this end a triangular voltage between $-100\,\mathrm{V}$ and $+30\,\mathrm{V}$ is swept at a frequency of $1 - 3\,\mathrm{kHz}$. One has chosen for a maximum voltage of $+30\,\mathrm{V}$ instead of $+100\,\mathrm{V}$ to reduce the electron–collection which could damage the probes.

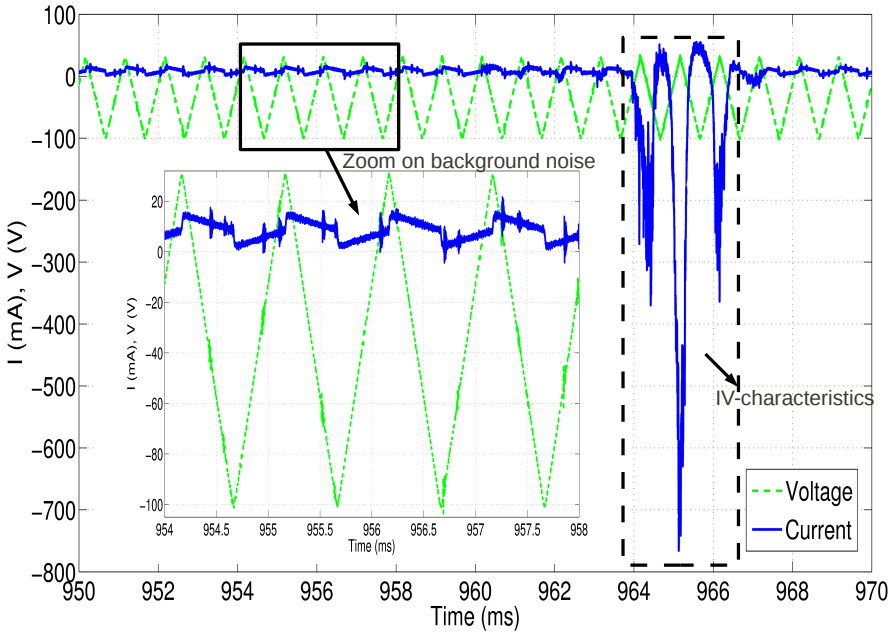

Figure 6.1: Illustration of the background noise present on the current signal (full blue line) for shot #1499 and LP #3. Notice that a ramping up of the voltage (dashed green line) corresponds to a ramping up of the noise and vice versa.

6.1.1 Background noise

In figure 6.1 one can see that there is a background noise present on the raw current signal. Hence the first task that one needs to do is to remove this unwanted noise as much as possible. The origin of this parasitic signal is related to the capacitance of the cables used for the data acquisition. The long cables (up to 30 m and more) used for the transfer of the signals from

the probes to the data aqcuisition system have an non–zero capacitance C_{cable}. Therefore, if a voltage $V(t)$ is running through these cables a capacitive current I_{cap} is induced, given by:

$$I_{\text{cap}} \propto C_{\text{cable}} \frac{\mathrm{d}V(t)}{\mathrm{d}t} \tag{6.1}$$

This parasitic signal becomes more apparent with increasing sweeping frequency as can be seen in figure 6.2. Hence one needs to find a compromise between a high sweeping frequency, in order to obtain as much as possible $I-V$–characteristics, and a low frequency to reduce the capacitive current. Therefore, as already mentioned, one usually sweeps the voltage at a frequency of $1-3\,\text{kHz}$.

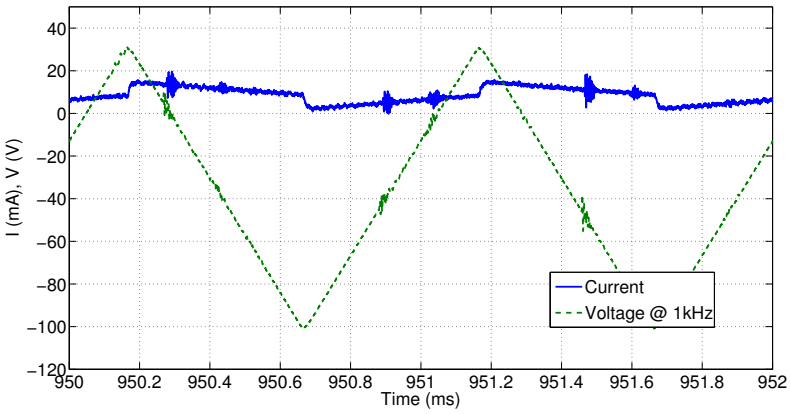

(a) Sweeping voltage at frequency of 1 kHz for shot #1499 LP #3.

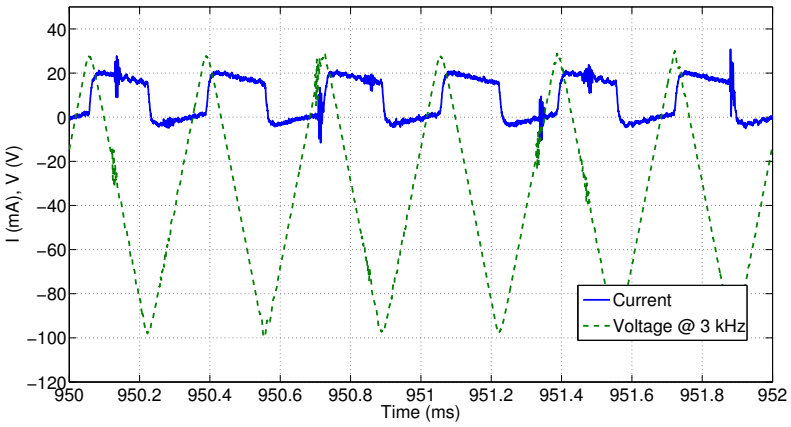

(b) Sweeping voltage at frequency of 3 kHz for shot #1484 LP #3.

Figure 6.2: Background noise on the current signals (blue full lines) due to capacitive effects for two shots at two different sweeping frequencies. The effect is more significant for higher sweeping frequencies. Mention that above this repetitive effect there is (mostly) an off set for the current signal.

As can be seen in figure 6.1, the capacitive current goes up as the voltage goes up and vice versa. In the analysis of the $I-V$–characteristics only one $I-V$–curve, corresponding to either one ramping up or one ramping down voltage, is selected at a time. Therefore one can make use of a rather simple technique to remove the noise. One starts with taking a time window before the actual discharge where only noise is present. Depending on the desired $I-V$–characteristic (corresponding with either a voltage ramp up or down) one must choose in this time window a current–noise corresponding with a similar voltage ramp (up or down). Next a linear fit is made

to this noise and substracted from the original signal (see also figure 6.4). Substracting this linear fit also ensures that the off set on the current signal is corrected, if present. The resulting corrected signal is now being used to accomplish the actual fitting procedures as explained in the following section.

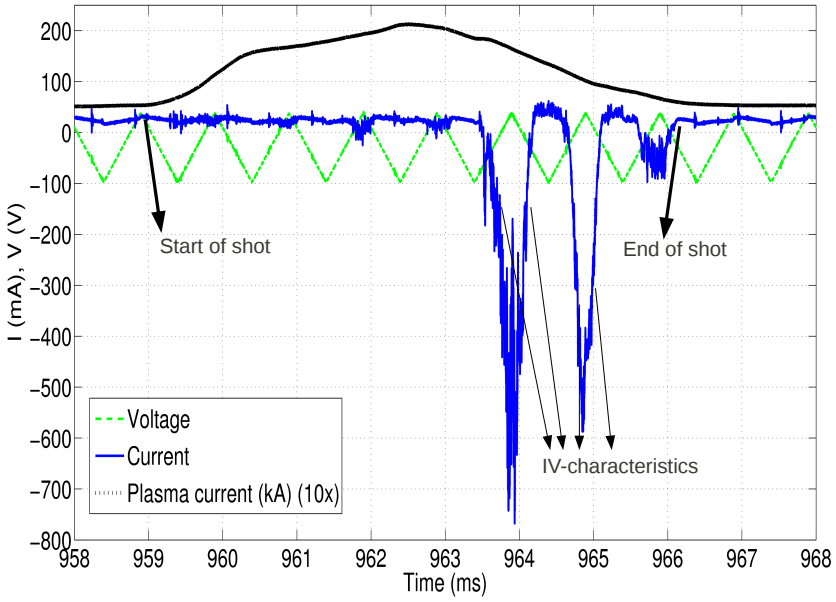

Figure 6.3: Raw current (full blue line) and voltage (dashed green line) signal (without correction for the noise) in function of time for shot #1498 and LP #5. The plasma current (black dotted line) is plotted as reference for the duration of the shot. It is multiplied by 10 and expressed in kA. Remark that one measures $I-V$–characteristics only at the end of the shot due to the fact that the plasma positioning system is not operational (see the text for a more profound explanation).

6.1.2 $I-V$–characteristics and fitting procedure

In figure 6.3 the raw signals for current and voltage are shown. For clarity the signal of the plasma current is included. The plasma current is an indication for the duration of the discharge. At the end of the shot one can see four clear $I-V$–characteristics. When the voltage ramps up positive, more and more electrons will be collected which drives the current negative. At the other hand, negative voltage will repell the electrons and only attract ions. A bias of $-100\,\mathrm{V}$ is sufficient to obtain the ion–saturation regime (see section 3.2.1). Notice that no electron–saturation is obtained because the high power load could severely damage the probe.

After removing the background noise (see section 6.1.1) equation (3.23) is fitted to the $I-V$–characteristics. To this end a procedure was programmed which make it possible to select one single $I-V$–characteristic at a time. As a result it gives the desired quantities: I_{sat}, T_e and V_f and χ^2 as indication of the goodness of fit. The fitting procedure is summarised from figures 6.4 till 6.6 for shot #1498 and Langmuir probe #3. A remark can be made about the range of fitting the $I-V$–curves. As already mentioned in section 3.2.4 the use of equation (3.23) is only valid up to the floating potential. Nevertheless we will fit this function to the $I-V$–characteristic also just above the floating potential. To illustrate the fitting region we look at shot #1498 and Langmuir probe #3 for which is found that $V_f = -29.9\,\mathrm{V}$ and where the curve was fitted till about $-17\,\mathrm{V}$ which is just above V_f (see figure 6.6).

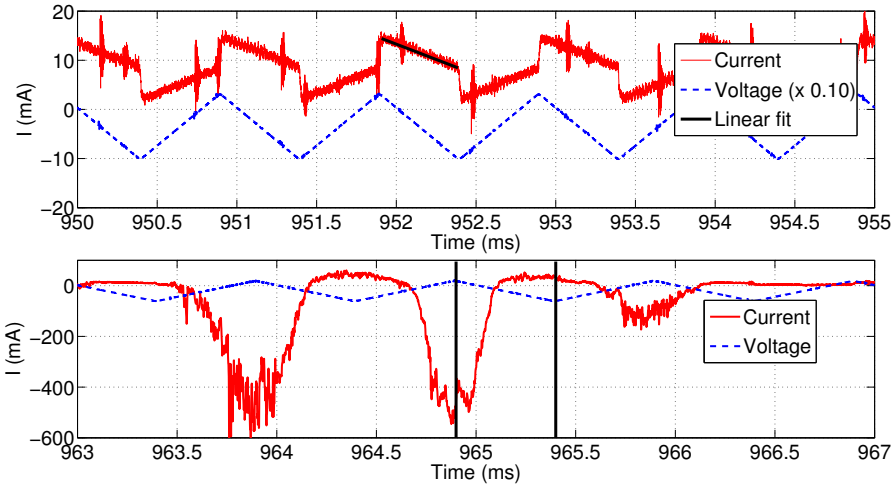

Figure 6.4: In the top panel voltage (dashed blue line) and current (ful red line) are plotted for a time window before the actual shot (shot #1498 LP #3). In the bottom panel the current and voltage are plotted in the time window during the discharge. The two black vertical lines indicate the $I-V$–characteristic that was selected. It corresponded with a ramping down voltage and hence a similar ramp was selected at the top panel (thick black line).

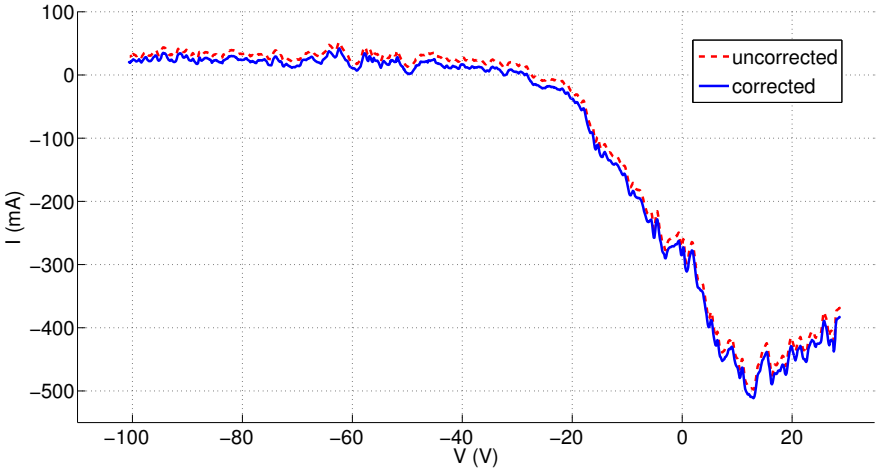

Figure 6.5: The raw current signal for shot #1498 LP #3 is plotted with a dashed red line. The ful blue line is the same current after substracting the background noise determined with the linear fit from figure 6.4.

6.1.3 Results and discussion

The fitting procedures explained in the two previous sections are used to analyse the data obtained with the divertor probes. Mostly there are several, typically three till five, $I-V$–characteristics observable during one shot as the voltage is sweeping (see for example figure 6.3). A first set of data are concerned with the determination of the basic plasma parameters T_e, I_{sat} and V_f for a configuration whereby data were acquired with five neighbouring LPs at the high field side (from LP #3 till LP #7, each seperated by a distance of 5 mm, see figure 5.1). Unfortunately the signal from LP #7 is not good enough to ensure a decent fitting. Therefore only LPs #3 till #6 are considered.

For every fitted $I-V$–curve χ^2 was between 2 and 8. The fitted values for T_e, I_{sat} and V_f are plotted in function of time whereby the time is taken as the middle of the time window used for fitting. Hence for one shot and for one certain LP we can obtain a kind of evolution of

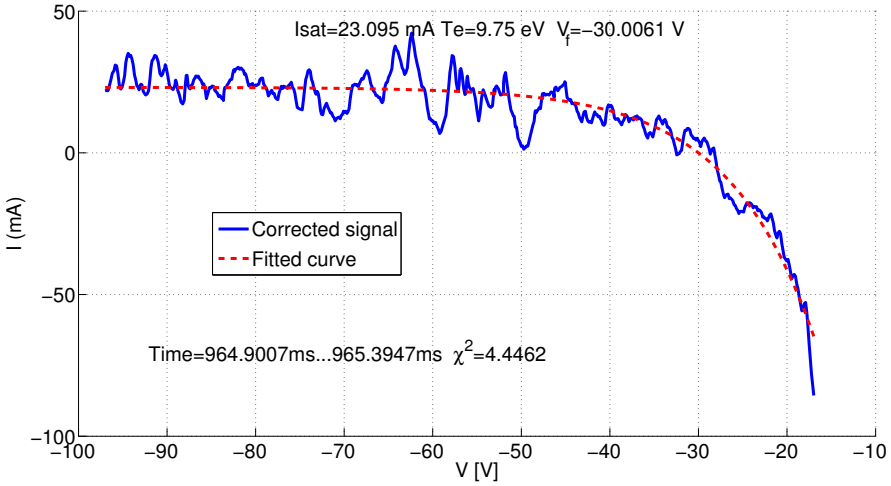

Figure 6.6: The final result of the fitting procedure for shot #1498 and LP #3. Ion–saturation current (I_{sat}), electron temperature (T_e) and floating potential (V_f) are given. Furthermore the goodness of fit is shown by means of χ^2 and also the time window from which the $I-V$–characteristic is selected.

these important plasma parameters. Remark that the time resolution is rather limited by the sweeping frequency (this in contrast with BPP measurements which will be explained in chapter 7). There are two $I-V$–characteristics per sweeping period (time window corresponding with one ramping up and one ramping down of the voltage). The fitted plasma parameters derived from one $I-V$ curve are then actually an average over half of this sweeping period.

From figures 6.7 till 6.9 one can find the results obtained for shot #1466 whereby the plasma parameters T_e, I_{sat} and V_f are plotted in function of time for LP #3 till LP #6. A first remark is that there are not many data for this shot (as for all analysed shots) which make a decent interpretation quite difficult. There are only a few data per shot due to the fact that the plasma positioning system was not operational during the experimental campaign as explained before. As a consequence the plasma shots are quite short and most data on the divertor probes are collected at the beginnig or the end of a shot, when the plasma column is unstable. Therefore only a small number of $I-V$–characteristics are recorded by each LP. Nevertheless some information can be extracted from the obtained data.

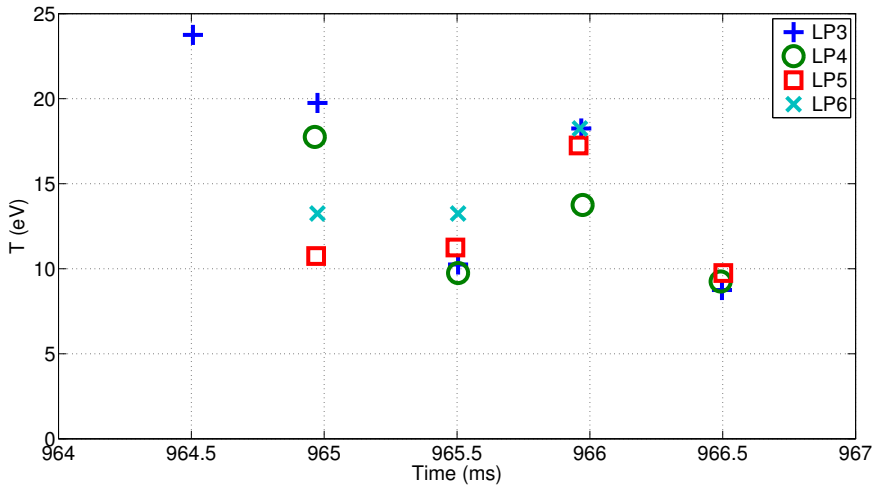

Figure 6.7: Time evolution of the electron temperature for shot #1466 and for four LPs (#3–6)

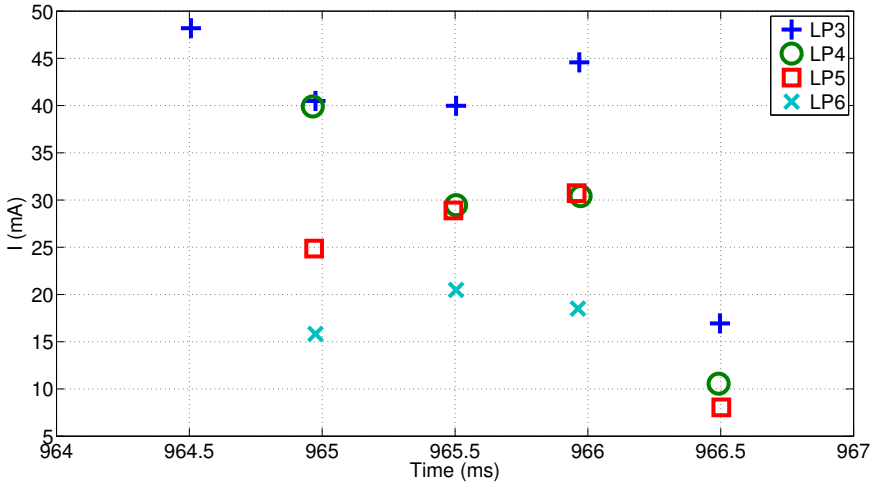

Figure 6.8: Time evolution of the ion saturation current for shot #1466 and for four LPs (#3–6)

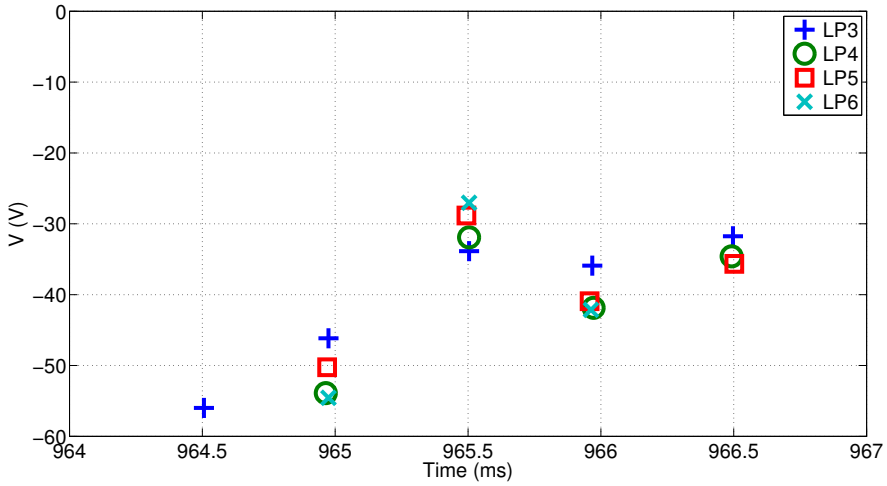

Figure 6.9: Time evolution of the floating potential for shot #1466 and for four LPs (#3–6)

For shot #1466 one can see that the trend (rising or declining) of T_e is quite similar for all four LPs (figure 6.7). Furthermore one observes that the electron temperature in the plasma edge flucuates roughly between 9 eV and 20 eV with even a peak around 24 eV in the beginning of the measurement for LP #3.

For I_{sat} one can also see that the four LPs roughly show a similar behaviour. The measured ion–saturation currents are generally decreasing in function of time with roughly a factor of 3 (notice that for LP #6 no qualitatively good fitting was performed for time $t \approx 966.5$ ms). Remembering that the ion–saturation current is related to the plasma density (see 3.2.5) this could mean that the plasma column moved away from the divertor (i.e. less plasma density). This statement should be compared with the measurements of the plasma position (see also section 5.3). Unfortunately the magnetic reconstruction did not provide results for the plasma position up to the time region where the $I - V$ curves were fitted (see figure 6.10). The large fluctuations at the beginning and the end of the reconstruction of the plasma coordinates is not physical but rather a consequence of errors. Nevertheless we can assume that based on figure 6.10a the plasma column stayed on the high field side during the LP–measurements and even moved further to the high field side. Looking at the rising trend of the z position (figure 6.10b) at the end of the magnetic reconstruction it seems plausible that the plasma even moved further

above the mid plane (i.e. away from the divertor probes). Hence this could explain why the ion–saturation current decreases with time.

Finally the trend of V_f is somehow opposite to T_e. Roughly one can say that V_f is increasing when T_e is decreasing and vice versa.

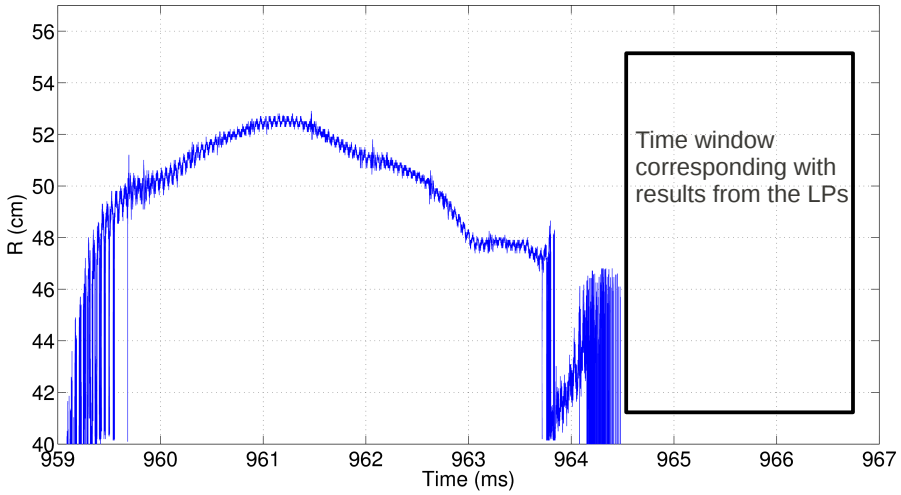

(a) R coordinate in function of time.

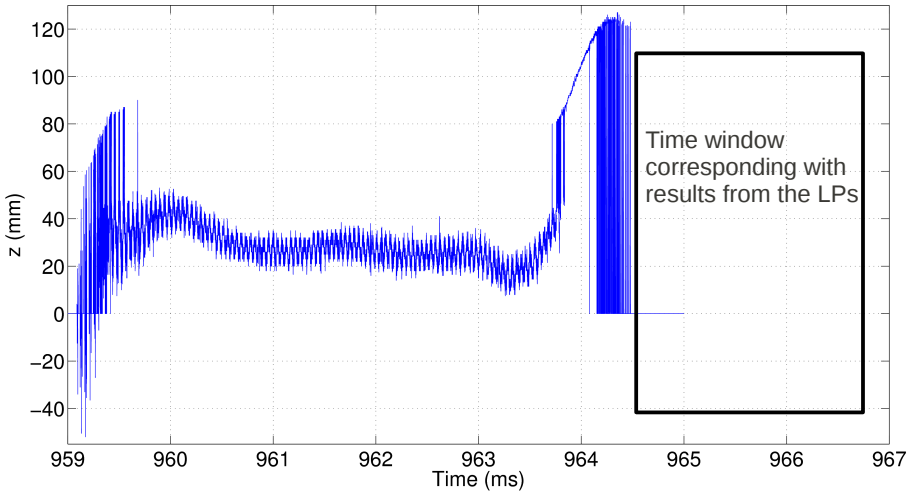

(b) z coordinate in function of time.

Figure 6.10: Plasma position for shot #1466. See section 5.3 for the definition of the plasma position coordinates. The time window which corresponds with the time interval of figures 6.7 till 6.9 is shown with the black rectangle. It is clear that for this time window no data for R or z is available.

In figure 6.11 we grouped for six different shots the results from for the electron temperature into two categories: all the electron temperatures determined with the four LPs during the ramping down of the voltage and during the ramping up of the voltage. It can be seen that the electron temperatures during a ramping up phase seems to be systematically higher than during a ramping down phase.

This experimental configuration with four neighbouring LPs at the high field side was used during the shots #1457–1512 from which 30 shots actually produced plasma inside the tokamak. In total 9 shots (#1463, #1466–1468, #1484, #1486–1487 and #1498–1499) out of these actual plasma shots gave relatively good signals on the divertor probes. The rather low number of qualitatively good shots are again a consequence of the lack of a working plasma positioning system. Above the useful data were obtained during the beginning or the end of the shot. At

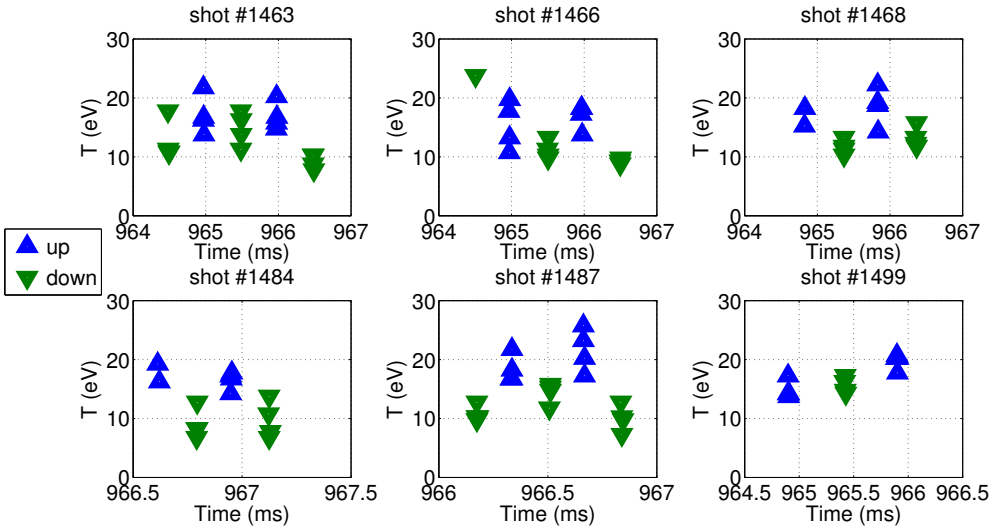

Figure 6.11: The blue upwards (respectively green downwards) pointing triangles represent T_e measured during a ramping up (respectively down) phase of the sweeping voltage. T_e is slightly higher during a ramping up phase of the sweeping voltage.

that moment the plasma was unstable and hence the magnetic reconstruction did not produce any position output. Therefore position data could not be compared decently with the results from the LPs for any of these shots. The electron temperature for these shots varied between 5 eV and 24 eV with ion–saturation currents between 4 mA and 50 mA and floating potentials between −63 V and −21 V.

6.2 Ion–saturation mode

The ion–saturation current can be measured by biasing the probes to negative voltages. For this experiment the voltage was set to a constant value around −100 V. As explained in section 3.2.5 the ion–saturation current is proportional to the plasma density ($I_{is} \propto n_e$). Hence we can consider fluctuations on the ion–saturation current as fluctuations on the plasma density.

6.2.1 Background noise

Mostly a clear off set is visible on the raw current signal. Above this off set one can observe sometimes an extra background noise. The origin of this background noise is caused by the voltage signal coming from the power supply. In figure 6.12 this is clearly demonstrated. One can see that the noise on the current signal is just the voltage current shifted in time and multiplied with some constant. Therefore a routine was written to find the shift in time t_{shift} and the multiplication factor A that minimalised the difference between current I and voltage signal V. Or in formula form: $I - A * V(t + t_{\text{shift}}) \approx 0$. In figure 6.13 one can see the current signal before and after removing the background noise.

6.2.2 Correlations between two Langmuir probes

As already mentioned ion–saturation current fluctuations can us learn something about plasma density fluctuations. In this experiment the aim is to examine possible poloidal plasma movement based on the correlation of I_{sat} between two neighbouring LPs. As a result the **poloidal**[1] plasma

[1]Notice that the poloidal velocity is estimated. The divertor probe array is namely oriented along the poloidal direction (see figure 5.2) and hence only phase correlation along the poloidal direction can be calculated.

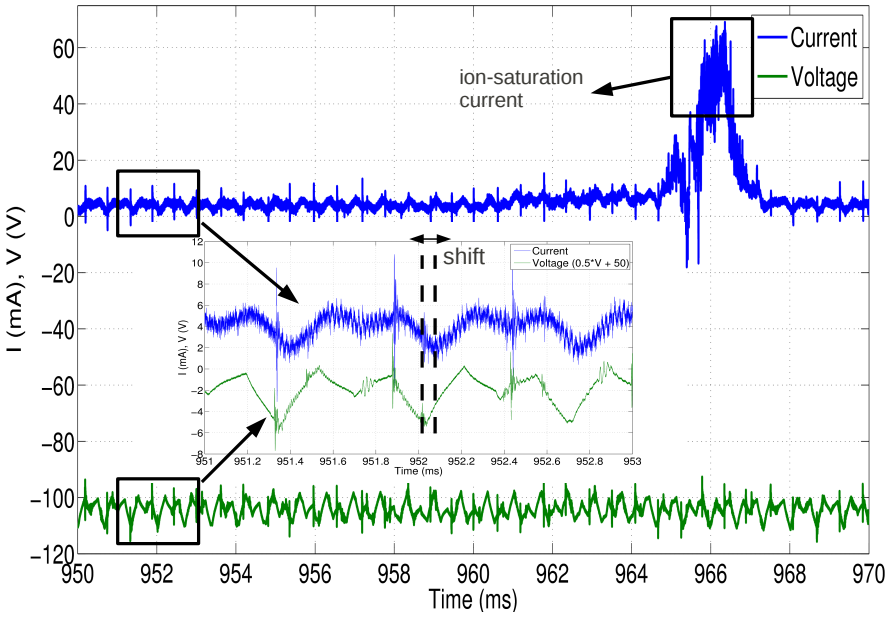

Figure 6.12: Above the off set one can sometimes observe a background on the current (blue line) which is related to the voltage signal (green line). In the subfigure the voltage is devided by 2 and shifted vertically by 50 V to clearly see the shift compared to the current signal. Shot #1518 LP #3.

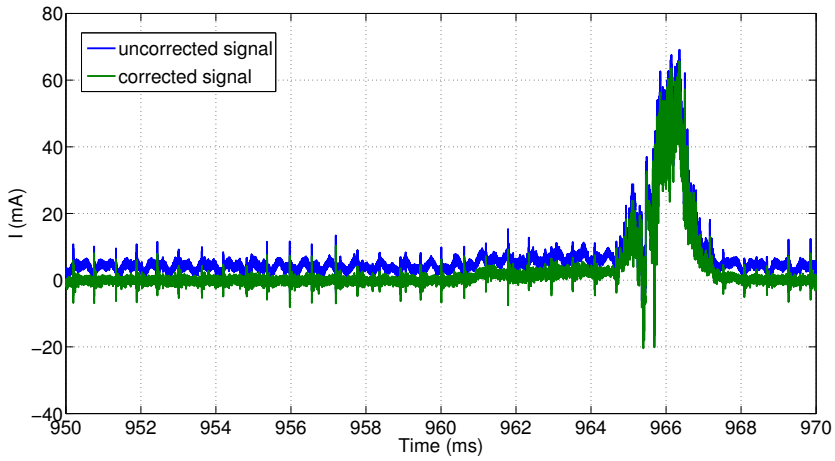

Figure 6.13: The ful green line represents the current signal after correcting for the off set and the background noise. Shot #1518 LP #3.

velocity v_{pol} can be estimated. This velocity is an important plasma parameter because it is an indication of plasma rotation in the poloidal direction. The presence of a poloidal plasma rotation can have a stabilising effect on the plasma and hence is important in stability studies.

The poloidal plasma velocity v_{pol} can be estimated by determining the time delay between the current signal of two adjacent LPs. Together with the kwowledge of the distance d=5 mm between these two LPs one can simply determine v_{pol} as:

$$v_{pol} = \frac{d}{\tau} \tag{6.2}$$

Main task to do is to determine the time delay τ. Two methods will be used for deriving τ [34].

A **first method** consist of directly determining the time lag (i.e. time delay) between the

two current signals by means of the cross–correlation function (see appendix B, section B.3) of these two signals.

The **second method** make use of the cross–power spectrum (CPS, see appendix B, section B.4). The phase ϕ of this CPS is plotted in function of the frequency f. This should give a linear relation given by equation (B.11) or in discrete form:

$$\tau = \frac{1}{2\pi}\frac{\Delta\phi}{\Delta f} \tag{6.3}$$

Finally both methods give a value for τ which leads to v_{pol} through equation (6.2). The time resolution of both methods is limited by the sampling frequency of 2 MHz and is thus 0.5 µs. These poloidal velocity estimations where determined for a few shots. It is worthwhile to mention that the determination of v_{pol} with both methods is based on the assumption that the time delay is only caused by a poloidal rotation of the plasma column. Any other physical processes are assumed to not contribute to the observed time delay.

6.2.3 Results and discussion

Both methods of determining τ and hence v_{pol} are demonstrated for shot #1521. In figure 6.14 an overview is given for the raw current signals on all five LPs (#3–7) for this shot when a constant voltage of −100 V is applied. For clarity also the plasma current is shown to indicate the beginning and the end of the plasma shot. One can see that the significant part of the signals is around the time region from 965 ms, beginning of a clear saturation region till, 967.5 ms, the end of the plasma shot. This time region is shown explicitely for LP #3 in figure 6.15. The saturation region still runs further above 967.5 ms but we exlude this region in the analysis because it is appearing in a region when the plasma decays and hence is unstable.

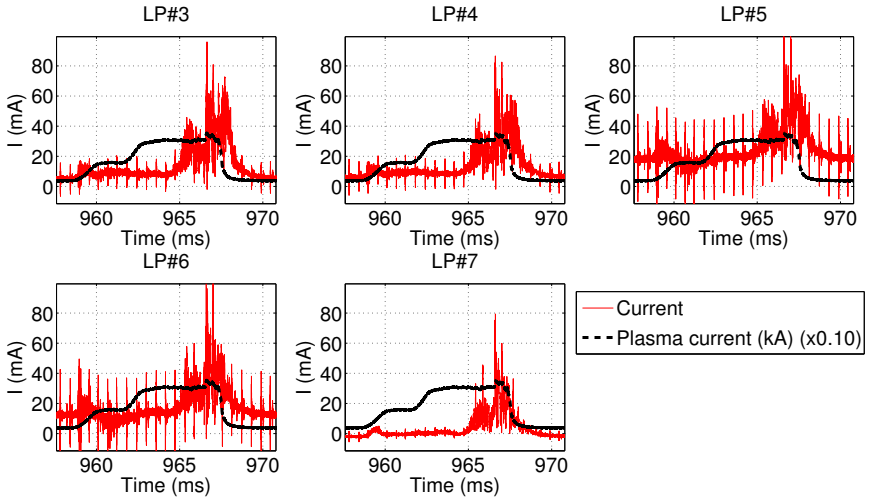

Figure 6.14: Overview of the raw current signals (red ful lines) on the five LPs (#3–7) for shot #1521. The applied voltage is −100 V. The plasma current (black dashed line, scaled by a factor 0.10 and expressed in kA) indicates the beginning and the end of the shot.

After correcting the signals for background noise as explained in section 6.2.1, the correlation between two adjacent LPs is examined.

Method 1: time lag measurement

In figure 6.16a one can find the (corrected) current signals for LP #3 and LP #4 in function of time whereby the mean value was removed. One can observe a kind of time delay between

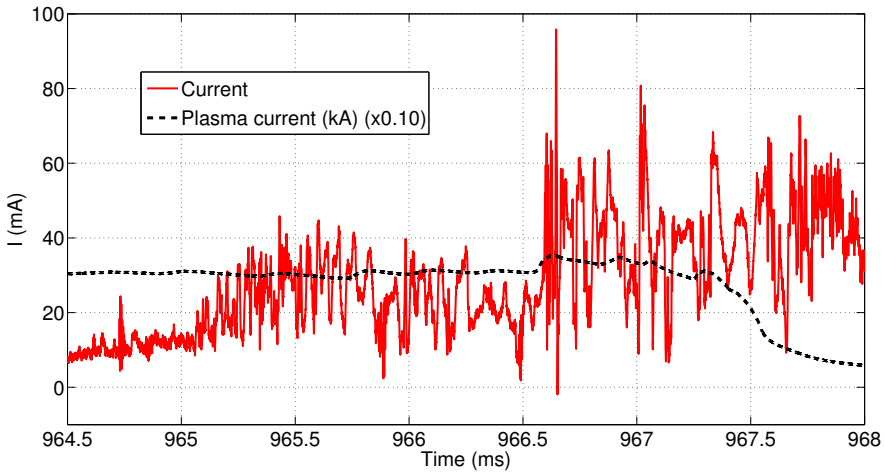

Figure 6.15: Zoom in on the raw current signal (red ful lines) for LP #3 for shot #1521. The applied voltage is −100 V. The saturation region runs from about 965 ms till 967.5 ms. The plasma current (black dashed line, scaled by a factor 0.10 and expressed in kA) is also shown.

both fluctuations signals. This time delay is characterised by the time lag which is determined from the cross–correlation function of these two neighbouring LPs. The "zero-time" is chosen as the time when the auto–correlation functions of both LPs is maximum. The time lag is the moment with respect to the zero–time when the cross–correlation function reaches its maximum. In figure 6.16b on can find a plot of the different correlations function for LP #3 and LP #4 for shot #1521. A time lag of about 8.5 µs is found. As the distance between two LPs is 5 mm, this time lag corresponds to a poloidal velociy of about $588\,\mathrm{m\,s^{-1}}$.

Method 2: CPS–phase measurement

Instead of reading directly the time lag from the cross–correlation as in method 1, the phase ϕ of the CPS is plotted in function of the frequency f (see figure 6.17a). Making a linear fit to the first part of the (smoothed) spectrum gives the slope $\frac{\Delta\phi}{\Delta f}$ (see figure 6.17b). Dividing this slope by 2π gives through equation (6.3) a value for τ. With this method one finds for shot #1521, LP #3 and #4, a time lag of about 6.1 µs which corresponds with a poloidal velocity of about $819\,\mathrm{m\,s^{-1}}$. This value is roughly 40% higher than the poloidal velocity obtained through method 1, where the time lag is directly derived from the cross–correlation function. Nevertheless both methods give a result that is of the same order of magnitude and has the same sign (i.e. rotation in the same direction). Above the correlation between both LPs is very high, almost 90% (see figure 6.16b). Therefore it seems reasonable that the observed poloidal velocity (and hence plasma rotation) is not just a mathematical artifact but has a underlying physical process.

6.3 Floating potential mode

A third kind of experiments is based on the measurement of the floating potential. To this end the power supply is disconnected from the probes and the probes are left floating. Notice that the measured current must be close to zero when floating potential is measured (see equation (3.6)).

6.3.1 Background noise

The measurements in floating mode suffer less from background noise. There is no parasitic effect from the power supply because it is not switched on. Nevertheless there is sometimes an

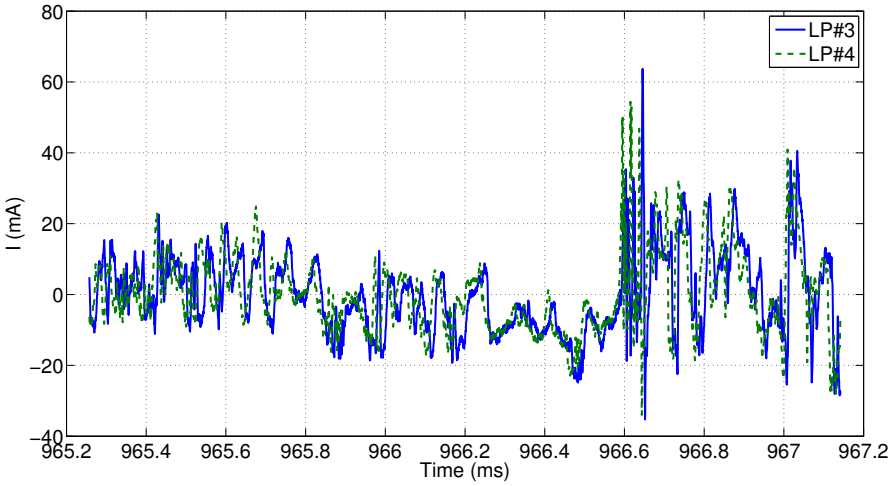

(a) Corrected current signals for LP #3 (ful blue line) and LP #4 (dashed green line) in function of time. For both signals the mean value was substracted to clearly see the fluctuations.

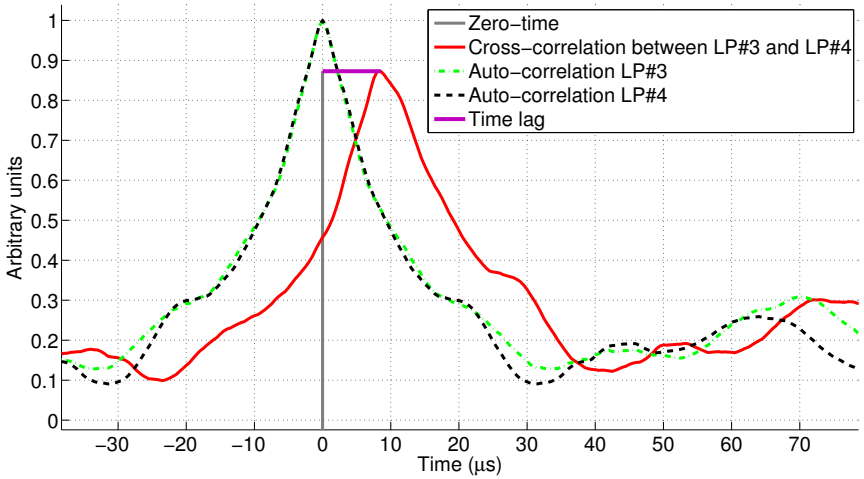

(b) Auto–correlation functions for LP #3 (dashed–dotted green line) and LP #4 (dashed black line) which indicates the zero–time (gray ful line). The time lag (ful purple line) is determined through the maximum of the cross–correlation function of both LPs (ful red line).

Figure 6.16: Time lag measurement between LP #3 and LP #4 for shot #1521.

off set present on the current signal which needs to be corrected.

6.3.2 Floating potential and the separatrix

Experimentally (see e.g. [34, 35, 36]) one has found that the profile of the floating potential typically increases starting from the plasma core till it reaches a maximum in the neighbourhood of the separatrix. From the separatrix to the plasma edge, the floating potential decreases again. This radial profile of the floating potential is a direct consequence of the difference in mobility between electrons and ions and turbulent processes, for a more profound discussion of the origin of the radial profile of the floating potential we refer to [34, 36]. In figure 6.18 the radial profiles of the floating potential and ion–saturation current are shown schematicly. The behaviour of the ion–saturation current is rather logical: towards the core a higher plasma density and thus a higher ion–saturation current (proportional to the plasma density) is expected.

Now it is possible to extract information about the movement of the plasma column based on

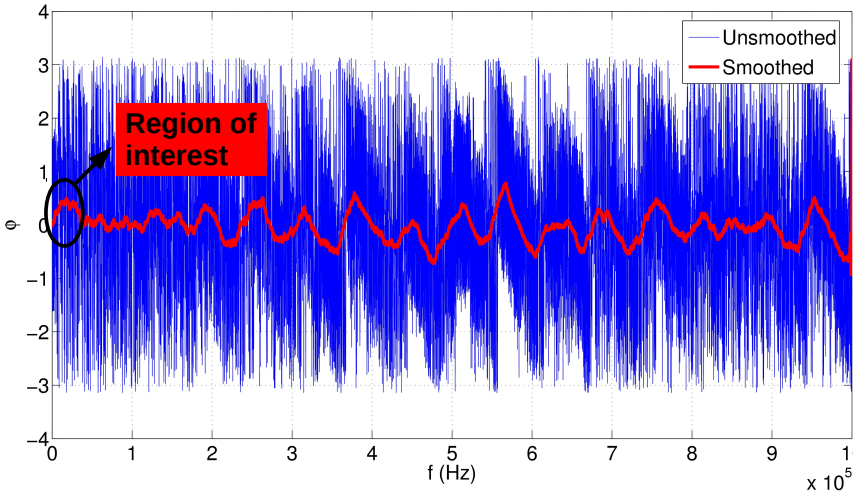

(a) ϕ in function of f. The blue line represents the unsmoothed phase whereas the red line represents the smoothed phase. The region of interest corresponds to figure 6.17b.

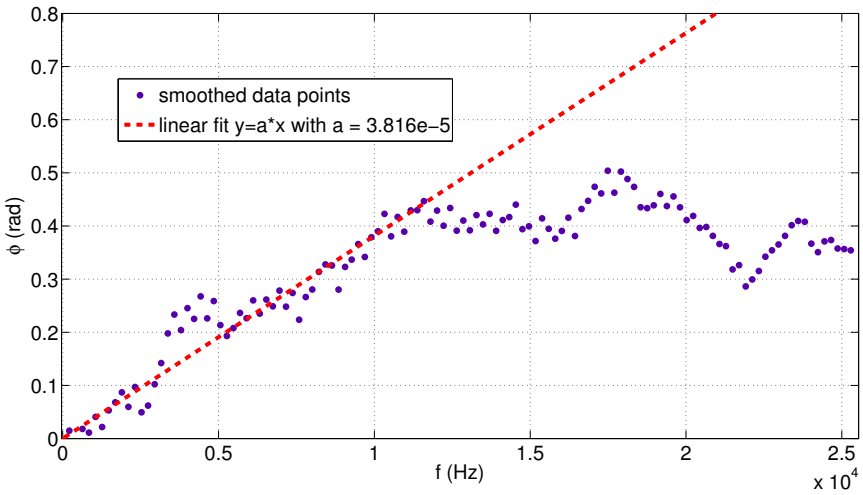

(b) Linear fit to the smoothed phase in the region of interest of figure 6.17a in order to determine the slope.

Figure 6.17: Determination of the time lag τ between LP #3 and #4 for shot #1521 by plotting the phase ϕ in function of the frequency f.

the spatial evolution of the floating potential in combination with the spatial evolution of the ion–saturation current. Hence a configuration is made whereby one LP measuring I_{sat} is surrounded by two LPs measuring floating potential. Figure 6.18 gives actually the spatial evolution of the floating potential and the ion–saturation current whereas the probes are fixed and measure the time evolution of these parameters. However we can consider the measurement with the LPs as a spatial evolution. Because the lack of a feedback system on the plasma position (see section 5.3) the plasma column is allowed to move inside the vessel. Hence, instead of the probes moving to or away from the plasma, it is the plasma itself that moves to or away from the probes.

6.3.3 Results and discussion

A configuration is set up whereby one LP measuring I_{sat} is surrounded by two neighbouring LPs measuring V_f. In figure 6.19 one can find the raw data output for shot #1535 where LP #6 measured I_{sat} and both surrounding LPs (#5 and #7) recorded V_f. For clarity also the

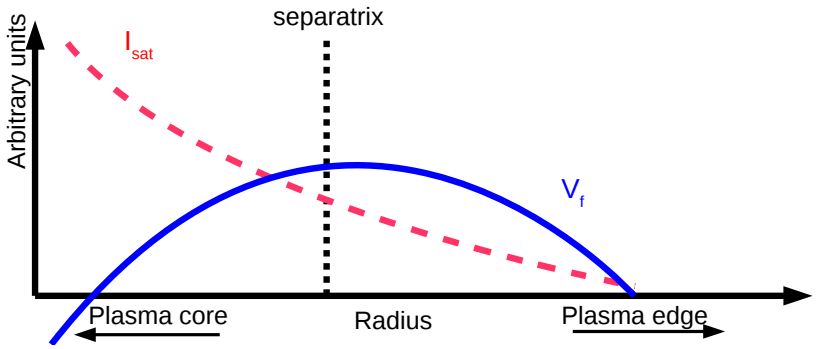

Figure 6.18: Schematic view of the floating potential and the ion–saturation current profile in function of the radius with respect to the separatrix.

plasma current is shown to indicate the beginning and the end of the shot. One can see that the interesting part of the shot lasts from 962.7 ms till 965.2 ms (we do not consider the time period after 965.2 ms because the shot was ended then).

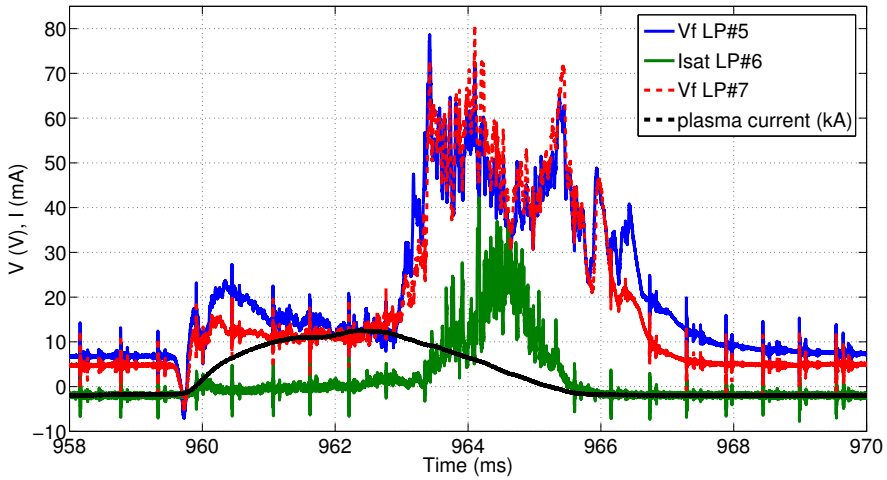

Figure 6.19: Time evolution of the ion–saturation current for LP #6 (green), floating potential for LP #5 (blue) and LP #7 (red) and the plasma current (black) for shot #1535.

From figure 6.19 one can see that the evolution of the floating potential is about the same for both LPs. Hence we can assume that the floating potential would have a similar behaviour if one used LP #6 for the measurement. Therefore we can consider the measurement of I_{sat} with LP #6 and V_f with for instance LP #7 as it happened on the same location. In figure 6.20 we plot, after removing the off–set, I_{sat} and V_f for LP #7 together for the time window of interest as mentioned above.

What can now be extracted from this figure? We see that I_{sat} increases till a time of 964.6 ms. This means, based on figure 6.18, that the probe is moving towards the plasma core or stated the other way around that the plasma is moving towards the probes. If meanwhile the probe is moving in front of the separatrix a increasing V_f should be observed. On the other hand V_f should decrease if the probe is moving beyond the separatrix towards the plasma core. In the time interval from about 964 ms till 964.6 ms we see that V_f is decreasing. Hence, based on these arguments, we can conclude that during this time window the LP (actually a kind of spatial average of LP #6 and LP #7) was located beyond the separatrix. To confirm this assumption

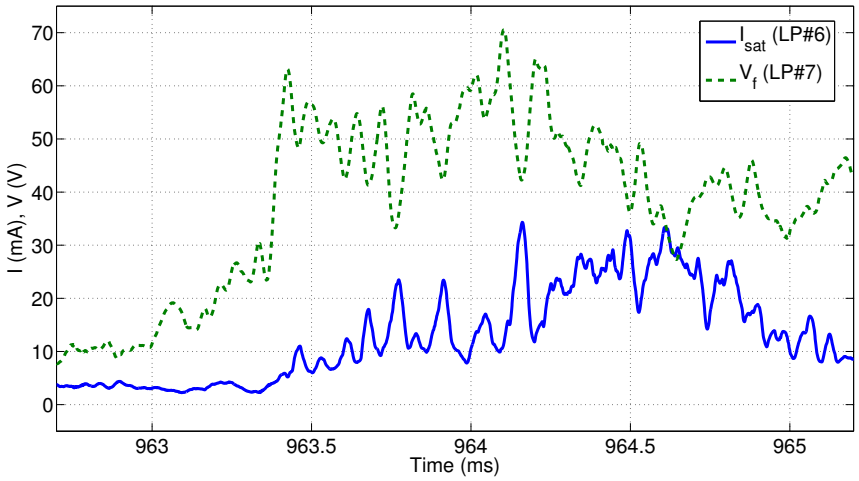

Figure 6.20: Time evolution of both ion–saturation current and floating potential for shot #1535. Both signals are smoothed to see a clear trend without the sharp fluctuations.

one should compare the result with the output for the position of the plasma from magnetic reconstruction. Unfortunately, the information of the plasma position for shot #1535 is only available till a time of 963.5 ms. Therefore no comparison can be made.

In total 17 shots (#1525–1542) were prepared in this configuration to measure the floating potential in combination with the ion–saturation current. From this set 12 shots produced plasma and 6 shots (#1531, #1535, #1538, #1540–1542) out of these 12 plasma shots were significant enough to extract possible plasma movement from the floating potential and ion–saturation current signals.

6.4 Indication of plasma position

Mostly the plasma position output from the magnetic reconstruction does not cover the same time range when data are collected on the LPs. As already explained this is a consequence of the lack of a feedback system controlling the plasma position. But in fact, the divertor probe can actually be used as a sensor to measure indirectly the position of the plasma column. As already demonstrated in section 6.3 information can be extracted about the plasma position by considering the relation between the evolution of the floating potential and ion–saturation current. In this section we will explicitely use two indirect ways of determining the plasma position based on the sweeping mode and the ion–saturation mode.

6.4.1 Sweeping mode configuration

Instead of using the sweeping mode to determine the time evolution of T_e, V_f and I_{sat}, as explained in section 6.1, one can directly use the presence (or absence) of a signal on a LP as an indication of the presence of the plasma column. A very simple way to detect the presence of the plasma is by putting five LPs in sweeping mode scattered over the whole divertor probe, whereby one choose to put LPs #1, #10, #19, #30 and #39 in sweeping mode (see also figure 5.1). This configuation was choosen for shots #1549–1561 from which 7 shots were real plasma shots (#1549–1551, #1557–1560).

6.4.2 Ion–saturation mode configuration

Similar one can also put the LPs #1, #10, #19, #30 and #39 in ion–saturation mode. The detection of ion–saturation current is an indication of the presence and thus the position of the plasma column. There were 4 plasma shots (#1545–1548) out of 6 shots in this configuration (#1543–1548).

6.4.3 Results and discussion

In figure 6.21 one can find an example of the signals on the LPs when operating in sweeping mode. For clarity only the current signal together with the plasma current is shown. From this figure one can observe a kind of time evolution of the plasma position. Apparently the plasma column was more located in the neighbourhood of LPs #19–39 because these LPs clearly exhibit $I-V$–characteristics which are an indication of the presence of plasma. Whereas the LPs at the high field side (#1–10) do not exhibit clear $I-V$–characteristics and the signals are a consequence of noise.

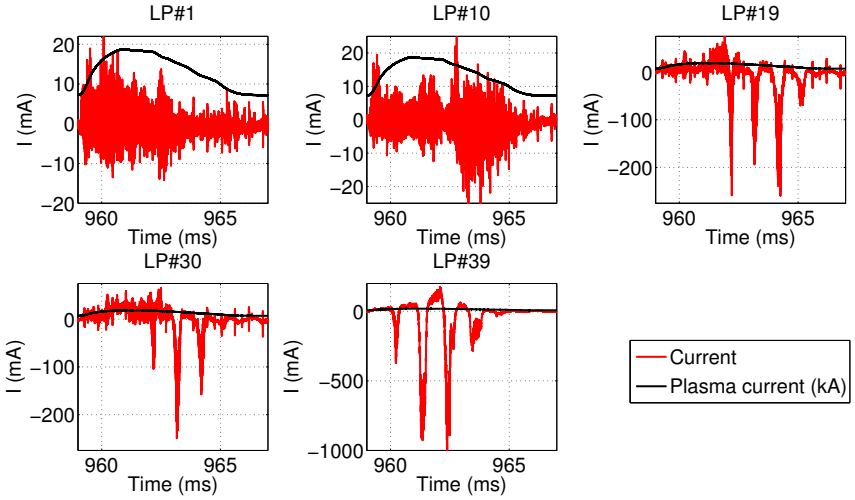

Figure 6.21: The current registred with the LPs for shot #1560 is shown (red) together with the plasma current (black) when the probes are operated in sweeping mode. Mind that the vertical scales are different whereas the horizontal scales are the same.

An equivalent result for the ion–saturation mode is shown in figure 6.22. One can see that during this plasma shot the ion–saturation signal becomes significant starting from probe #19 and is very clear for probe #39 (low field side). Therefore one can expect that the location of the plasma was more around LP #39.

6.5 Mixed experiments

Finally it is also possible to combine all three operating modes (sweeping, floating and ion–saturation) together in one experiment. One has the freedom to chose any of the 39 LPs and the mode in which it will be operating. An intelligent combination can provide useful information on different plasma parameters at the same time and make it possible to compare between the different modes. We will demonstrate such a mixed experiment through shot #1583, the last shot of the campaign. During this shot LPs #3 and #7 were operating in sweeping mode whereas LPs #4 and #6 were set floating. The probe in the middle, LP #5, measured the ion–saturation current. The output is shown in figure 6.23.

One can now analyse the data as discussed in the previous sections. As explained in section 6.1 one can derive T_e, I_{sat} and V_f using the sweeping LPs by fitting equation (3.23) to the $I-V$–

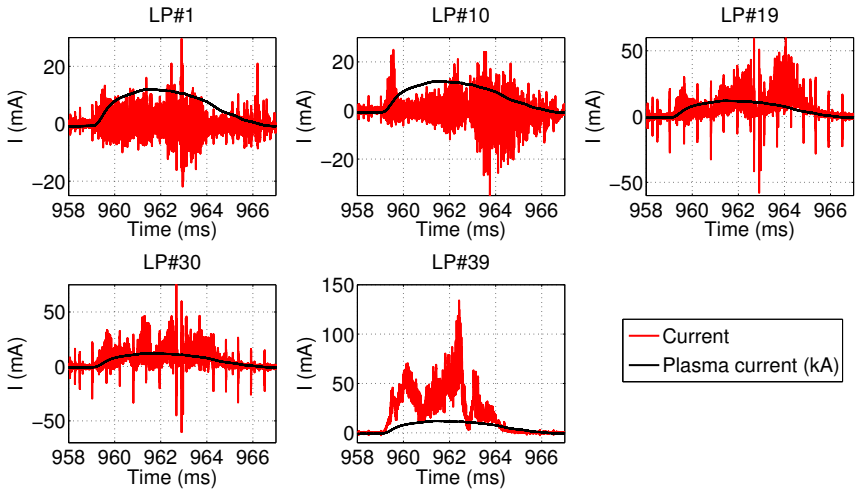

Figure 6.22: The current registred with the LPs for shot #1547 is shown (red) together with the plasma current (black) when the probes are operated in ion–saturation mode. Mind that the vertical scales are different whereas the horizontal scales are the same.

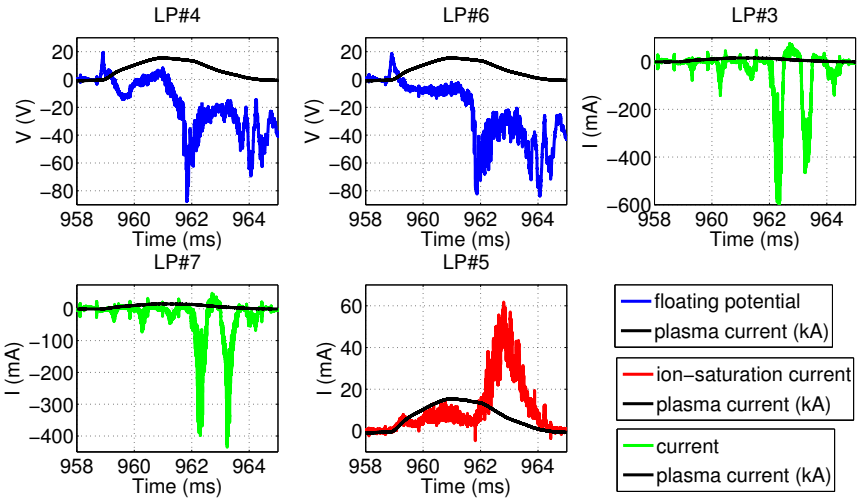

Figure 6.23: Data output for shot #1583. LPs #3 and #7 are in sweeping mode, LPs #4 and #6 are left floating and LP #5 measures ion–saturation current. For clarity the voltages signals in case of sweeping mode and ion–saturation mode are not shown, whereas the current signal for the floating potential measurements are omitted. The plasma current is plotted to indicate the duration of the plasma shot.

characteristics. One might like to compare the values for V_f and I_{sat} obtained directly from the corresponding probes with the values obtained from fitting. In figure 6.24a and 6.24b one can find the comparison between the values obtained from the sweeping mode and the corresponding direct measurements of the same quantity. Although only three $I-V$–characteristics from LP #3 could be used for fitting, the obtained results corresponds quite well with the direct measurements of the same plasma parameters in the small time window were the $I-V$–characteristics were recorded.

At the same time one can extract information about the plasmas position based on the relation between V_f and I_{sat} as explained in section 6.3. Therefor we plot the V_f recorded with LP #6 together with I_{sat} recorded with LP #5 as can be seen in figure 6.25. It is clear that the floating potential and the ion–saturation current are both rising during about 1 ms startting from 961.9 ms. After 962.9 ms both plasma parameters are decreasing till the end of the shot (around

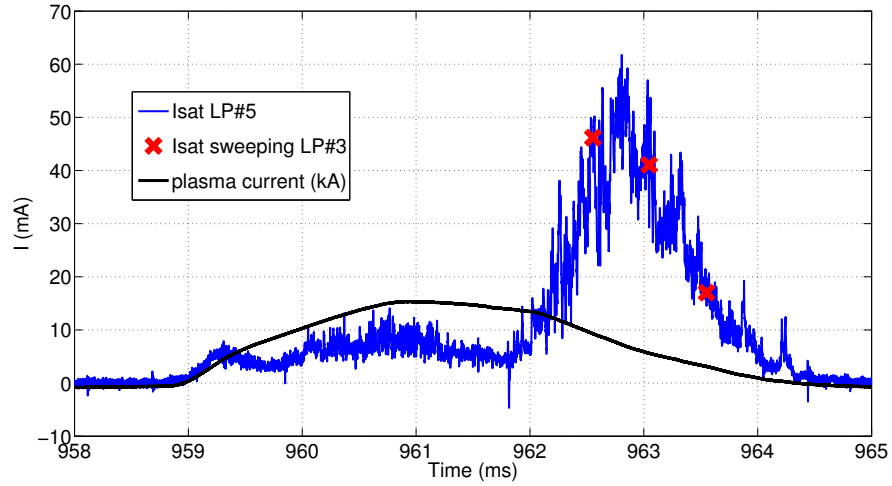

(a) The blue ful line represents I_{sat} as measured directly with LP #5, whereas the red crosses represents the fitted values obtained from LP #3.

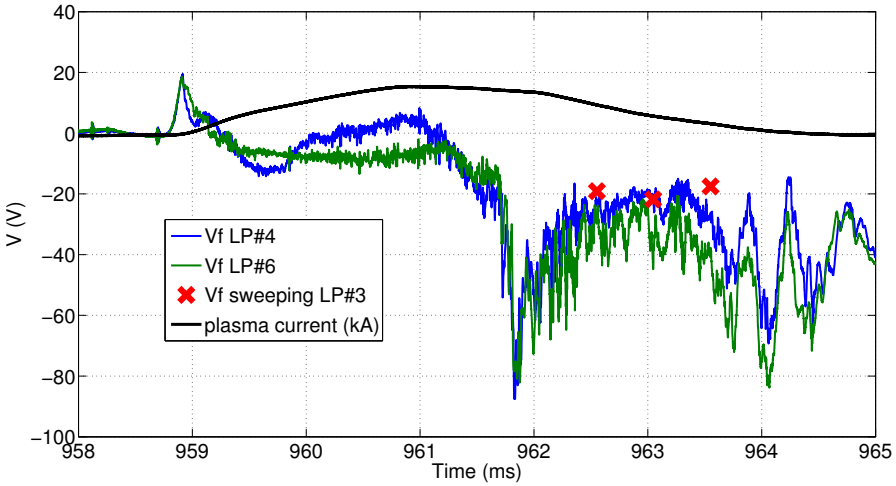

(b) The blue ful line represents I_{sat} as measured directly with LP #5, whereas the red crosses represents the fitted values obtained from LP #3.

Figure 6.24: Comparison of the direct values of V_f and I_{sat} with the values obtainded from fitting $I-V$–characteristics for shot #1583

964 ms). Based on the profile of I_{sat} (see figure 6.18) one can determine that the plasma column was moving towards the LPs during the time period 961.9 ms–962.9 ms, whereas the plasma is moving away again during the time period 962.9 ms–964 ms. Furthermore, based on the profile of V_f (see figure 6.18), it seems that the LPs stayed in front of the separatrix (i.e. at the plasma edge). Unfortunately the data about the plasma position from magnetics didn't cover this time window.

6.6 Conclusion

In this chapter we have discussed different kind of experiments with the divertor probe array consisting of 39 LPs. The data are obtained by biasing the probes with respect to the tokamak vessel. One distinguishes between three major operating modes of the LPs: **sweeping mode** (sweeping voltage), **ion–saturation current mode** (constant negative voltage) and **floating potential mode** (no bias).

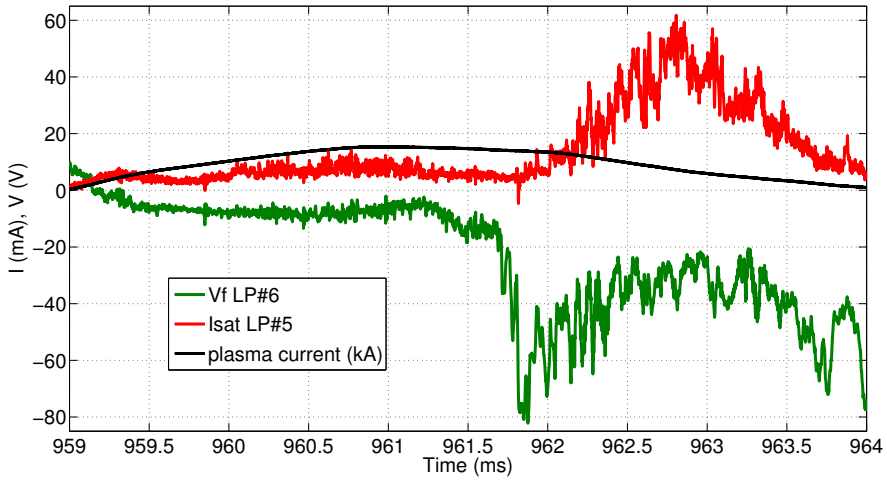

Figure 6.25: Time evolution of V_f (green) and I_{sat} (red), together with the plasma current (black) for shot #1583.

Using the LPs in sweeping mode provides a way to measure $I-V$–characteristics from which one can derive the electron temperature T_e, the floating potential V_f and the ion–saturation current I_{sat} based on Langmuir probe theory (see section 3.2). In section 6.1 we demonstrate that sweeping LPs are indeed very useful in determining these three basic plasma parameters.

The ion–saturation current mode is particularly useful for the direct measurement of the time evolution of the ion–saturation current which is related to the plasma density (see also section 3.2.5). Monitoring the plasma density can be important in the study of plasma turbulences which in turn is important in understanding particle transport, plasma confinement, etc. In section 6.2 the ion–saturation current mode is used to determine the correlation between different I_{sat} (and hence plasma density) signals on neighbouring LPs. From these correlations one can learn something about a possible rotation of the plasma column in the poloidal direction.

When the LPs are left floating one measures directly the floating potential of the plasma. Knowledge about this floating potential can learn us something about the plasma potential, as it is directly proportional to it (see equation (3.8)). On the other hand one can extract information about the movement of the plasma column based on the profile of the floating potential as is demonstrated in section 6.3.

The LPs can be used as a simple sensor for the plasma position. Chosing an appropriate arrangement of active LPs along the divertor array make it possible to detect the presence or absence of plasma. These simple plasma position techniques are shown in section 6.4

Finally one has the freedom to combine LPs in different operating modes during one plasma discharge. The results can be used to check if they are consistent whith each other. Furthermore one is able to derive different kinds of information from the plasma at the same time (e.g. V_f, T_e, I_{sat}, plasma position, plasma rotation, etc.) whereas this is not possible when the probes are used in one single mode. An example of such a mixed experiment is presented in section 6.5.

One can conclude that LPs, although there relative simplistic design and operation but sometimes difficult interpretation, are an important diagnostic tool in determining the properties of the plasma edge.

Chapter 7

Measurements with the reciprocating manipulator

7.1 Measurement of the plasma potential and determination of electron temperature

As explained in section 4.2 it is possible to measure directly the plasma potential with a BPP. The probe head of the reciprocating manipulator is equipped with four BPPs (see section 5.2) and hence one makes use of this probe system for the experiments in the following chapter. In order to measure the plasma potential with a BPP one needs to leave this BPP floating. The measured floating potential than corresponds to the plasma potential. This way of determining the plasma potential is more accurate than using equation (3.8) with the knowledge of the floating potential and electron temperature, which can be measured with for example sweeping LPs (see section 6.1). Using (3.8) would then give the plasma potential. Major drawback is that the measured values of the floating potential and the electron temperature are always averaged values over a certain time window (in section 6.1 the time window corresponds with half of the period of the sweeping frequency). Hence the time evolution of the plasma potential is somehow smoothed out if one use sweeping LPs and equation (3.8). On the other hand the use of floating BPPs is a better way to determine the time evolution of the plasma potential as the time resolution is limited only by the sampling frequency (i.e. 2 MHz). In figures 7.1a and 7.1b two examples are given for the direct measurement of the plasma potential with floating BPP #2 (see figure 5.4a). it has to be mentioned that there was a background noise present on the signals in the disguise of an off–set for which we have made a correction.

On the other hand if one looks back at equation (3.8) and rewritte it as follows:

$$T_e = \frac{V_p - V_f}{\ln(\delta)} \tag{7.1}$$

This suggests that one can determine the electron temperature once V_p, V_f and δ are known. Now V_p is simply measured by a BPP left floating. To know the value of V_f one could use a floating LP left at the same position of the BPP. For δ one takes the value of 2.8 for a hydrogen plasma. Note that this value is actually derived from Langmuir probe theory in non–magnetised plasma which is thus not correct. Nevertheless this value is a first good estimation for δ.

In practice the LP can not be on the same position of the BPP but one uses a LP close to the considered BPP. In this experiment LP #2 and BPP #2 (see figure 5.4a) were used as floating probes. Furthermore the probe head of the reciprocating manipulator was located in the midplane (z =0 mm) and at a radial position of R =768 mm, i.e. at 208 mm from the tokamak center towards the low field side (see also section 5.3 for the coordinate conventions used). This configuration is valid for shots #1537–1548 which are analysed in the current section.

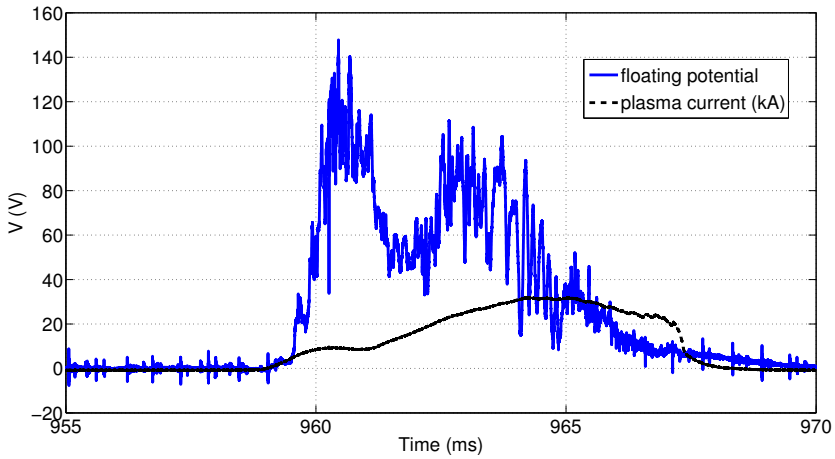

(a) Corrected floating potential in function (ful blue line) of time for shot #1540 and BPP #2.

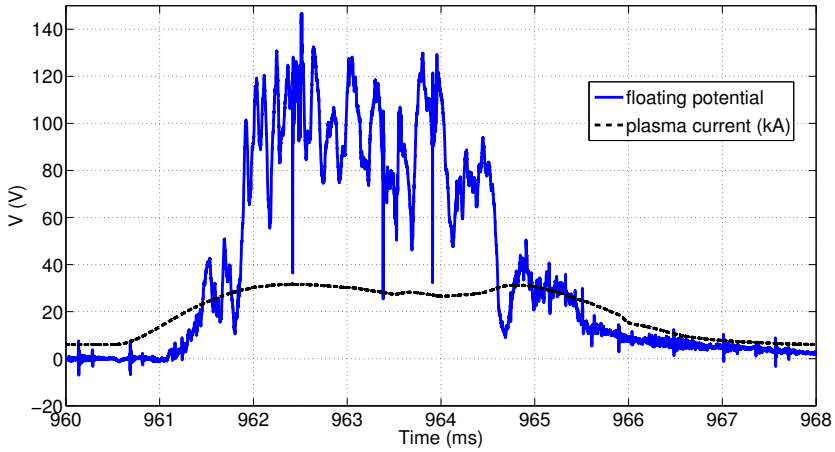

(b) Corrected floating potential in function (ful blue line) of time for shot #1545 and BPP #2.

Figure 7.1: The floating potential corresponds directly with the plasma potential. The plasma current (dashed black line) indicates the duration of the plasma shot.

Applying equation (7.1) on the measured voltage signals from LP #2 (i.e. V_f) and BPP #2 (i.e. V_p) gives the time evolution of the electron temperature. In figures 7.2a and 7.2b two examples are shown. For clarity also the plasma current is shown which is an indication for the duration of the shot. One can see that the determination of the electron temperature by means of equation (7.1) gives a real–time evolution of the temperature. For shot #1542 one can see in the time interval from 960 ms till 965 ms that the electron temperature is roughly constant with a value of 7 eV. Afterwards the electron temperature is decreasing with finally at the end some large fluctuations. For shot #1548 the electron temperature has more fluctuations and has not really an average value for a specific time interval. It has to be noticed that in both shots the electron temperature becomes negative sometimes. This is not physically possible. One can see that the negative temperatures mainly show up in the beginning and at the end of the shot. During this time periods it seems very plausible that the plasma is not stabilised and not in thermodynamic equilibrium and hence is not behaving Maxwellian. As a consequence it possible that there is a high–energy tail of so–called suprathermal electrons. As a result equation (7.1) is not valid anymore.

In comparison with measurements from sweeping LP measurements one has a higher time

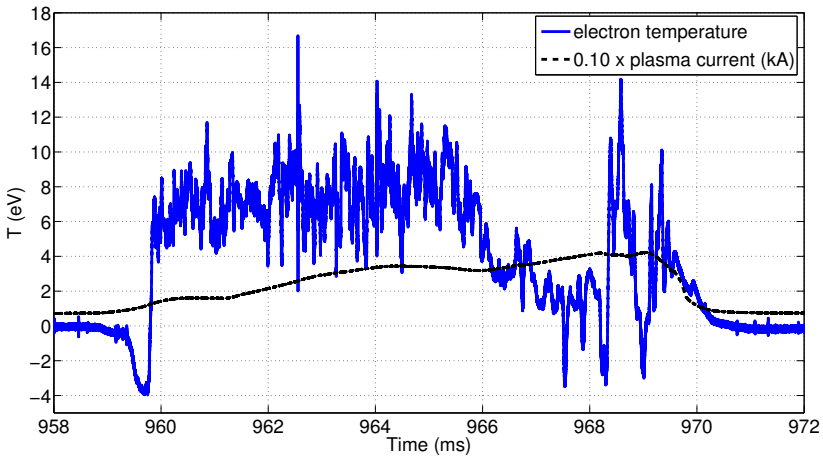

(a) Electron temperature (ful blue line) in function of time for shot #1542

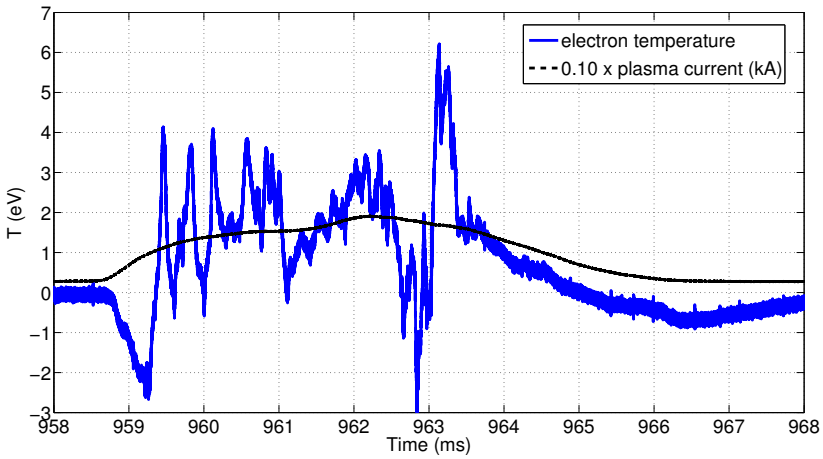

(b) Electron temperature (ful blue line) in function of time for shot #1548

Figure 7.2: Determination of the electron temperature with equation (7.1). The black dashed line represents the plasma current (divided by a factor 10).

resolution for the electron temperature in this case. Whereas the time resolution in the former method is actually limited by the sweeping frequency (see also section 6.1.3), now one has a time resolution corresponding with the sampling frequency of 2 MHz. The time evolution of the plasma position (see section 5.3 for the conventions of the plasma position) determined from magnetic reconstruction techniques has the same sampling frequency. Hence we can try to link the time evolution of the electron temperature with the time evolution of the plasma position. In figures 7.3 till 7.4b the time evolution of respectively the electron temperature, the radial plasma position and the vertical position are plotted for a time range from 964 ms till 965.5 ms for shot #1540. From figure 7.4b it is clear that the plasma column is above the mid plane and is almost stable around z =25 mm. Therefore we neglect the effect of the change in the vertical plasma position on the measurements of the electron temperature. On the other hand the plasma column is moving further towards the high field side, see figure 7.4a. At the same time one can see from figure 7.3 that the electron temperature has a decreasing trend with increasing time. Hence it seems plausible that the electron temperature is decreasing because the plasma column is moving radially away from the probe head of the reciprocating manipulator (i.e. towards the high field side).

In figure 7.5 the electron temperature is finally plotted against the radial position of the

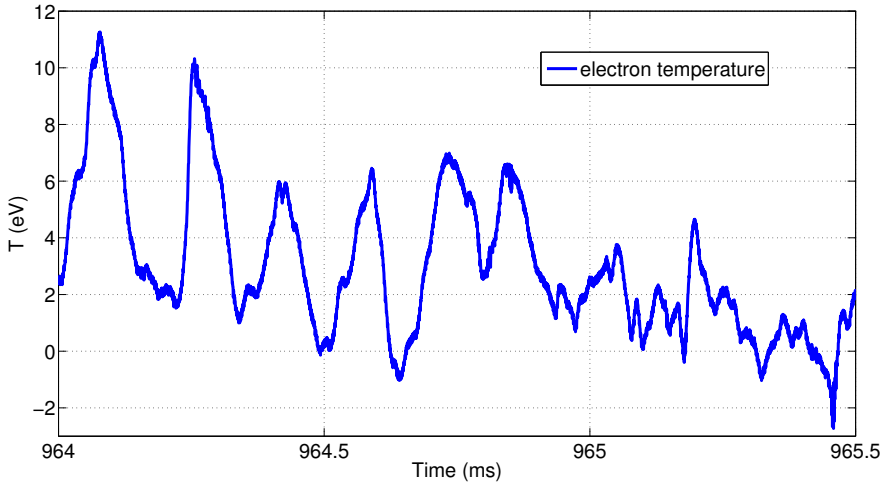

Figure 7.3: Time evolution of the electron temperature for shot #1540 during the time window 964 ms–965.5 ms.

plasma as measured with magnetic reconstruction techniques. One can see that the electron temperature is indeed decreasing as the radial plasma position decreases (i.e. the plasma column is moving away from the probe head which is located at z =0 mm and R =768 mm and is not reciprocating). If one compares this with figure 7.4a it is clear that the radial position decreases with time. Hence time evolution in figure 7.5 is from the left to the right. This figures is obtained by smoothing the original electron temperature signal (see 7.3) in order to see the decreasing trend with time. From figure 7.4b we know that the plasma is located above the mid plane during the considered time period. Thus the probe head of the reciprocating manipulator is not really in direct contact with the plasma and hence a relatively low electron temperature is expected which is confirmed by the measurement (less than 10 eV). To conclude one can say that the decrease in electron temperature can be a consequence of the fact that the plasma is moving to the high field side during the selected time window whereas the probe head is located at the low field side.

7.2 Conclusion

In this chapter the first results with the reciprocating manipulator on COMPASS were analysed. Although the reciprocating option was not operational during the campaign, the reciprocating manipulator gave interesting results concerning BPPs. In contrary to LPs, BPPs can measure directly the plasma potential by an appropriate configuration of the collector pin with respect to the shielding (see section 4.2 and figure 5.4). We have demonstrated that these direct plasma potential measurements give good result with a good time resolution.

Using the data of a floating LP in combination with the plasma potential measured with a BPP gives the electron temperature through equation (7.1). Although this equation is derived from ideal Langmuir probe theory (see section 3.2), it is a good first order approximation. In section 7.1 we show the results for the electron temperature determined in this way. Finally we compare the time evolution of the electron temperature and the plasma position in order to explain the observed behaviour of the electron temperature.

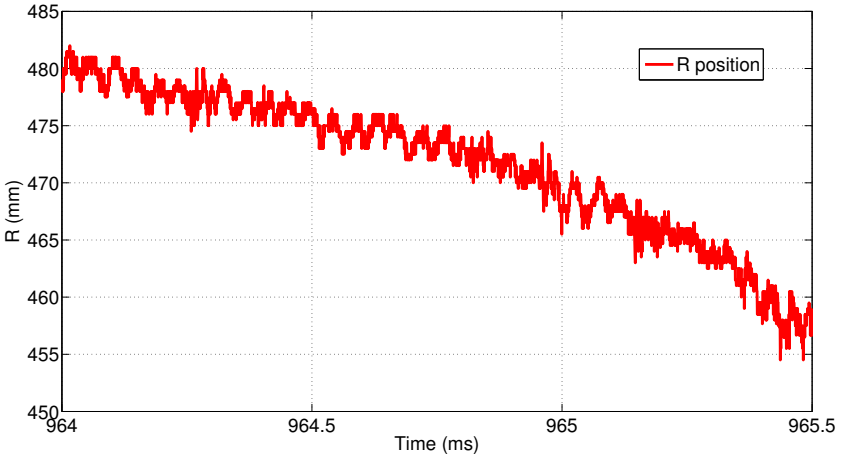

(a) Time evolution of the radial position.

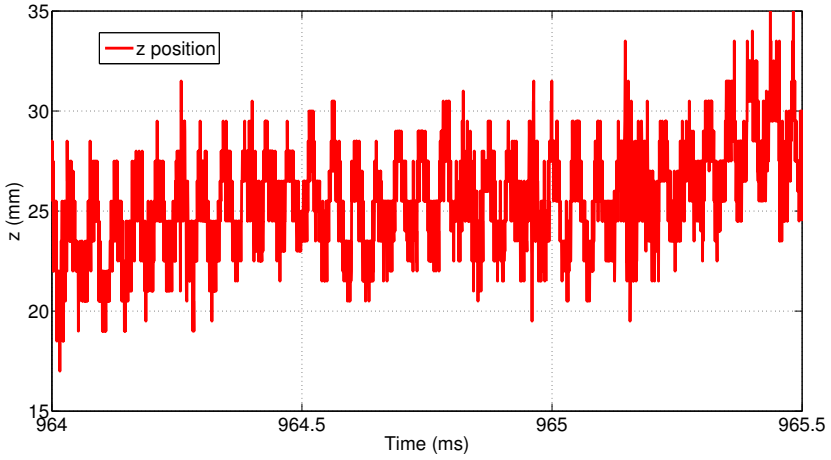

(b) Time evolution of the vertical position.

Figure 7.4: Time evolution of the plasma position (see also section 5.3) for shot #1540 during the time window 964 ms–965.5 ms.

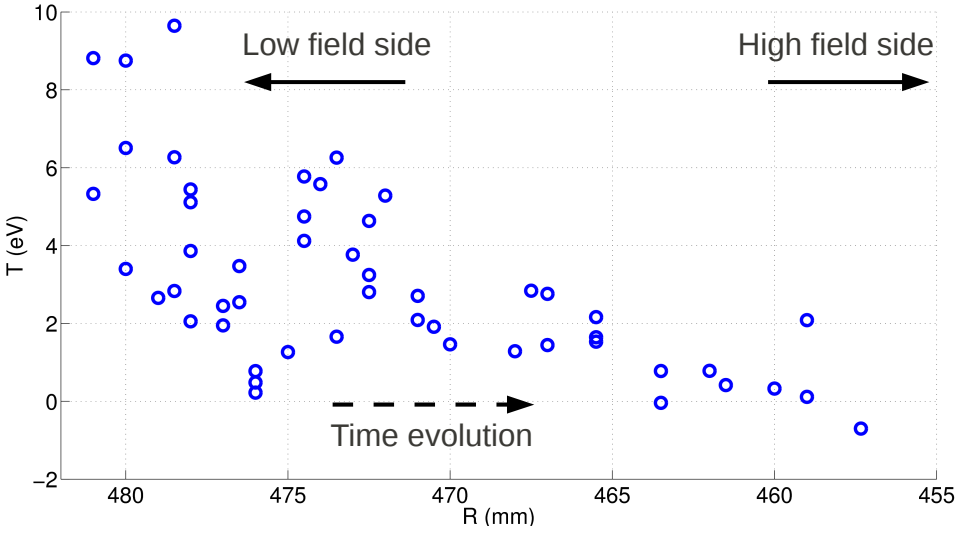

Figure 7.5: The electron temperature as measured with the BPP#2 and LP#2 (both located at R =768 mm and not reciprocating) in function of the radial plasma position as measured with magnetics for shot #1540.

Part IV

Closure

Chapter 8

The GOLEM tokamak

8.1 Introduction

During my staying in Prague I have participated the SUMmer TRAIning Course (SUMTRAIC) 2010. During this summerschool one day was devoted to perform experiments on the GOLEM tokamak. Hence it is worthwhile to include some data of that campaign and to extract some basic information from it.

Figure 8.1: "Mascot" of the GOLEM tokamak [37].

8.2 History

The history of GOLEM goes back to the early sixties. At that time GOLEM was called TM–1 and was located in the Kurchatov Institute in Moscow, former Sovjet–Union. This tokamak was actually one of the first working fusion machines based on the tokamak concept. In 1975 TM–1 moved to the IPP in Prague, former Czechoslovakia, and was named TM–1 MH. In 1985 it was renamed to CASTOR which stands for Czech Academy of Sciences TORus. CASTOR was intensively used as a fusion research machine from 1977 till 2006. In 2004 the tokamak COMPASS located at Culham, UK, was offered to IPP Prague. The offer was accepted and CASTOR needed to make place for this new tokamak COMPASS. As a consequence CASTOR was offered to the Faculty of Nuclear Sciences and Physical Engineering of the Czech Technical University. Hence CASTOR moved to his new location and was renamed GOLEM. This rather strange name finds its origin in a jewish legend whereas the building were the tokamak is located, is situated in the jewish neighbourhood of Prague. A "golem" is namely some kind of creature made of mud that was brought alive by the jewish rabbi Löwe. This "golem" was intended to serve and protect the jewish people as it did. In that context the GOLEM tokamak can be considered

as serving students and scientists in the learning process about fusion. The GOLEM tokamak is nowadays not so important anymore because it is rather small and only a limited selection of diagnostics are available (see section 8.4). However it is rather unique in his kind because it can be operated by remote control. Any one who would want to perform an experiment can operate GOLEM from his/her home location. An internet connection is sufficient to modify[1] the controllable parameters of the tokamak and to execute real plasma shots. After the experiment the data appear on the online archive [38].

Although it is the oldest active tokamak in the world, GOLEM is at the same time, quite paradoxically, one of the most modern tokamaks because of its rather unique internet remote control. An to honor its name, GOLEM has a special "mascot" as can be seen in figure 8.1. It represents the golem creature from the jewish legend. Inside the sculpture there is room for a small candle which needs to be lighted before every experiment in order to "put the infernal power of fusion into GOLEM".

8.3 Short technical overview

The GOLEM tokamak is a small tokamak with main parameters:

- Major radius $R_0 = 0.4\,\mathrm{m}$
- Minor radius $a = 0.1\,\mathrm{m}$
- Radial position of the limiter $r = 0.085\,\mathrm{m}$
- Hydrogen plasma

In figure 8.2 one can find a engineering scheme of GOLEM. For more technical details and how GOLEM operates we refer to the GOLEM webpage [37] and the instruction guide for the tokamak [39].

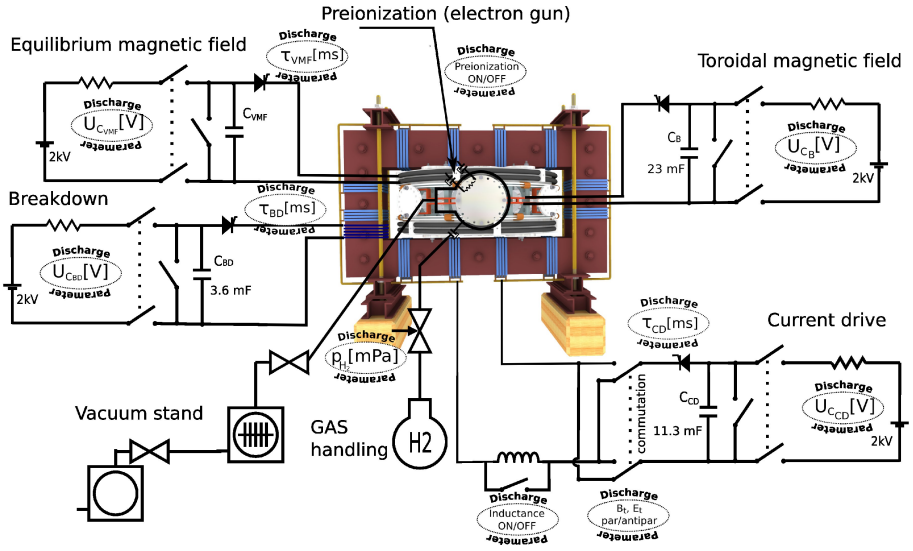

Figure 8.2: Engineering scheme of GOLEM [37].

[1] Of course one first needs to contact the operator (`svoboda@fjfi.cvut.cz`) and to make a request for an experiment.

8.4 Diagnostics

Due to limited funding and working staff only a limited amount of diagnostics are available. In figure 8.3 one can find a overview of the available diagnostics. There is:

- a single loop around the transformer core to measure the loop voltage U_{loop}.
- a Rogowski coil, surrounding the tokamak chamber to measure the sum of the plasma and chamber current $I_{\text{p+ch}}$.
- a small pick–up coil placed on the tokamak chamber to measure the toroidal magnetic field B_t.
- a photocell facing a glass port of the tokamak to measure the plasma radiation in the visible part of the spectra.

We refer again to [37] and [39] for more information about the diagnostics. All the obtained experimental data from these diagnostics are digitized by a sampling frequency of 100 kHz and stored by a PC. Later on the data can be accessed via the online archive (see [38]) to which we refer for more details about the shots from the following section.

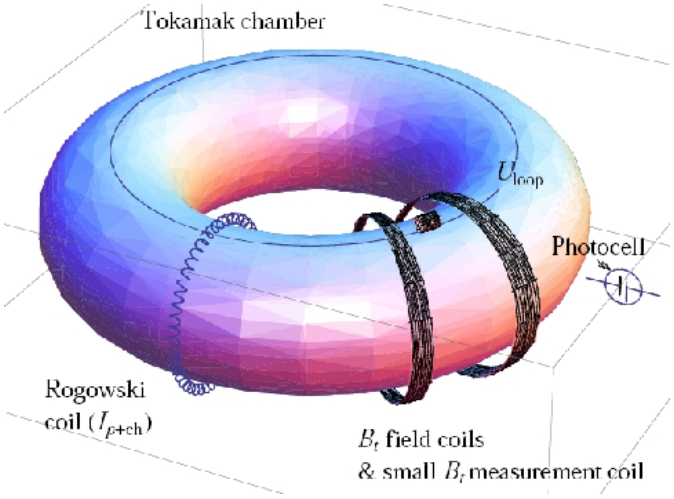

Figure 8.3: Diagnostics available on GOLEM [37].

8.5 Experiments and results

8.5.1 Goal of the experiment

The data obtained from the plasma discharge on GOLEM are used to determine the **energy confinement time** τ for different plasma parameters. We have choosen to determine the energy confinement time because it is a very important fusion parameter. We have not discussed this parameter in the chapters about COMPASS therefore a short derivation is given here [39, 34].

Plasma heating power

The only heating source for the plasma in the GOLEM tokamak is current driven Ohmic heating. The power of this heating mechanism is simply given by:

$$P_{OH}(t) = U_{loop}(t) I_{pl}(t) \tag{8.1}$$

with U_{loop} the loop–voltage and I_{pl} the plasma current which both can be read from the online database.

Central electron temperature

It can be shown that the specific resistivity of a fully[2] ionised plasma only depends on the central electron temperature T_e and the effective charge of the plasma Z_{eff}. On can find that:

$$T_e(t) = \left(\frac{R_0}{r^2} \frac{8 Z_{eff}}{1.544\, 10^{-3}} \frac{1}{R(t)} \right)^{\frac{2}{3}} \tag{8.2}$$

$$\approx 80 \left(\frac{I_{pl}(t)[kA]}{U_{loop}(t)[V]} \right)^{\frac{2}{3}} \tag{8.3}$$

where in (8.2) the estimation $Z_{eff} = 2.5$ is taken, R_0 and r are determined in section 8.3 and $R(t)$ is the plasma resistance. In (8.3) the numerical values are filled in such that T_e is expressed in units eV.

Actually equation (8.3) is not correct because the Ohmic relation $U_{loop}(t) = R(t) I_{pl}(t)$ is not valid. Instead one needs to take into account the inductance of the circuit:

$$U_{loop}(t) = R(t) I_{pl}(t) + L \frac{\mathrm{d}I_{pl}(t)}{\mathrm{d}t} \tag{8.4}$$

with L the inductance, which is not exactly known. Hence one choses the moment when the plasma current I_{pl} reaches its maximum (i.e. $\frac{\mathrm{d}I_{pl}(t)}{\mathrm{d}t} = 0$), in this case equation (8.4) reduces to the simple law of Ohm: $U_{loop} = R I_{pl}$. Therefore expression (8.3) is used when I_{pl} is maximal and the more correct form of (8.3) is:

$$Te(t_0) = 80 \left(\frac{I_{pl}(t_0)[kA]}{U_{loop}(t_0)[V]} \right)^{\frac{2}{3}} \tag{8.5}$$

with t_0 the moment of time when I_{pl} reaches its maximum.

Plasma density

The plasma density n is estimated based on the ideal gas law because of the lack of real density measurement techniques on GOLEM. Taking into account that the tokamak vessel is filled with hydrogen gas and assuming a ionisation degree of 100%, one gets:

$$n = \frac{2 p_{ch}}{k_B T_{ch}} \tag{8.6}$$

with p_{ch} the chamber pressure and $k_B T_{ch}$ the thermal energy corresponding with the chamber temperature T_{ch}. Notice that this expression for the plasma density is a very crude estimation and thus can be considered as an upper limit for the real plasma density.

Plasma energy

With the expression for the central electron temperature (see equation (8.2)) and for the plasma density (see equation (8.6)) one can calculate the total energy content of the plasma $W(t)$:

$$W(t) = \frac{n k_B T_e(t) V}{3} \tag{8.7}$$

with $V = \pi r^2 2\pi R_0$ the plasma volume.

[2] One assumes for simplicity that the plasma in GOLEM is fully ionised.

Energy confinement time

We now have an expression for the energy content of the plasma $W(t)$ at certain moment of time (equation (8.7)) and for the plasma Ohmic heating power $P_{OH}(t)$ (equation (8.1)). During the quasi–stationary phase of the plasma discharge the energy losses of the plasma are balanced by the heating power which can be expressed as:

$$P_{OH}(t_{\text{balance}}) = \frac{W(t_{\text{balance}})}{\tau} \tag{8.8}$$

Herein t_{balance} stands for the moment when the plasma column is in the quasi–stationary phase. In practice one usually takes this moment equal to the moment t_{max} when the plasma energy content is maximalised. Therefore one defines the energy confinement time τ[3] as the ratio of energy content to heating power when the energy content is maximal. As explained in the discussion of the central electron temperature, the electron temperature is determined at time t_0, i.e. when the plasma current is maximal. Therefore we identify t_0 with t_{max}[4] and one gets for τ:

$$\tau = \frac{W(t_0)}{P_{OH}(t_0)} \tag{8.9}$$

The energy confinement time is an indication for the time scale on which the plasma loses its energy. The longer τ, the better the plasma is confined. Towards future fusion power plants it is important to have a energy confinement time as high as possible in order to achieve a maximal energy field.

8.5.2 Results

Energy confinement time in function of inserted gas pressure

In this section one examines the relation between the energy confinement time τ and the pressure of the inserted H_2–gas p_{H_2}. The pressure was increased with steps of roughly 5 mPa startting from 15 mPa till 50 mPa (shots #3480–3484 and #3495–3498). Meanwhile the other controllable parameters were set to: voltage for toroidal magnetic field U_b =1200 V, voltage for Ohmic heating U_{OH} =500 V and a time delay between U_b and U_{OH} = of 3 ms. In figure 8.4 one can find τ (calculated with equation (8.9)) in function of the effective pressure p_{H_2}.

One can see that τ roughly increases with increasing gas pressure. This behaviour is expected because a higher gas pressure induces a higher plasma density. As a consequence the plasma energy will be higher (equation (8.7)) and hence also the energy confinement time τ. The observed increasing trend of τ with p_{H_2} can be compared with the so–called **NeoAlcator–scaling**[5], which states in its original form [40]:

$$\tau_{\text{scaling}} = 1.9\,10^{-21} n R_0^2 a \tag{8.10}$$

where the confinement τ_{scaling} time is expressed in units of μs, the plasma density n in units m^{-3} and the major radius R_0 and minor radius a in units m.

In figure 8.5 the measured values for τ are plotted against n (see equation (8.6)) instead of p_{H_2} in order to take into account the small variations in chamber–temperature and to directly use the alcator–scaling. Using the values for R_0 and a gives, through equation (8.10), a linear relation of τ_{scaling} in function of n. However the general rising trend is observed, the confinement time is systematically to high. Therefore the scaling relation (8.10) is normalised with the data.

[3] Strictly seen it is not the real energy confinement time but only the electron component of the energy confinement time. This because any contribution from the ion–temperature is completely neglected in expression (8.7).

[4] In fact this statement is not completely correct because the energy content is not necessarily maximal when the plasma current is. Anyhow it can be a first rough approximation for τ.

[5] This scaling relation was derived from experiments performed on the ALCATOR tokamak (acronym for ALto CAmpo TORus, Italian for high field torus) during the seventies of the last century.

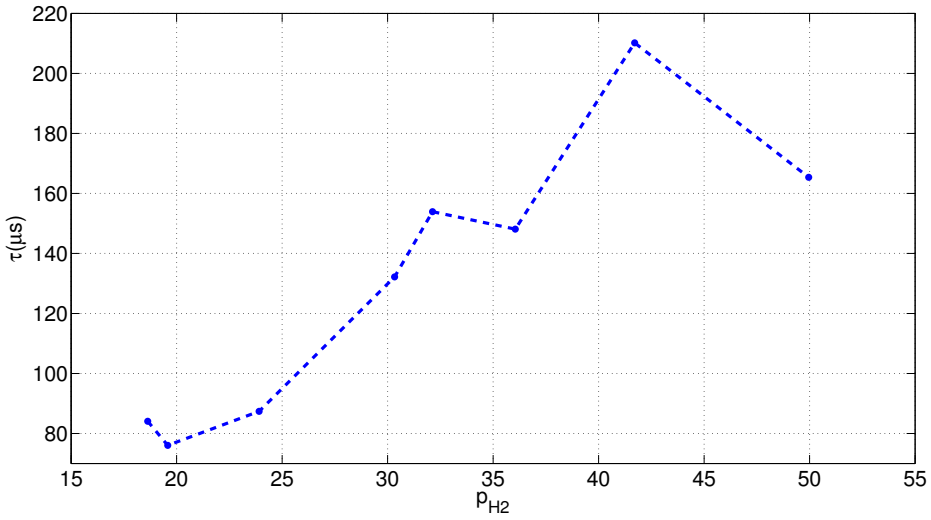

Figure 8.4: Energy confinement time τ in function of inserted gas pressure p_{H_2}. The mean plasma current I_p for these measurements varied between 2.1 kA and 2.5 kA with a slightly different value of 1.7 kA around p_{H_2} =36 mPa. The values for the mean toroidal magnetic field varied between 406 mT and 437 mT.

This is done at two different ways. The first way takes a linear fit as equation (8.10) but with a different value for the coefficient:

$$\tau_1 = A_1 R_0^2 an \tag{8.11}$$

the second way also includes a constant term B in the linear fit:

$$\tau_2 = A_2 R_0^2 an + B \tag{8.12}$$

The results for both fittings are shown in figure 8.5. This demonstrates that, eventhough a rough estimation for the plasma density n (see equation(8.6)) and τ (see equation (8.9)) is used, the results are qualitatively reasonable.

The reason why the scaling relation needs to be normalised to the data is because one needs to take into account radiation losses typical for the GOLEM tokamak. The energy balance expressed in (8.8) must actually be written as:

$$P_{OH} - P_{rad} = \frac{W}{\tau} \tag{8.13}$$

where P_{rad} takes into account the part of the ohmic heating power that is lost by radiation losses instead of heating the plasma electrons. The radiation losses are a consequence of impurities inside the vacuum chamber. In GOLEM the vacuum inside the vessel has a rather low quality which means that quite a lot of impurities are present in the plasma and hence a considerable amount of heating power is lost by radiation.

Energy confinement time in function of applied voltage for the toroidal magnetic field U_b

An other experiments deals about the relation between τ and the applied voltage for the creation of the toroidal magnetic field U_b. During shots #3470–3474 one increase U_b with steps of 120 V starting from 720 V till the maximum of 1200 V. Meanwhile the other controllable parameters were set to: gas filling pressure p_{H_2} of about 20 mPa, voltage for Ohmic heating U_{OH} =500 V and a time delay between U_b and U_{OH} = of 3 ms. In figure 8.6 one can find the results.

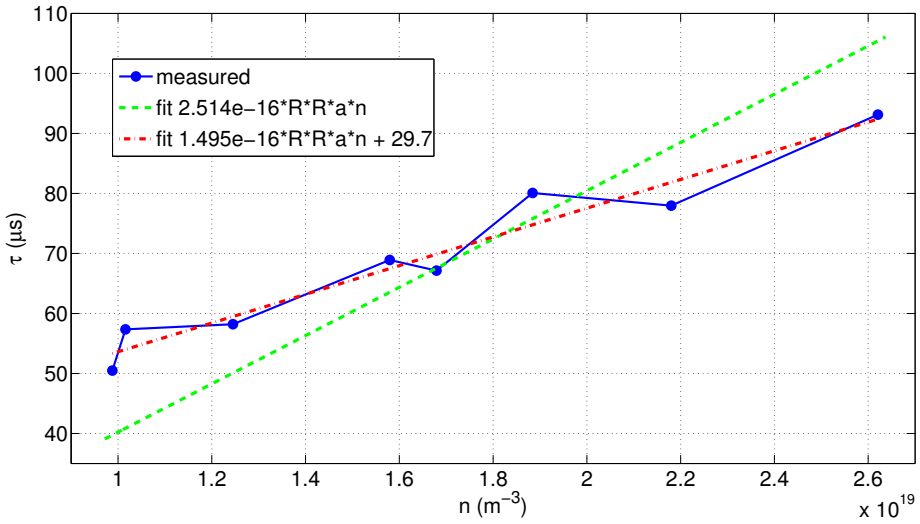

Figure 8.5: Energy confinement time τ in function of plasma density n (ful blue line). The dashed green line and the dashed–dotted red line represents two different fitted NeoAlcatar scalings as explained in the text. The mean plasma current I_p for these measurements varied between 2.1 kA and 2.5 kA with a slightly different value of 1.7 kA around p_{H_2} =36 mPa. The values for the mean toroidal magnetic field varied between 406 mT and 437 mT.

One can observe that τ is generally increasing with increasing U_b. This behaviour seems logical because a increasing voltage U_b induces a higher toroidal magnetic field and hence the plasma becomes better confined.

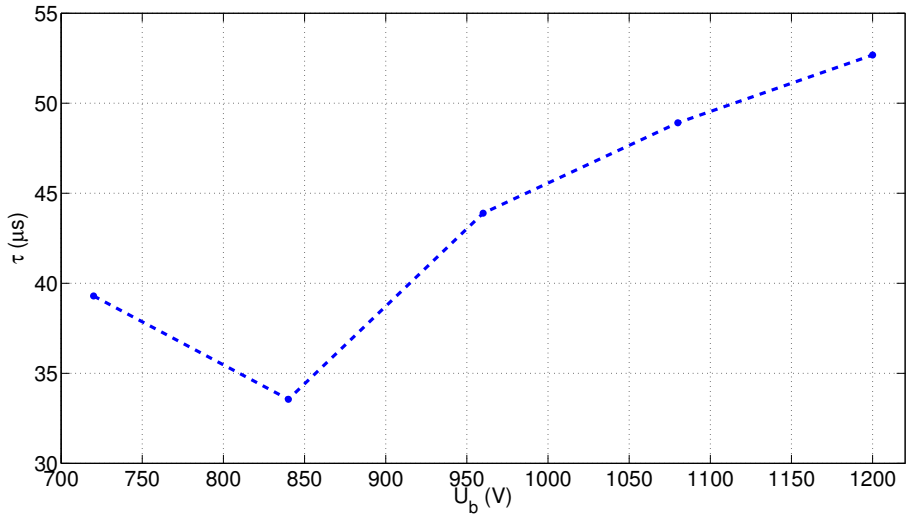

Figure 8.6: Energy confinement time τ in function of the applied voltage for the toroidal magnetic field U_b. The gas filling pressure p_{H_2} varied between 20.12 mPa and 23.45 mPa.

8.6 Conclusion

During the campaign on GOLEM a number of shots were performed (#3459–3498). A few data outputs were used to determine the energy confinement time τ, a characteristic of how good energy is confined in the plasma. One can find that τ increases with increasing inserted gas pressure, which is also qualitatively confirmed by the NeoAlcator–scaling relation. Furhermore

one observes an increasing energy confinement time with increasing toroidal magnetic field.

Although only a limited variety of diagnostics are available GOLEM is of great educational importance. It can be used to demonstrate some basic principles of the tokamak concept and nuclear fusion. Furthermore the remote control is very convenient to make the experiments and the data accessible for every body around the globe. On the first of December 2010 this was clearly demonstrated with the **Tokamak Global Experiment [41]** which united 38 participants (including myself) from 10 different countries to make real fusion shots. It was the first time ever that such a global fusion experiment was performed whereby the participants, using internet, controlled 100% remotely the tokamak from their home locations. The experiment even got mentioned on the ITER news pages, see [42].

Chapter 9

Conclusion

Appendix A

Symbols

Here an overview is given of all the symbols used in this thesis work. It is recommended to first go through this list before proceeding with the main matter of the thesis.

- e^- electron
- e^+ positron
- p proton
- n neutron
- D deuterium
- T tritium
- γ photon
- ν neutrino
- $\bar{\nu}$ anti neutrino
- α alpha–particle (or ^{4}He)

Note 1: all atoms occur in their ionised state unless stated otherwise.

- V applied voltage
- V_p plasma potential or spatial potential
- V_f floating potential
- ϕ particle flux
- j current density
- I current
- v particle velocity
- $\bar{v}$ mean particle velocity
- m particle mass
- e unit of electron charge
- q particle charge (mostly $q = -e$ or $q = +e$)

- $\vec{v}$ particle velocity
- $\vec{E}$ electrical field
- $\vec{B}$ magnetic field
- $\vec{F}$ external force
- T temperature
- p pressure (the context will make clear if one mentions pressure or proton)
- n particle density (the context will make clear if one mentions density or neutron)
- A collection area of the probe
- λ_D Debeye shielding length
- a typical dimension of the probe
- D diffusive coefficient
- l mean free path

Note 2: temperatures are usually expressed in units of eV by the conversion: $1\,\mathrm{eV} = 11604.505\,\mathrm{K}$. Therefore the Boltzmann constant $k_B = 1.3806503\,10^{-23}\,\mathrm{m^2 kg^2 s^{-2} K^{-1}}$ is omitted in this thesis work unless stated otherwise.

Note 3: some quantities may appear with a subscript i or e refering to ions respectively electrons.

Appendix B

Statistical functions

B.1 Probability functions

B.1.1 The probability density function

The probability $P(x)$ that a quantity x lies between a and b is defined as:

$$P(x) = \int_a^b f(u)\ \mathrm{d}u \tag{B.1}$$

Herein $f(u)$ is called the probability distribution function (PDF).

Closely related to the PDF is the cumulative distribution function (CDF) which is defined as:

$$P(x) = \int_{-\infty}^{x} f(u)\ \mathrm{d}u \tag{B.2}$$

B.1.2 Statistical moments

Often one is interested in the calculation of a moment M_n of order n of a PDF. The first order moment is defined as:

$$M_1(x) = E[x] = \int_{-\infty}^{+\infty} uf(u)\ \mathrm{d}u \tag{B.3}$$

The second order moment:

$$M_2(x) = E[x^2] = \int_{-\infty}^{+\infty} u^2 f(u)\ \mathrm{d}u \tag{B.4}$$

Generally one has:

$$M_n(x) = E[x^n] = \int_{-\infty}^{+\infty} u^n f(u)\ \mathrm{d}u \tag{B.5}$$

with $n >= 0$ whereby $n = 0$ is nothing else than the normalisation of the PDF.

B.2 Auto–correlation function

The auto–correlation function $R_x(\tau)$ is a measure of the correspondence of a signal $x(t)$ on time t with itself when it is shifted by a time lag τ, i.e. $x(t-\tau)$ or formula form:

$$R_x(\tau) = E[x(t)x(t-\tau)] \tag{B.6}$$

One can see that the auto–correlation function is strongly related with the second order moment of the PDF (see equation (B.4)).

B.3 Cross–correlation function

The cross–correlation function $R_{xy}(\tau)$ is actually an extension of the definition of the auto–correlation function in the sense that two differen signals x and y are compared:

$$R_{xy}(\tau) = E[x(t)y(t-\tau)] \tag{B.7}$$

B.4 Cross–power spectrum

The cross–power spectrum $S_{xy}(f)$, which is defined as the Fourier transform of the cross–correlation function ((B.7)):

$$S_{xy}(f) = \int_{-\infty}^{+\infty} R_{xy}(\tau) \exp(i2\pi f\tau)\, \mathrm{d}\tau \tag{B.8}$$

with f the temporal frequency.

In section 6.2 the cross–power spectrum will be calculated for two real current signals. Hence x and y in expression (B.8) are real function and it can be shown that:

$$S_{xy}(-f) = S_{xy}^{*}(f) \tag{B.9}$$

This last expression means that it sufficient to consider only the part of the power–spectrum at positive frequencies.

Furthermore equation (B.8) indicates that $S_{xy}(f)$ is a complex function and thus can be expressed in polar form:

$$S_{xy}(f) = |S_{xy}(f)| \exp(i\phi(f)) \tag{B.10}$$

Plotting the fase $\phi(f)$ in function of the frequency f gives a linear relation between both:

$$\phi(f) = 2\pi f\tau \tag{B.11}$$

Bibliography

[1] United Nations, "World Population Prospects: The 2002 Revision Highlights," *ESA/P/WP. 180*, 26 February 2003. 2, 3

[2] Atmoz, "The Future: Distributed Energy Production and Storage." `http://atmoz.org/blog/2008/11/05/the-future-distributed-energy-production-and-storage`, cited August 2010. 3

[3] U.S. Energy Information Administration, "International Energy Statistics." `http://www.eia.doe.gov/emeu/international/energyconsumption.html`, cited February 2011. 4, 84

[4] S. Shafiee and E. Topal, "When will fossil fuel reserves be diminished?," *Energy Policy*, vol. 37, no. 1, pp. 181–189, 2009. 2

[5] Hyperphysics, "Fission and fusion can yield energy." `http://hyperphysics.phy-astr.gsu.edu/hbase/nucene/nucbin.html`, cited August 2010. 7, 80

[6] Case Western Reserve University, "Overcoming the Coulomb Barrier." `http://burro.cwru.edu/Academics/Astr221/StarPhys/coulomb.html`, cited August 2010. 7

[7] Wikipedia, "Nuclear Fusion." `http://en.wikipedia.org/wiki/File:Fusion_rxnrate.svg`, cited September 2010. 9, 80

[8] New Scientist, "Mass cut-off between stars and brown dwarfs revealed." `http://www.newscientist.com/article/dn9771-mass-cutoff-between-stars-and-brown-dwarfs-revealed.html`, cited August 2010. 10

[9] Wikipedia, "Inertial confinement fusion." `http://en.wikipedia.org/wiki/Inertial_confinement_fusion`, cited August 2010. 11, 80

[10] European Commission–Research & Innovation, "Euratom Nuclear Research–Fusion." `http://ec.europa.eu/research/energy/euratom/fusion/at-work/tech-prep-demo/index_en.htm`, cited March 2011. 12, 80

[11] G. Van Oost, *Plasma Physics, Part A: High Temperature Plasma Physics*. Universiteit Gent, 2008–2009. 13, 14

[12] Nederlands Onderzoeksplatform Duurzame Energievoorziening, "De tokamak." `http://www.energieplatform.nl/energieopties/kernfusie/achtergrond/techniek/de-tokamak/`, cited August 2010. 14, 80

[13] I. Caldas et al., "Control of Chaotic Magnetic Fields in Tokamaks," *Brazilian Journal of Physics*, vol. 32, no. 4, December 2002. 14, 80

[14] JET, "Ohmic Heating." `http://www.jet.efda.org/focus-on/plasma-heating-current-drive/ohmic-heating/`, cited September 2010. 16

[15] JET, "Tokamaks." `http://www.jet.efda.org/wp-content/uploads/magconfinement-s2.jpg`, cited August 2010. 16

[16] P. Stangeby, "A tutorial on some basic aspects of divertor physics," *Plasma physics and controlled fusion*, vol. 42, pp. B271–B291, DEC 2000. 27th European-Physical-Society Conference on Controlled Fusion and Plasma Physics, BUDAPEST, HUNGARY, JUN 12-16, 2000. 16, 17

[17] J. Linke, "Plasma facing materials and components for future fusion devices - development, characterization and performance under fusion specific loading conditions," *Physica scripta*, vol. T123, pp. 45–53, 2006. 5th International Workshop and Summer School on Plasma Physics, POLAND, JUN 06-10, 2005. 17

[18] JET, "Limiters and Divertors." `http://www.jet.efda.org/focus-on/limiters-and-divertors/`, cited October 2010. 17, 80

[19] C. Pitcher and P. Stangeby, "Experimental divertor physics," *Plasma physics and controlled fusion*, vol. 39, pp. 779–930, JUN 1997. 17

[20] ITER, "The way to new energy." `http://www.iter.org/`, cited August 2010. 17

[21] EURATOM–IPP.CR, "Association EURATOM-IPP.CR." `http://www.ipp.cas.cz/Tokamak/euratom/`, cited August 2010. 18, 84

[22] IPP Prague, "Diagnostics." `http://www.ipp.cas.cz/Tokamak/euratom/index.php/en/compass-diagnostics`, cited September 2010. 18, 19, 80

[23] I. Hutchinson, *Principles of Plasma Diagnostics, Second Edition*. Cambridge University Press, 2002. 18, 19, 20, 28, 80

[24] V. Demidov, S. Ratynskaia, and K. Rypdal, "Electric probes for plasmas: The link between theory and instrument," *Review of scientific instruments*, vol. 73, pp. 3409–3439, OCT 2002. 25, 28, 80

[25] M. Goossens, *An Introduction to Plasma Astrophysics*. Katholieke Universiteit Leuven, March 2003. 27

[26] J. Tagle, P. Stangeby, and S. Erents, "Errors in measuring electron temperatures using a single Langmuir probe in a magnetic field," *Plasma physics and controlled fusion*, vol. 29, pp. 297–301, MAR 1987. 29

[27] K.-U. Riemann, "The Bohm criterion and sheath formation," *Journal of physics D-applied physics*, vol. 24, pp. 493–518, APR 14 1991. 29, 30

[28] J. E. Allen, "The plasma-sheath boundary: its history and Langmuir's definition of the sheath edge," *Plasma sources science & technology*, vol. 18, FEB 2009. 30

[29] K.-U. Riemann, "Plasma and sheath," *Plasma sources science & technology*, vol. 18, FEB 2009. 30

[30] I. Katsumata and M. Okazaki, "Ion sensitive probe - A New Diagnostic Method for Plasma In Magnetic Field," *Japanese journal of applied physics*, vol. 6, no. 1, pp. 123–124, 1967. 31

[31] J. Adamek, J. Stockel, M. Hron, J. Ryszawy, M. Tichy, R. Schrittwieser, C. Ionita, P. Balan, E. Martines, and G. Van Oost, "A novel approach to direct measurement of the plasma potential," *Czechoslovak journal of physics*, vol. 54, no. Part 1-3 Suppl. C, pp. 95–99, 2004. 21st Symposium on Plasma Physics and Technology, Prague, CZECH REPUBLIC, JUN 14-17, 2004. 31, 32, 80

[32] J. Adamek, J. Stockel, I. Duran, M. Hron, R. Panek, M. Tichy, R. Schrittwieser, C. Ionita, P. Balan, E. Martines, and G. Van Oost, "Comparative measurements of the plasma potential with the ball-pen and emissive probes on the CASTOR tokamak," *Czechoslovak journal of physics*, vol. 55, pp. 235–242, MAR 2005. Workshop on Electric Fields, Structures and Relaxation in Edge Plasmas, Nice, FRANCE, OCT 26-27, 2004. 32

[33] J. Adamek, J. Horacek, H. W. Mueller, V. Rohde, C. Ionita, R. Schrittwieser, F. Mehlmann, B. Kurzan, J. Stoeckel, R. Dejarnac, V. Weinzettl, J. Seidl, M. Peterka, and ASDEX Upgrade Team, "Ball-Pen Probe Measurements in L-Mode and H-Mode on ASDEX Upgrade," *CONTRIBUTIONS TO PLASMA PHYSICS*, vol. 50, pp. 854–859, NOV 2010. 35

[34] J. Brotankova, *Study of high temperature plasma in tokamak-like experimental devices.* PhD thesis, Charles University Prague, 2009. 47, 50, 66

[35] G. Van Oost, M. Berta, J. Brotankova, R. Dejarnac, E. Del Bosco, E. Dufkova, I. Duran, M. P. Gryaznevich, J. Horacek, M. Hron, A. Malaquias, G. Mank, P. Peleman, J. Sentkerestiova, J. Stoeckel, V. Weinzett, S. Zoletnik, B. Tal, J. Ferrera, A. Fonseca, H. Hegazy, Y. Kuznetsov, A. Ossyannikov, A. Singh, M. Sokholov, and A. Talebitaher, "Joint experiments on small tokamaks: edge plasma studies on CASTOR," *Nuclear Fusion*, vol. 47, pp. 378–386, May 2007. 50

[36] R. Dejarnac, J. P. Gunn, J. Stoeckel, J. Adamek, J. Brotankova, and C. Ionita, "Study of ion sheath expansion and anisotropy of the electron parallel energy distribution in the CASTOR tokamak," *Plasma Physics and Controlled Fusion*, vol. 49, pp. 1791–1808, Nov 2007. 50

[37] GOLEM, "GOLEM tokamak na fjfi cvut." `http://golem.fjfi.cvut.cz/?p=uvod`, cited September 2010. 64, 65, 66, 82

[38] GOLEM, "Archive." `http://golem.fjfi.cvut.cz/?p=archive`, cited September 2010. 65, 66

[39] G. Pokol, C. Buday, and D. Imre Refy, "Instructions for student measurements on the golem tokamak," March 21, 2010. 65, 66

[40] Ron Parker, "An Alcator Chronicle or What Happened to Alcator B?." Presentation. 68

[41] The Tokamak Global Team, "Global Tokamak Experiment." `http://tokamakglobal.com/`, cited December 2010. 71

[42] ITER, "ITER Newsline." `http://www.iter.org/newsline/156/512`, cited January 2011. 71

List of Figures

List of Tables